Title
Metal-Radical Magnetic Exchange: From Molecules to Metal–Organic Frameworks

Author
Darago, Lucy

Publication Date
2018

Peer reviewed|Thesis/dissertation

Metal-Radical Magnetic Exchange: From Molecules to Metal–Organic Frameworks

by

Lucy Elizabeth Darago

A dissertation submitted in partial satisfaction of the

requirements for the degree of

Doctor of Philosophy

in

Chemistry

in the Graduate Division

of the

University of California, Berkeley

Committee in charge:

Professor Jeffrey R. Long, Chair
Professor Richard A. Andersen
Professor Michael F. Crommie

Summer 2018

Metal-Radical Magnetic Exchange: From Molecules to Metal–Organic Frameworks

Lucy Elizabeth Darago

Abstract

Metal-Radical Magnetic Exchange: From Molecules to Metal–Organic Frameworks

by

Lucy Elizabeth Darago

Doctor of Philosophy in Chemistry

University of California, Berkeley

Professor Jeffrey R. Long, Chair

This dissertation describes several investigations into the use of paramagnetic ligands to drive new electronic behaviors in molecules and materials. In the field of single-molecule magnetism, radical bridging ligands are primarily of interest as a mode of generating strongly exchange-coupled magnetic units for use in high-density data storage. Incorporation of radical ligands into metal–organic frameworks may provoke a more diverse set of behaviors, including electronic conductivity, redox activity, and bulk magnetic ordering. *Chapter 1* provides a perspective on the field of metal-radical coordination chemistry, highlighting some of the most notable metal-radical materials in the literature.

Chapter 2 details the study of a three-dimensional metal-radical solid composed of Fe^{III} centers and paramagnetic semiquinoid linkers, $(NBu_4)_2Fe^{III}_2(dhbq)_3$ ($dhbq^{2-/3-}$ = 2,5-dioxidobenzoquinone/1,2-dioxido-4,5-semiquinone). UV-Vis-NIR diffuse reflectance measurements reveal that this framework exhibits Robin-Day Class II/III ligand mixed valence, one of the first such observations in a metal–organic framework. The mixed-valence ligand manifold is shown to facilitate high electronic conductivity in addition to strong metal-ligand magnetic exchange. Slow-scan cyclic voltammetry is used to probe the redox activity of the framework, leading to synthesis of the reduced framework material $Na_{0.9}(NBu_4)_{1.8}Fe^{III}_2(dhbq)_3$ via a post-synthetic chemical reduction reaction. Differences in electronic conductivity and magnetic ordering temperature between the two compounds are correlated to the relative ratio of the two different ligand redox states. Overall, the transition metal-semiquinoid system is established as a particularly promising scaffold for achieving tunable long-range electronic communication in metal–organic frameworks.

In *Chapter 3*, a series of two-dimensional lanthanide-quinoid metal–organic frameworks of the formula $Ln_2(dhbq)_3(DMF)_x \cdot yDMF$ (Ln = Y, Sm–Yb, DMF = *N*,*N*-dimethylformamide) is synthesized and post-synthetically reduced to produce the series of lanthanide-semiquinoid frameworks $Na_xLn_2(dhbq)_3(DMF)_y(THF)_z$ (THF = tetrahydrofuran). This set of lanthanide-radical frameworks is investigated using IR and UV-Vis-NIR spectroscopies, which confirm the presence of radical ligands. Magnetic susceptibility measurements indicate that lanthanide-radical magnetic exchange is relatively weak and localized. The systematic analysis of magnetic behaviors of lanthanide-radical coordination solids incorporating a series of lanthanide ions allows for new discussion regarding enhancement of lanthanide-radical magnetic exchange in extended solids.

Chapter 4 reports the synthesis and characterization of the trinuclear 4d-4f complexes $[(C_5Me_5)_2Ln(\mu\text{-}S)_2Mo(\mu\text{-}S)_2Ln(C_5Me_5)_2][Co(C_5Me_5)_2]$ (Ln = Y, Gd, Tb, Dy), containing the highly polarizable and paramagnetic MoS_4^{3-} bridging unit. UV-Vis-NIR diffuse reflectance and electron paramagnetic resonance spectroscopies reveal substantial charge transfer between Mo^{V} and Ln^{III} centers. This metal-to-metal charge transfer enables strong ferromagnetic Ln–Mo exchange, giving rise to one of the largest Gd^{III} magnetic exchange constants, $J_{Gd–Mo}$, observed to date, +16.1(2) cm^{-1}. Both the Tb^{III} and Dy^{III} complexes are shown to exhibit slow magnetic relaxation via ac magnetic susceptibility measurements, with the Dy^{III} congener exhibiting the largest thermal relaxation barrier yet reported for a complex containing a 4d metal center, 68 cm^{-1}. These results demonstrate a generalizable route to enhanced nd-4f magnetic exchange, revealing opportunities for the design of new nd-4f single-molecule magnets.

Table of Contents

Acknowledgements…… ii
Dedication…….... v

Chapter 1: An Introduction to the Magnetism of Metal-Radical Materials
Section 1.1. Introduction…… 2
Section 1.2. Magnetic Exchange in Coordination Chemistry…… 3
Section 1.3. Single-Molecule Magnets with Radical Ligands……..... 4
Section 1.4. Towards Metal–Organic Bulk Magnets: Inspiration from Magnetic Molecules…..... 8
Section 1.5. Metal-Radical Coordination Solids……... 10
Section 1.6. References…… 14

Chapter 2: Electronic Conductivity, Ferrimagnetic Ordering, and Reductive Insertion Mediated by Organic Mixed-Valence in a Ferric Semiquinoid Metal–Organic Framework
Section 2.1. Introduction……... 19
Section 2.2. Experimental Information……..... 20
Section 2.3. Results and Discussion……... 21
Section 2.4. Conclusions and Outlook……... 31
Section 2.5. Acknowledgements……... 32
Section 2.6. References……..... 32
Chapter 2 Supporting Information……..... 35

Chapter 3: Magnetic Exchange in Two-Dimensional Lanthanide-Semiquinoid Frameworks
Section 3.1. Introduction……... 48
Section 3.2. Experimental Information…….. 49
Section 3.3. Results and Discussion……... 50
Section 3.4. Conclusions and Outlook……... 59
Section 3.5. Acknowledgements……..... 59
Section 3.6. References……..... 60
Chapter 3 Supporting Information……..... 62

Chapter 4: Strong Ferromagnetic Exchange Coupling and Single-Molecule Magnetism in MoS_4^{3-}-Bridged Dilanthanide Complexes
Section 4.1. Introduction……..... 80
Section 4.2. Experimental Information…….. 81
Section 4.3. Results and Discussion……... 83
Section 4.4. Conclusions and Outlook……... 92
Section 4.5. Acknowledgements……... 92
Section 4.6. References……..... 93
Chapter 4 Supporting Information……..... 96

Acknowledgements

While my Ph.D. journey has taken a little longer than initially hoped, I now find myself wishing for more time to spend with the incredible people I met along the way. The friendships developed over the course of the last six years have at times tested and most times maintained my sanity, and I am extremely grateful to have met such an extraordinary cast of talented, diverse, and generous scientists.

My advisor Jeff Long has always encouraged me to think ambitiously and creatively. I have become a much more confident and independent researcher while working for him, and will always be thankful for his support. Jeff balances the many demands on his time with a level of patience and openness that are quite uncommon in academia, and the opportunity to work in his lab is one I appreciate more and more the longer I spend in it.

I am thankful for a great set of year-mates: Doug Reed, for his loyalty, frankness, and, of course, fashion sense, Matt Kapelewski, for his contagious enthusiasm and willingness to plan events, and Phil Bunting, my magnetism contemporary, who has been beyond dependable when needed, and whose philosophic insights and life strategies are always entertaining. The four of us have shared two weddings, countless drinks, research failures and successes, and, in general, a fair bit of growth into adulthood. Our camping trip to Yosemite / "accidental" celebration of my birthday is a very fond memory. It is hard to believe how lucky I was to end up with a crew as kind, interesting, and clever as these guys are.

The years below us brought more amazing group members, including Jon Bachman, Mercedes Taylor, Julia Oktawiec, and Rodi Torres-Gavosto in 2013. Jon's magnetic personality and entrepreneurial spirit are sure to bring him success. Mercedes brought support and humor (often in quiz form) to our ladies group when it was needed most, and has been a stalwart companion in these final months of writing. Julia's love of all things cute is matched only by her love for science, and it has been a true pleasure to watch her crush it in the lab, as well as share moments of late-night silliness I would trust with no one else. I have always enjoyed working with Rodi— his intelligence and passion make it as easy to collaborate with him as it is to get in a debate with him!

The arrival of Rebecca Siegelman and Kristen Colwell in 2014 added two more women to our awesome contingent in lab, and they made being a lady scientist cooler than ever. Rebecca's technical expertise and attention to detail are invaluable in the lab, and she is a trustworthy and considerate friend. Kristen is extremely bright and creative, and has pursued one of the most challenging projects in the lab with great determination. I know she can accomplish anything she sets her mind to!

The next year brought in a very large magnetism class, and as a result I begrudgingly became quite close to this crew. In Colin Gould I finally found a labmate whose high spirits matched my own. Our entertaining chats have provided much-needed breaks from thesis work, and it has been inspiring to watch his research progress. Ari Turkiewicz's deeply sarcastic personality often overshadows his thoughtfulness and insight, but I am always reminded when hanging out with him that these other qualities are quite present too. I can't help but see Henry Jiang as our oddball visiting undergrad from my early years of grad school, but his dedication to the IR craft (among other crafts) exhibits the thorough, intense researcher he has become. Job Chakarawet impressed from day one with his meticulous research. He is very fun to talk to about both science and his personal life, which he wisely refuses to detail, though this hasn't stopped me from trying. Dan Lussier has met the extreme challenge of understanding uranium magnetism with an unbelievable amount of hard work and persistence. I always enjoy talking shop with him, and know his

dedication will pay off. Jesse Park has the admirable combination of talent and humility, and I look forward to following his work in the next few years. Mike Ziebel is perhaps my most direct successor, inheriting all things "dhbq" in addition to the dubious honors of safety officer and lab manager. We share a great deal in common, in particular desires both to do things the right way and to be in charge. While this could have led us into conflict, it has instead led to a steadfast alliance that has made my last few years of grad school both easier and more enjoyable.

The next two years brought a number of students who are already making great contributions to the lab, including Ryan Murphy, David Jaramillo, Naomi Biggins, Kaipeng Hou, Eugene Kim, and Ever Velasquez in 2016, and then Maria Paley, Alex Vincent, Ziting Zhu, Surya Parker, Katie Engler, and Adam Uliana in 2017, all of whom show great promise. I will single out Ryan, who I have worked with quite a bit with in the past few years. I can always look to Ryan to get a unique opinion on pretty much any topic, scientific or otherwise. Ryan's independence and initiative have already begun to pay off, and I look forward to seeing his future work. I will also speak a bit about Alex since he is the newest "magnet"— he has been a ton of fun to work with this past year and has pursued some of my zanier ideas with great determination, all the while making improvements far beyond what I ever would have tried. In collaboration with Colin, persuading Alex to partake in group events has been a highlight of the year. All in all, it is clear the future of the Long group is in great hands.

Of course, I also worked with a number of talented older researchers who served as excellent mentors and role models. I would not have made it very far without the teachings of Michael Nippe, who was somehow able to deliver years of synthetic knowledge over the course of ten-minute smoke breaks. Magnet mentors Joe Zadrozny and Katie Meihaus showed me (and Phil) how it was done— these two were some of the hardest working scientists I have ever seen, and their scientific rigor set the standard for the Long group and generations of magnetism students to come. Katie has been both a great friend and mentor, and I admire her dedication to making the world a better, kinder place. I would also like to thank Eric Bloch for making me feel like a part of the team in that difficult first year of grad school. Brian Weirs always knew how to make me laugh, and taught me to not take work too seriously. Dianne Xiao was the first friend I made in Berkeley. Her incredible work ethic, thoughtfulness, and intelligence, as well as our shared love of gossip, make her an equally amazing labmate and friend. Miguel Gonzalez has been a great friend and entertaining rival. His unmatched critical thinking undoubtedly made me a better scientist, and his enduring support got me through the tougher times. I would further like to thank group members Jordan Axelson, David Zee, Jarad Mason, Xiaowen Feng, Dana Levine, Tom McDonald, and Zoey Herm for their support and friendship. I would like to thank Selvan Demir for a very interesting collaboration on models for magnetic exchange. I would also like to thank Lucie Norel, an outstanding visiting scientist and collaborator who became a great friend. Working with Lucie gave some much-needed fresh energy to the latter half of my PhD work.

Additionally, I was fortunate to participate in some excellent collaborative efforts. I would like to thank Professor Bill Evans and his students Monica Boshart, Dan Huh, Austin Ryan, Chad Palumbo, and Chris Kotyk at UC Irvine for the opportunity to study so many interesting lanthanide complexes. Wayne Lukens helped to evaluate some crucial EPR spectra, and was a great sounding board for development of some of the magnetic exchange models contained herein. Professor Laura Gagliardi and recently her postdoctoral researcher Jingyun Ye at the University of Minnesota have provided excellent and efficient computational analyses and research feedback, and I am grateful for their help. Further, I am grateful to have had the opportunity to work with Andy Nguyen and Professor T. Don Tilley at Berkeley on the study of cobalt cubane complexes,

which provided both opportunity and incentive to improve my understanding of transition metal magnetism. During my PhD work I developed an interest in the behaviors of metal–organic frameworks under high-pressure conditions. My venture into high-pressure science would not have been possible without the generous time and teachings of a number of scientists, including Martin Kunz, Christine Beavers, and Andrew Doran at Beamline 12.2.2 at the Advanced Light Source, Kurt Leinenweber at Arizona State University, Matthew Koc of the Alivisatos group at Berkeley, Zhenxian Liu at Beamline 22-IR-1 at NSLS-II, and Adam Jaffe.

I would like to thank my undergraduate advisor Ram Seshadri and my undergraduate mentor Brent Melot. Ram started my research career by asking me to work in his lab after my first year of general chemistry class at UCSB. Ram's enthusiasm and boundless support made research unintimidating and fun. I am so fortunate to have had his guidance not only at UCSB but also throughout my time in graduate school. Brent's approachable and candid nature made him the obvious model from which to develop my own mentorship style. The joy for science that I cultivated at UCSB, buoyed by the support of these mentors, was the foundation I turned to whenever graduate school became challenging.

Finally, I would like to thank the people whose support outside of the lab made all of this possible. Mike Aubrey has been a wonderful partner who pushes me to be the best version of myself inside and outside the lab. His caring and encouragement made this work possible. I have always been able to count on Katie Klymko to share in the trials of grad school and give me a pep talk when needed; she is also my athletic hero! My friendship with Kyra Bauman, Adra Bowman, Christina Ho, and Megan Petkovic has stood the test of time (now 10 years!), and our adventures together have been a welcome reprieve from all-consuming PhD work. I would like to thank my aunts and uncles out here in the Bay Area, Elizabeth, Jo Ann, Robert, and Paul. The many dinners, trips, and events we have shared count as some of my happiest times in grad school. I would like to thank my entire Heinen family, who have always made me feel supported and loved, and in particular my grandma, Dotty Heinen, the head of an amazingly successful and ever-growing family. I would like to thank my dad, John Darago, who raised me to be hard-working and ambitious, and my mom, Patty Heinen, who taught me to take a break from the hard work every now and then. I would lastly like to thank my sisters, Nora and Maggie, who I can always count on to be my biggest supporters.

Dedicated to my parents, Patty and John

Chapter 1: An Introduction to the Magnetism of Metal-Radical Materials

1.1 Introduction

High-performance magnetic materials underpinned many technological achievements of the 20th century, including the development of portable electronics, electric motors, and data recording media.[1] The signature property of magnetic materials is their hysteresis loop, a magnetization versus applied magnetic field curve that demonstrates the magnetic memory effect, or the degree to which the material remains magnetized upon removal of an applied magnetic field. Magnetic materials are further evaluated by a few key experimental parameters, including the magnetic transition temperature, below which the material exhibits magnetic hysteresis and thereby retains spin information, the saturation magnetization, M_s, which reflects the density of magnetic moments in a material, and the coercive field, H_c, which reflects the magnetic anisotropy of the material (Figure 1.1, right).

The intermetallic materials $Nd_2Fe_{14}B$ and $SmCo_5$ (Figure 1.1), both discovered in the latter half of the twentieth century,[2-5] still reign as the best permanent magnet materials known today. Materials of this type combine the intrinsic anisotropy of the lanthanide ions, stemming from unquenched orbital angular momentum, with strong lanthanide-transition metal exchange coupling with itinerant 3d electrons to optimize magnetic behavior. However, efforts towards improving the magnetic properties of intermetallic materials have stagnated since the development of Nd-Fe-B magnets.

As ideas for improved intermetallic magnetic materials waned, the field of coordination chemistry was gaining momentum. Understanding of magnetic structure and development of predictive models for magnetic behaviors have been enduring motivations for the field of coordination chemistry over the past several decades. In particular, efforts to enhance magnetic exchange in coordination solids, as well as to develop new single-molecule magnets, molecular units that show magnetic properties akin to those of bulk magnets, have flourished. Several ambitious goals are in ongoing pursuit, including the development of both bulk metal–organic magnets and single-molecule magnets that exhibit magnetic hysteresis above room temperature. Further, development of multifunctional magnetic metal–organic materials, which exhibit secondary functions, for instance, response to gas, solvent, or ionic guest molecules, electronic conductivity, or multiferroic behavior, are of active interest, with much to be done to achieve the same degree of electronic structure diversity for metal–organic materials as is already known for solid-state materials.

Radical ligands, organic linkers hosting an unpaired electron, play a unique role in the ongoing development of magnetic molecules and materials. The often substantial spin density on the coordinating atoms of radical ligands prompts overlap of spin-carrying metal and ligand orbitals that can drive a number of new behaviors. In molecules, radical bridging ligands are particularly pertinent to the design of lanthanide-based single-molecule magnets as a mode of generating strongly exchange-coupled, but still highly anisotropic magnetic units for use in high-density data storage. In extended solids, properties such as electronic conductivity, redox activity, and bulk magnetic ordering may be observed in metal-radical materials, with implications for metal–organic battery electrode, electrocatalyst, thermoelectric, sensing, bulk magnetic, and magnetoelectric / multiferroic materials design.

The ultimate goal of the work herein is to understand which specific metal and radical pairings will lead to high-performance magnetic molecules and materials. To this end, models for magnetic exchange and a qualitative relationship between exchange strength and magnetic ordering are discussed in Section 1.2. Section 1.3 describes how magnetic exchange can impact the electronic

structure and magnetic relaxation behaviors of single-molecule magnets. Section 1.4 discusses how insights from model molecular systems can be translated to the design of new metal-radical magnetic materials. Finally, section 1.5 examines a select number of known metal-radical materials to demonstrate the diversity of properties that may be observed.

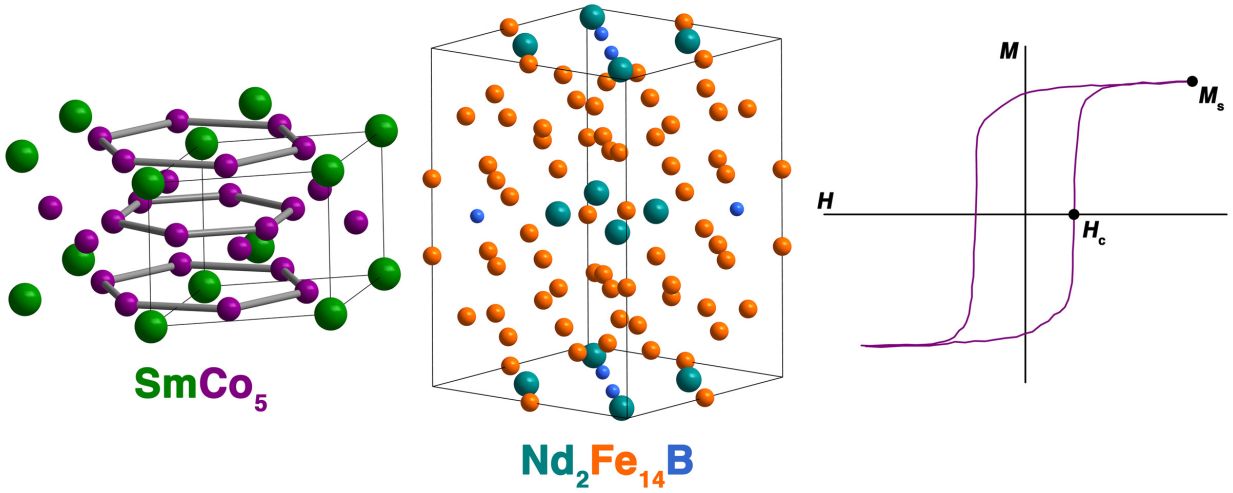

Figure 1.1. Left and center: Crystal structures of $SmCo_5$ and $Nd_2Fe_{14}B$ permanent magnet materials. Green, purple, teal, orange, and blue spheres represent Sm, Co, Nd, Fe, and B atoms, respectively. The unit cell of each structure is indicated by solid lines. Right: Magnetic hysteresis loop with magnetic performance metrics H_c and M_s indicated.

1.2 Magnetic Exchange in Coordination Chemistry

To begin, some formative models for prediction of the type and strength of magnetic exchange in molecules and extended solids will be discussed, followed by a strategy to estimate magnetic ordering temperature once exchange coupling strength is known.[6,7]

The Anderson Model for Singlet-Triplet Energy Splitting. The Anderson model[8] provides one of the earliest explorations of the mechanisms behind magnetic coupling, considering the simplest model possible: a system consisting of two $S = 1/2$ spins, which may either be paired in opposing directions (antiferromagnetic exchange to generate a singlet state) or in the same direction (ferromagnetic exchange to generate a triplet state). When predicting the nature of this interaction, two types of excited state interactions are considered. The first is the transfer of an electron from the magnetic orbital of a donor (D) into the magnetic orbital of an acceptor (A), producing the pair, D^+A^-. Since these electrons are occupying the same orbital, they must be antiparallel, or antiferromagnetically coupled. This antiferromagnetically-coupled excited state contributes to the energy of the magnetic ground state by an energy term named kinetic exchange:

$$\Delta E_1 = -4\beta^2/U$$

where β is the transfer integral, which is dependent on the orbital overlap of the magnetic orbitals involved, and U is the Coulombic repulsion energy (electron pairing energy) associated with two electrons occupying the same orbital. The second type of excited state to consider instead stabilizes a ferromagnetic interaction between the two $S = 1/2$ spins, named the potential exchange:

$$\Delta E_2 = 2K$$

where K is the intramolecular exchange integral associated with ferromagnetic coupling. This exchange integral must be similar in energy to the pairing energy U to favor ferromagnetic exchange. Charge transfer between an empty or doubly occupied orbital and a singly-occupied

magnetic orbital (SOMO) can be described by these terms in addition to further terms describing charge transfers of the HOMO and LUMO to the SOMO, allowing predictions of exchange coupling type and strength in more complex systems.[9]

These terms reveal some obvious guidelines to enhance different types of magnetic exchange. To enhance antiferromagnetic coupling, overlap between magnetic orbitals must be as large as possible. Such a scenario may be achieved by decreasing distances between spin centers, or increasing the overlap between spin-carrying orbitals (for example, by replacing a 3*d* cation with a 4*d* cation). Further, reductions in the Coulombic repulsion energy, for instance via addition of electronegative substituents to the acceptor center, should also favor antiferromagnetic exchange. In contrast, increases in the pairing energy and reductions in the degree of magnetic orbital overlap, either by distance or orbital orthogonality, will favor ferromagnetic exchange.

Spin Polarization. While the Anderson model considers the full transfer of an electron from donor to acceptor site, spin polarization models, which reflect excitations on the same spin center, must also be considered to accurately describe many exchange phenomena in molecular magnetism. Spin polarization occurs via mixing of the SOMO into the HOMO to generate new regions of positive and negative spin density, and is particularly necessary in discussion of spin density on radical ligands.[10,11] The charge transfer salts $[MCp^*_2][TCNE^{\cdot}]$ (M = Cr, Fe, Mn, Co, Ni; Cp* = pentamethylcyclopentadienyl; TCNE = tetracyanoethylene) are excellent illustrations of systems requiring consideration of spin polarization to correctly predict magnetic behaviors.[12] In the case of the complex $[CrCp^*_2][TCNE]$, since both cation and anion consist of half-filled orbitals, we would expect virtual charge transfers to stabilize antiferromagnetic ordering between the Cr^{III} spins and the $TCNE^-$ radical spin.[13] However, ferromagnetic coupling is observed, and can instead be described by a negative spin polarization of the Cp* rings by the positive spin density on the metal cation, which couples antiferromagnetically to the positive spin density on the $TCNE^-$ radical ligand, leading to ferromagnetic alignment of Cr^{III} and $TCNE^-$ spins.

Predicting Magnetic Ordering Temperatures in Extended Solids. If the strength of magnetic exchange between building blocks in an extended solid is known, or can be estimated, the mean-field expression derived by Langevin, Weiss, and Néel can be used to predict the magnetic ordering temperature of extended solid, as follows:

$$T_{\mathrm{C}} = \frac{zJ\sqrt{C_{\mathrm{A}}C_{\mathrm{B}}}}{N_{\mathrm{A}}g^2{\mu_{\mathrm{B}}}^2}$$

where T_{C} is the magnetic ordering temperature, z is the number of magnetic nearest-neighbors, J is the magnetic exchange coupling constant, C_{A} and C_{B} are the Curie constants of spin centers A and B, g is the Landé factor, and μ_{B} is the Bohr magneton.[14] This expression was initially developed to predict ordering temperatures in metal-oxide ferrimagnets, in which non-equivalent spins or spin sublattices are coupled antiferromagnetically, yielding a net magnetic moment. It has since been modified for use in a variety of molecule-based magnetic materials. Importantly, this expression predicts that enhancement of the number of magnetic neighbors, the strength of magnetic exchange, or the magnitude of the spins involved should lead to increases in magnetic ordering temperature of the corresponding extended solid.

1.3 Single-Molecule Magnets with Radical Ligands

Single-molecule magnets are molecules that possess a bistable magnetic ground state with an energy barrier to spin inversion, *U*. These molecules act as nanoscale permanent magnets with physical properties similar to those of bulk magnets, most critically that of magnetic hysteresis,

which allows single-molecule magnets to record and retain spin information.[15] As a result, single-molecule magnets are of great interest for high-density data storage, as well as quantum computation, spintronics,[16] and dark matter detection.[17] Since the discovery of single-molecule magnets in the 1990s,[18-21] the enhancement of their operating temperatures has been the primary motivation for researchers in the field. This goal requires both increases in magnetic anisotropy and magnetic relaxation times.

Considering the first goal, increases in magnetic anisotropy require definition of a preferred magnetic axis in combination with retention of orbital angular momentum. Such a combination is difficult to achieve in transition-metal-based magnetic molecules, in which strong metal-ligand bonding frequently quenches orbital angular momentum. In contrast, the lanthanide ions exhibit intrinsic magnetic anisotropy due to strong spin-orbit coupling of spin and orbital angular momentum, but require strong ligand fields to define a magnetic axis. In principle, both conditions may be met in a single-ion transition metal or lanthanide complex placed in a highly axial, strong ligand field. In such systems, spin, S, and orbital angular momentum, L, combine to give a total angular momentum, J. The combined effects of the ligand field and spin-orbit coupling remove the degeneracy of the $2J + 1$ M_J states, as depicted in Figure 1.2 for an imaginary two-coordinate dysprosium complex. The separation between the lowest and highest M_J states is the barrier to magnetic relaxation, U. In practice, the measured barrier to slow magnetic relaxation, U_{eff}, determined from an Arrhenius fit of relaxation times, τ, versus temperature according to the equation:

$$\tau^{-1} = \tau_0^{-1} e^{U_{\text{eff}}/kT}$$

is typically much lower than U. Continuing with the single-ion example, deviations from perfectly axial symmetry can break the orbital degeneracy required to preserve orbital angular momentum, and can lead to mixing of M_J states. Mixing of M_J states often leads to fast magnetic relaxation via lower M_J states.

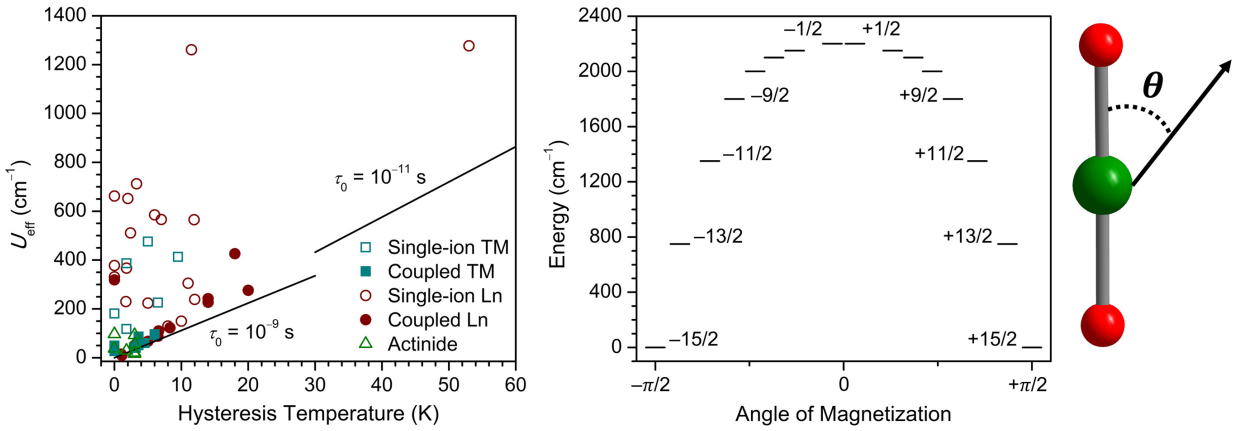

Figure 1.2. Left: Effective barrier height versus the highest temperature at which magnetic hysteresis is observed for notable single-molecule magnets. The lines represent the correlation between U_{eff} and the hysteresis temperature, assumed to correspond to a 100-s magnetic relaxation time, using the Arrhenius law, $\tau^{-1} = \tau_0^{-1} e^{U_{\text{eff}}/kT}$, with the two given τ_0 values. Right: Energy level diagram for the $J = {}^{15}/_2$ state of the fictional molecule $[Dy(OR)_2]^+$ (far right). The numbers at each line are the M_J values, with values for $M_J = \pm$ 7/2, 5/2, and 3/2 omitted due to crowding, but which occur at the expected lines above $M_J = \pm 9/2$. The angle of magnetization is the angle between the molecular magnetic moment and the molecular axis. Dysprosium and oxygen are represented by green and red spheres, respectively.

Nevertheless, large U_{eff} values have been obtained using low-coordinate or pseudo-low-coordinate ligand geometries (Figure 1.2, left). In contrast, the second condition for higher single-molecule magnet operating temperatures, slow magnetic relaxation times, has largely eluded researchers. Mononuclear single-molecule magnets are particularly vulnerable to through-barrier magnetic relaxation mechanisms. Such mechanisms include Raman relaxation, or magnetic relaxation through a virtual magnetic excited state, and quantum tunneling, in which tunneling between ground M_J states at low temperature precludes magnetic relaxation through a thermal barrier. One strategy to prevent through-barrier relaxation is simply maximization of magnetic anisotropy, which leads to more substantial splitting of M_J states, reducing the degree of M_J mixing. This strategy may be achieved through the use of ionic ligands that ideally act as point charges, and reside as close to the metal center as possible;[22-25] for instance, alkoxide and phenoxide ligands have long been used to enable axial magnetic anisotropy in lanthanide complexes.[26-28] Special symmetries such as D_{8h} and C_{5v} have also been suggested to minimize M_J mixing.[28-31] Further, recent studies on the effects of molecular vibrations on through-barrier relaxation pathways suggest that use of a lightweight, rigid coordination environment may be advantageous, for example by driving vibrations involving the metal center to very high energies.[32,33] Recent reports on the molecule $[Dy(Cp^{ttt})_2]^+$ (Cp^{ttt} = 1,2,4-tri(*tert*-butyl)cyclopentadienide), which was found to display blocking temperatures as high as 60 K in conjunction with an effective barrier of ~1230 cm^{-1}, demonstrates the successful realization of many strategies in a single molecule via its pseudo-two-coordinate environment, strong ligand field, and limited vibrational modes.[34,35] Further improvements in blocking temperature for single-ion lanthanide complexes can likely only be achieved via isolation of the Dy^{III} ion in a rigorously linear, two-coordinate environment, and this synthetically-challenging moiety is the subject of many efforts in the field.

Moving away from single-ion complexes, one of the most effective means by which to reduce through-barrier magnetic relaxation is the coupling of multiple spins to produce a molecule with a coupled, large total angular momentum ground state. Exchange interactions have been demonstrated in particular to suppress magnetic relaxation via quantum tunneling.[34-36] Initial efforts in the field of single-molecule magnetism focused on exchange coupling of transition metal centers, though it was ultimately determined that magnetic anisotropy could not be appreciably increased in such systems.[37] In contrast, the exchange coupling of multiple lanthanide centers has been demonstrated to be one of the most successful strategies to increase the magnitude of the total angular momentum ground state while retaining orbital angular momentum.[38] Radical ligands have been demonstrated to engage the lanthanide ions in magnetic exchange of unprecedented strength, in spite of the small radial extension of the 4f orbitals. Magnetic exchange in multinuclear lanthanide complexes is most easily evaluated by fitting of the gadolinium congener using the Heisenberg Hamiltonian, possible due to the spin-only nature of the Gd^{III} ion:

$$\hat{H} = -2J_{\mathrm{Gd-rad}}\hat{S}_{\mathrm{rad}} \cdot \left(\hat{S}_{\mathrm{Gd(1)}} + S_{\mathrm{Gd(2)}}\right)$$

One of the most successful instances of an exchange-coupled lanthanide single-molecule magnet is a dilanthanide complex bridged by a radical N_2^{3-} unit (Figure 1.3, left). [39,54] The highly diffuse N_2^{3-} π^* orbital, which lies perpendicular to the Ln–N_2–Ln plane, enables strong magnetic exchange via direct π^*-4f_{xyz} orbital overlap,[40] quantified by the Gd^{III}-N_2^{3-} exchange coupling constant, $J_{\mathrm{Gd\text{-}rad}}$ of –20 to –27 cm^{-1} (dependent on the lanthanide coordination environment). When this strong magnetic exchange, which prompts generation of an exchange-coupled ground state with large total angular momentum, is paired with the use of anisotropic lanthanide ions, they together can produce high-operating-temperature single-molecule magnets.[41,42]

Table 1.1. Select multinuclear Gd^{III}-radical complexes and their magnetic exchange constants, assuming the 2*J* formalism.

Compound[†]	$J_{\text{Gd-rad}}$ **(cm^{-1})**	**Ref.**
$[((HBpz_3)_2Gd)_2(\mu\text{-}Cl_2dhbq^{3-})]^-$	–2.09	43
$[Gd(acac)_2(NITPhO)]_2$	+2.75 ($J_{\text{Gd-Gd}}$ = –0.08 cm^{-1})	44
$(Cp^*_2Gd)_3(\mu_3\text{-}HAN^{3-})$	–5.0	45
$[(Cp^*_2Gd)_2(\mu\text{-}tppz^{3-})]^-$	–6.29	46
$[(Cp^*_2Gd)_2(\mu\text{-}tppz^{-})]^+$	–6.91	46
$[(Cp^*_2Gd)_2(\mu\text{-}bpym^{-})]^+$	–10	
$[(Cp^*_2Gd)_2(\mu\text{-}ind^{3-})]^-$	–11.04	47
$[\{Cp^{Me4H}_2(THF)Gd\}_2(\mu\text{-}N_2^{3-})]^-$	–20.1	42
$[\{[(Me_3Si)_2N]_2(THF)Gd\}_2(\mu\text{-}N_2^{3-})]^-$	–27	39
$\{[(Me_3Si)_2N]_2(THF)Gd\}_2(\mu\text{-}N_2^{3-})K$	–27.1 ($J_{\text{Gd-Gd}}$ = –2.28 cm^{-1})	48
$Gd_2@C_{79}N$[‡]	+175	49

[†]$HBpz_3$ = hydrotris(1-pyrazol-1-yl)borate; Cp* = pentamethylcyclopentadienide; Cl_2dhbq = 2,5-chloro-3,6-dihydroxo-1,4-benzoquinone, NITPhO = 2-(2′-hydroxyphenyl)-4,4,5,5-tetrmethyl-imidazoline-1-oxyl-3-oxide, HAN = hexaazatrinapthylene; tppz = 2,3,5,6-tetra(2-pyridyl)pyridine; bpym = 2,2′-bipyrimidine; ind = indigotin, (2E)-2-(3-oxo-1H-indol-2-ylidene)-1H-indol-3-one

[‡]In this case, $J_{\text{Gd-rad}}$ refers to exchange between two Gd^{3+} ions and an electron "trapped" in a Gd-Gd bonding-type orbital.

Interestingly, the barrier *U* in magnetically-anisotropic lanthanide-radical single-molecule magnets can be directly related to the magnitude of the exchange coupling constant, $J_{\text{Ln-rad}}$, using the Hamiltonian:[50]

$$\widehat{H} = -2J_{\text{Ln-rad}}\hat{S}_{\text{rad}} \cdot \left(\hat{J}_{\text{Ln(1)}} + \hat{J}_{\text{Ln(2)}}\right) + \sum_{i=\text{Ln(1),Ln(2)}} B_2^0 \, O_2^0(i)$$

This model assumes a large axial anisotropy, represented by the B_2^0 parameter, as well as an isotropic exchange interaction between the angular momenta of the Ln^{III} centers and the N_2^{3-} radical spin.[51,52] When applied to the variable temperature magnetic susceptibility-temperature product ($\chi_M T$) data for the complex $[(Cp^{Me4H}_2Tb)_2(\mu\text{-}N_2^{3-})]^-$, a coupling constant $J_{\text{Ln-rad}}$ of –23.1 cm^{-1} is obtained with slight modulation of the g_J value away from that expected for the Tb^{III} ion. Excited state energies defined by Ising exchange coupling correspond to multiples of $J_{\text{Ln-rad}}$ based on the magnitude of ΔJ resulting from a spin flip. For instance, in $[(Cp^{Me4H}_2Tb)_2(\mu\text{-}N_2^{3-})]^-$, the first excited state, corresponding to a flip of a single Tb^{III} spin, has an energy of $12J_{\text{Tb-rad}}$, while the second state, corresponding to a flip of both Tb^{III} spins, has an energy of $24J_{\text{Tb-rad}}$. Using this formalism, a U_{eff} estimate of 277 cm^{-1} can be obtained, in excellent agreement with the experimentally observed value 276 cm^{-1}. This model also estimates a second excited state energy double that of the first, or 554 cm^{-1} for $[(Cp^{Me4H}_2Tb)_2(\mu\text{-}N_2^{3-})]^-$, which is in reasonable agreement with the experimentally observed value of $U_{\text{eff,2}}$ = 564 cm^{-1}.

The excited states defined by exchange coupling within these molecules will certainly mix with crystal-field-split M_J states to generate a perturbed excited state spectrum, and a more accurate assessment of the electronic structure would therefore entail utilizing multiple exchange parameters. Regardless, the simple model seems to have surprising utility for predicting excited state energies, and thereby magnetic relaxation barriers for lanthanide-radical complexes. By linking the magnitude of U with the magnitude of exchange coupling, this model further provides a direct pathway to higher-barrier exchange-coupled lanthanide magnets— the enhancement of magnetic exchange (provided sufficiently large uniaxial anisotropy is maintained). Towards this end, new dilanthanide molecules exhibiting strong magnetic exchange are discussed in Chapter 4.

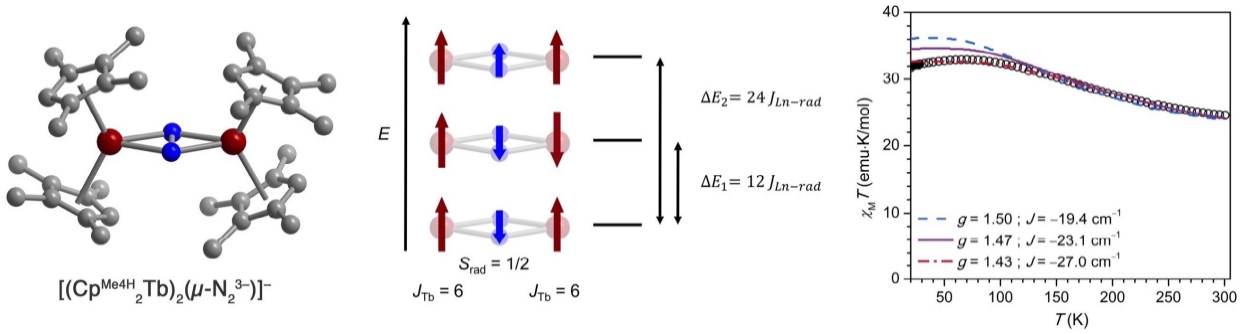

Figure 1.3. Left: The N_2^{3-}-radical-bridged complex $[(Cp^{Me4H}{}_2Tb)_2(\mu\text{-}N_2^{3-})]^-$. Grey, blue, and red spheres represent C, N, and Tb atoms, respectively. Hydrogen atoms, counter-cation, and molecules of solvation are not shown for clarity. Middle: Ladder of exchange-coupled excited states for molecules of the type $Tb_2(\mu\text{-}N_2^{3-})$. Right: Models of $\chi_M T$ data for the complex $[(Cp^{Me4H}{}_2Tb)_2(\mu\text{-}N_2^{3-})]^-$ using the Hamiltonian in Equation 1.x. Figure are modified from ref. 42.

1.4 Towards Metal–Organic Bulk Magnets: Inspiration from Magnetic Molecules

Coordination solids are an ideal synthetic platform in which to develop structure-property relationships due to the precise control possible over each framework's three main components: metal ion, ligand, and topology. Study of coordination solids, and in particular the related class of materials metal–organic frameworks,[53-56] defined by coordination bonds between metal ion or cluster and organic linker, as well as an open, potentially porous framework, has led to advances in gas storage and separations,[57,58] catalysis, [59] and sensing.[60] However, long-range electronic communication in metal–organic frameworks and its consequent properties, including electronic conductivity and bulk magnetic ordering, has largely eluded researchers.[61] Most metal–organic frameworks are essentially ionic solids, with little to no electronic communication due to frequent use of closed-shell metal ions (Zr^{4+}, Mg^{2+}, Zn^{2+}) and closed-shell linkers that promote long metal-metal distances, cutting off opportunities for communication between metal-based frontier orbitals. However, the achievement of electronic communication in metal–organic frameworks would open avenues to new applications for this class of materials as battery electrodes, supercapacitors, electrocatalysts, bulk magnets, multiferroics, and more.

Fortunately, strategies to enhance electronic communication between metals and/or organic ligands have been extensively developed in molecular chemistry. Since metal–organic frameworks are essentially combinations of molecular building blocks, study of electron delocalization in molecules should enable judicious choice of framework subunits to produce new metal–organic frameworks exhibiting continuous pathways for electronic communication. Two of the most successful and relevant strategies to engender electronic and magnetic communication in coordination solids are mixed valence and inclusion of radical bridging ligands. Incorporation of

paramagnetic bridging ligands is the primary strategy used to engender electronic communication and thereby strong magnetic exchange in extended solids in Chapters 2 and 3. However, many of the materials investigated therein are also mixed-valence, such that concepts from both of these strategies are relevant and, ultimately, highly interrelated.

Mixed Valence. Mixed-valence complexes contain either a metal or ligand that is present in more than one valence state. One of the first observations of this phenomenon was in the material Prussian blue, and mixed-valence was later demonstrated in molecular complexes such as the canonical Creutz-Taube ion, $[(NH_3)_5Ru(pz)Ru(NH_3)_5]^{5+}$.[62] Mixed-valence compounds may be classified by the degree of electronic coupling between centers of differing valence, with a general aim to determine the spatiotemporal localization of electrons in a given system. Traditionally, the degree of valence delocalization is described within the Robin-Day classification scheme.[63] Using the example of metal-centered mixed-valence, full localization (Class I mixed-valence) is observed when metal centers are in extremely different chemical environments, as determined by both ligand symmetry and ligand field strength, or are very far apart, and thus unable to engage in significant electronic coupling. Some electronic coupling between centers occurs when metal ions are in sufficiently similar environments, generating a thermal barrier to electron transfer (Class II mixed-valence). Finally, full electron delocalization— or electron itinerancy in extended systems— defines Class III mixed-valence, achieved via strong electronic coupling between metal centers. In this case, strong electronic coupling between metal-centers yields a single electronic ground state best described by assigning an intermediate valence to each metal. Mixed-valence compounds are often initially identified by an intense, optical absorption in the near-IR or visible regions, independent from optical absorptions related to the elements in either of their anticipated oxidation states. This new coloration can typically assigned as an intervalence charge transfer band (IVCT), which results from an optical excitation to provoke electron transfer.[64,65]

To a first approximation, pursuit of highly delocalized mixed valence systems simplifies to maximization of the orbital overlap between involved centers and minimization of the reorganization energy necessary for transfer of an electron between centers. Continuing with the example of metal mixed valence, choice of metal centers with minimal geometry differences, for instance octahedral d^5/d^6 pairings (e.g. Fe^{II}/Fe^{III}, either both high-spin or both low-spin), will minimize reorganization energy as exchange occurs between essentially non-bonding orbitals. Similarly, organic radicals (e.g. semiquinoid radicals) are often delocalized across extended π or aromatic systems, and as such exhibit minimal changes in bond length with changing redox state, leading to low reorganization energies.[66] Significantly, when both centers are paramagnetic, Class II and Class III mixed-valence are typically coincident with substantial magnetic exchange. In addition to minimizing reorganization energy, in order for an electron to be delocalized across multiple centers, those centers must be sufficiently close in distance, and bridged by a metal or ligand with orbitals of suitable symmetry so as to mediate electron delocalization.[67] These are the same conditions necessary to engender magnetic exchange.

Since most mixed-valence molecules consist of multiple metals but only a single bridging ligand, mixed-valence molecules almost always exhibit metal-based, rather than ligand-based, mixed-valence. However, extended redox-active metal–organic solids have a variety of metal-to-ligand radical molar ratios, and as such are more likely to demonstrate ligand-based mixed valence.

Paramagnetic Bridging Ligands. Direct magnetic exchange via overlap of spin-carrying orbitals is, intuitively, always stronger than magnetic superexchange between paramagnetic centers as mediated by a diamagnetic bridge. Thus, metal-ligand pairings that engage in direct magnetic exchange are an appealing strategy by which to pursue strong multidimensional magnetic

communication, and, in turn, metal–organic magnets with high magnetic ordering temperatures. This strategy requires use of both paramagnetic metals and paramagnetic linkers, which crucially have spin density on their coordinating atoms, enabling direct overlap of spin-carrying orbitals.

Molecular examples of radical-bridged dinuclear transition metal complexes have produced some of the strongest magnetic exchange couplings known, as high as –900 cm^{-1}.[38,68-70] Some of the metal-radical molecules studied most in-depth, and still under ongoing investigation, are complexes consisting of two transition metal ions and various redox states of the ligand 1,4-dihydroxy-2,5-benzoquinone ($dhbq^{n-}$).[68,71-81] One such example is the molecule $[((TPyA)Co^{II})_2(\mu\text{-}dhbq\text{-}Cl_2^{3-})]^+$ (TPyA = (tris(2-pyridyl)methylamine), which exhibits a large antiferromagnetic exchange coupling constant, $J_{Co\text{-}rad}$, of –52 cm^{-1} (Figure 1.4, right).[77,78] An incredible diversity of delocalization-related properties, including redox-induced-electron-transfer, spin crossover, double exchange, and valence tautomerism, have been observed for this class of molecules, inspiring use of this unit as a building block for the metal–organic frameworks studied herein.

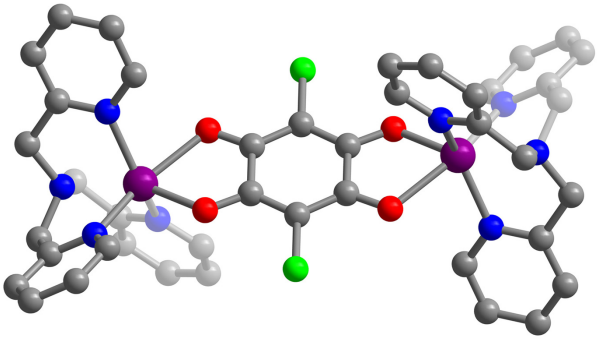

$[((TPyA)Co^{II})_2(\mu\text{-}dhbq\text{-}Cl_2^{3-})]^+$

Figure 1.4. Crystal structure of $[((TPyA)Co^{II})_2(\mu\text{-}dhbq\text{-}Cl_2^{3-})]^+$ (TPyA = (tris(2-pyridyl)methylamine) adapted from ref. 78. Dark purple, neon green, grey, blue, and red spheres represent Co, Cl, C, N, and O atoms, respectively. Counter ions, hydrogen atoms, and molecules of solvation are omitted for clarity.

1.5 Metal-Radical Coordination Solids

In solution, the free ions of most organic radicals are highly reactive and therefore relatively difficult to study. However, a number of radical ligands can be successfully stabilized in one-, two-, and three-dimensional coordination solids. A few organic radicals of interest are shown in Figure 1.5. Not that in addition to bearing an unpaired electron, each molecule also contains functional groups capable of coordinating multiple metal ions.

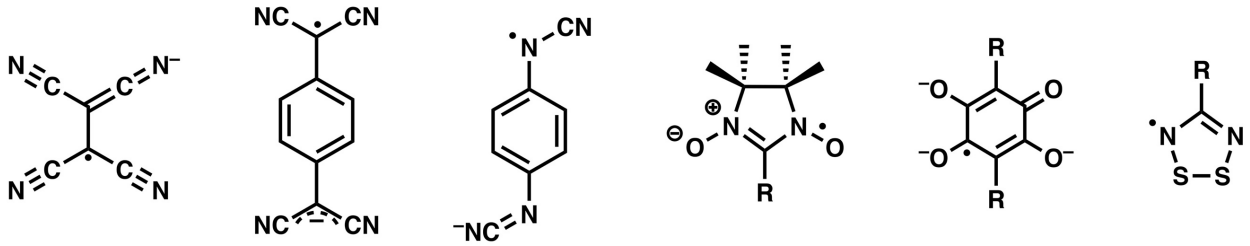

$TCNE^-$ $TCNQ^-$ $DCNQI^-$ NIT $dhbq^{3-}$ DTDA

Figure 1.5. Some of the most commonly used radical bridging ligands in coordination solids. Only one resonance structure for each ligand is shown. TCNE = tetracyanoethylene; TCNQ = 7,7′,8,8′-tetracyanoquinodimethane; DCNQI

= *N*,*N*′–dicyanoquinonediimine; NIT = 2-R-4,4,5,5-tetramethylimidazoline-1-oxyl-3-oxide; R_2dhbq = 2,5-R-3,6-dihydroxo-1,4-benzoquinone; DTDA = 4-R-1,2,3,5-dithiadiazolyl.

Metal-NIT chains. Nitronyl-nitroxide (NIT)-based materials make up one of the earliest-known and most diverse classes of metal-radical materials.[82] Nitroxides, one of the few known charge-neutral and stable radical ligands, have an N–O group with an unpaired electron in a π^* orbital that is roughly equally shared between the nitrogen and oxygen atom. Perhaps the most notable use of nitronyl nitroxides in magnetic materials is in the design of single-chain magnets, one-dimensional coordination polymers with a bistable magnetic ground state and large uniaxial magnetic anisotropy. Coordination polymers of the formula $[Co^{II}(hfac)_2(\mu\text{-NIT})]$ (hfac = hexafluoroacetylacetonate) have been shown to exhibit high magnetic blocking temperatures, up to 14 K, and large coercive fields, up to 4.9 T (at 4 K) (Figure 1.6).[83,84] These polymers can also undergo three-dimensional magnetic ordering when interchain separation is not sufficiently large, which can then prompt even higher temperature magnetic blocking behavior, > 45 K, and increased coercive fields, > 6 T.[85] Chains consisting of NIT radicals and the lanthanide ions have also been synthesized and studied, revealing antiferromagnetic Ln^{III}-NIT interactions, and single-chain magnetism for the Dy^{III} polymer $[Dy(hfac)_3(\mu\text{-(R-NIT)})]$ (R = ethyl).[86-88]

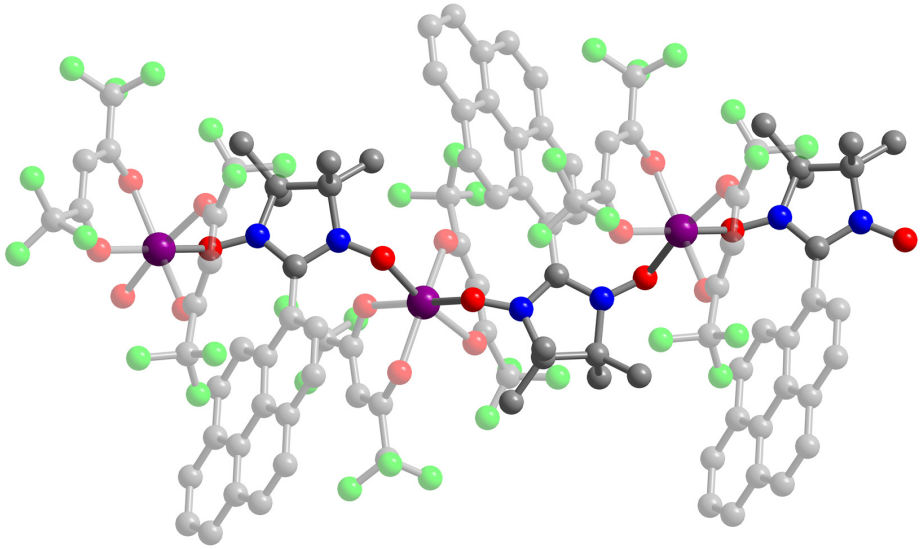

Figure 1.6. Crystal structure of $[Co^{II}(hfac)_2(\mu\text{-(R-NIT)})]$ (R = pyrenyl) adapted from ref. 83. Purple, neon green, grey, blue, and red spheres represent Co, F, C, N, and O atoms, respectively. Solvent molecules and hydrogen atoms are not shown for clarity.

Metal–TCNE materials. In general, radical ligands based on conjugated polynitriles, including TCNE and the related radical linkers TCNQ and DCNQI (Figure 1.4), are by far the most commonly observed ligands in two- and three-dimensional metal-radical solids. Tetracyanoethylene (TCNE) exhibits a low-lying π^* orbital into which an electron can be transferred to form the radical ligand $TCNE^-$. The largest spin densities on the $TCNE^-$ ligand are located on the coordinating nitrogen atoms and the central C–C bond.[89] The radical $TCNE^-$ ligand was a component of the first ferromagnetic containing spins in a *p*-orbital, [FeCp*$_2$][TCNE].[90] Coordination solids containing TCNE include a number of high-ordering-temperature metal-organic magnets, most famously the room-temperature magnetic material $V(TCNE)_2 \cdot yCH_2Cl_2$ (T_N ~ 400 K).[91] While $V(TCNE)_2 \cdot yCH_2Cl_2$ is amorphous, the related material $Fe(TCNE)(C_4(CN)_8)_{1/2}$

·$y$$CH_2Cl_2$ (T_N = 84 K),[92-94] containing sheets of μ_4- $TCNE^-$ radical ligands bridged by a μ_4-$(C_4(CN)_8)_{1/2}$ ligands (i.e., a dimerized $TCNE^-$ unit) has been structurally characterized[95] (Figure 1.7) and may be considered a starting point for the structure of $V(TCNE)_2 \cdot yCH_2Cl_2$. In comparison, each metal center in $V(TCNE)_2 \cdot yCH_2Cl_2$ is expected to have six magnetic neighbors, rather than the four magnetic neighbors per metal of $Fe(TCNE)(C_4(CN)_8)_{1/2} \cdot yCH_2Cl_2$, enabling its high magnetic ordering temperature. Furthermore, the larger 3*d* orbitals of V^{II} relative to Fe^{II} may be anticipated to lead to stronger metal–radical magnetic exchange. Metal-radical exchange coupling constants can be estimated for these materials using a modification of the Langevin, Weiss, and Néel expression for ferrimagnets (commonly used for Prussian blue derivatives):[96]

$$T_C = \frac{\sqrt{z_M z_{TCNE}}|J_{M-TCNE}|\sqrt{S_M(S_M+1)\cdot x \cdot S_{TCNE}(S_{TCNE}+1)}}{3k_B}$$

where T_c is the magnetic ordering temperature, J_{M-TCNE} is the nearest-neighbor magnetic coupling constant, z is the number of magnetic neighbors for each magnetic center (estimated as z = 6 for both metal and radical in $V(TCNE)_2 \cdot yCH_2Cl_2$; z = 4 for both metal and radical for $Fe(TCNE)(C_4(CN)_8)_{1/2} \cdot y\ CH_2Cl_2$), x is the number of $TCNE^-$ radical ligands per metal center (x = 2 for $V(TCNE)_2 \cdot y\ CH_2Cl_2$; x = 1 for $Fe(TCNE)(C_4(CN)_8)_{1/2} \cdot y\ CH_2Cl_2$), and k_B is the Boltzmann constant, to result in values of $J_{V\text{-}TCNE}$ = –58.6 cm^{-1} and $J_{Fe\text{-}TCNE}$ = –20.6 cm^{-1}. Ordering temperatures and coercive fields for $V(TCNE)_2 \cdot y\ CH_2Cl_2$ have shown to be highly sensitive to vanadium precursor and solvent,[97,98] and show expected decreases in magnetic ordering temperature with increasing Fe^{II} substitution.[99] Interestingly, $V(TCNE)_2 \cdot yCH_2Cl_2$ is also semiconducting, exhibiting a room-temperature conductivity of about 10^{-3} S/cm,[100] and shows a small magnetoresistance effect.[101-103] Coordination solids of TCNE have additionally been formed with some of the lanthanide ions, showing antiferromagnetic Ln^{III}-radical exchange and magnetic ordering at 8.5 K for a material of estimated formula unit $Dy(TCNE)_3 \cdot xCH_3CN$.[104] Reactivity of TCNE with uranium(III) has also been explored.[105]

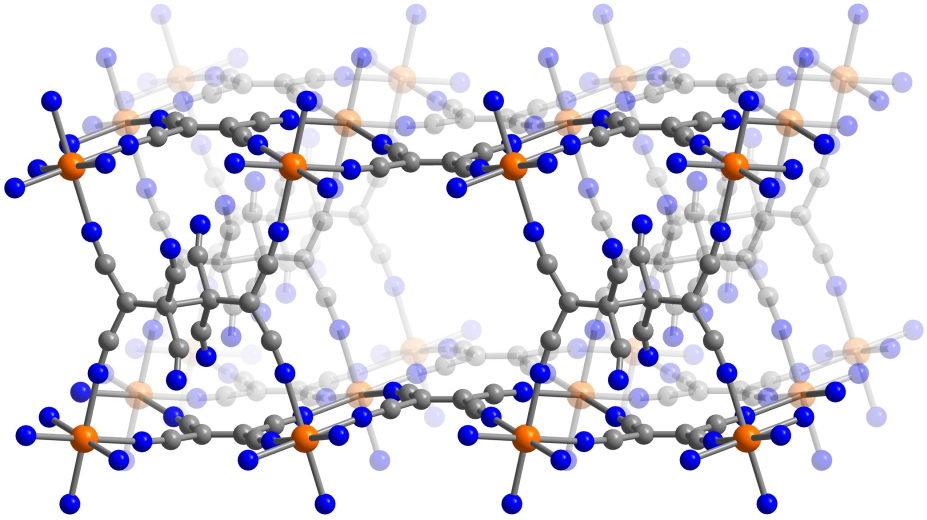

Figure 1.7. Powder X-ray diffraction structure of $Fe(TCNE)(C_4(CN)_8)_{1/2} \cdot yCH_2Cl_2$, adapted from ref. 95. Grey, blue, and orange spheres represent C, N, and Fe atoms, respectively. It was not possible to locate solvent molecule positions from the powder X-ray diffraction data, but some amount of CH_2Cl_2 is present in this structure.

Metal-TCNQ Materials. Metal–organic materials based on the TCNQ linker and its derivative DCNQI (Figure 1.5) have been shown to exhibit a diverse range of properties including magnetic ordering, electronic conductivity, and adsorbate response. For instance, the two-dimensional coordination solids Cu(2,5-R-DCNQI)$_2$ can show metallic conductivity, attributed to strong π-d conjugation between ligand and metal ions and close energy match of $TCNQ^{0/-}$ and $Cu^{II/I}$ redox potentials, leading to a mixed-valence metal manifold.[106-108] Coordination solids of the formula $M(TCNQ)_2 \cdot yCH_2Cl_2$ (M = Mn, Co, Fe, Ni) have displayed glassy magnetic behavior, with the Mn^{II} congener exhibiting the highest temperature increase in magnetization, indicative of some degree of magnetic ordering, at 44 K.[109] Of special interest is a series of materials that combine $(Ru^{II})_2$ paddlewheels with charge-neutral TCNQ to form charge-transfer solids, in which some degree of charge is transferred from the donor Ru_2 paddlewheel to the acceptor TCNQ, forming radical $TCNQ^-$ bridging ligands during material synthesis.[110] A series of Ru_2-TCNQ materials with a tunable degree of metal-ligand charge transfer has been achieved via use of linkers and paddlewheels with energetically matched HOMO-LUMO levels.[111] Further, the type of magnetic order observed for two-dimensional Ru_2-TCNQ materials has been shown to be strongly dependent on interlayer distance as well as adsorbate.[112] In a final example of interest, the material $\{Ru_2(O_2CPh\text{-}o\text{-}Cl)_4\}_2TCNQ(MeO)_2$ (TCNQ(MeO)$_2$ = 2,5-dimethoxy-7,7,8,8-tetracyanoquinodimethane) (Figure 1.8) has been shown to change from an antiferromagnet with T_N = 75 K to a ferromagnet with T_C = 56 K simply upon removal of an interstitial CH_2Cl_2 molecule.[113] These behaviors highlight the complexity of structure-property relationships in metal-radical magnetic materials.

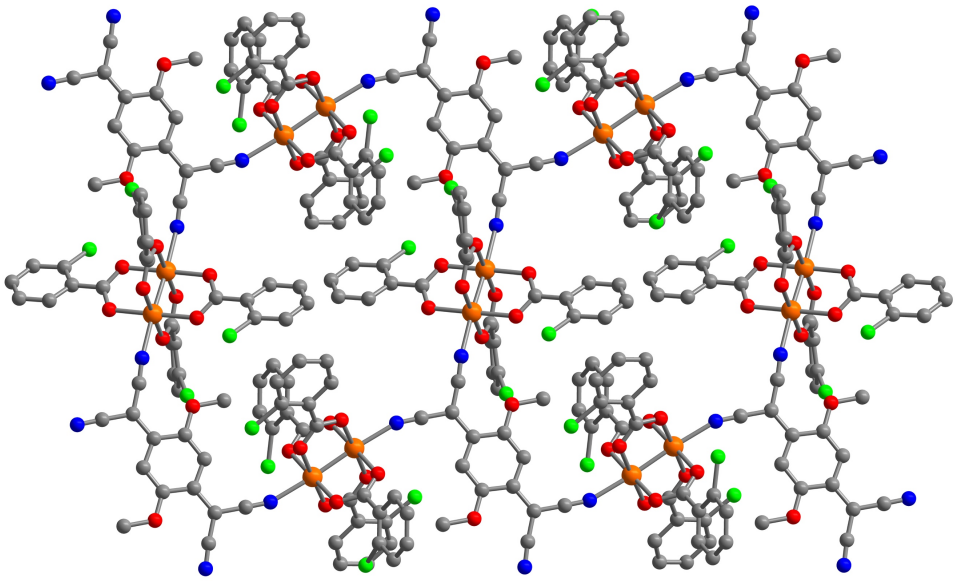

Figure 1.8. Single-crystal X-ray diffraction structure of $\{Ru_2(O_2CPh\text{-}o\text{-}Cl)_4\}_2TCNQ(MeO)_2$ (TCNQ(MeO)$_2$ = 2,5-dimethoxy-7,7,8,8-tetracyanoquinodimethane) adapted from ref. 113. Grey, blue, red, green, and orange spheres represent C, N, O, Cl, and Ru atoms, respectively. Hydrogen atoms are omitted for clarity.

1.6 References

(1) Gutfleisch, O.; Willard, M. A.; Brück, E.; Chen, C. H.; Sankar, S. G.; Liu, J. P. *Adv. Mater.* **2010**, *23*, 821.
(2) Strnat, K.; Hoffer, G.; Olson, J.; Ostertag, W.; Becker, J. J. *J. Appl. Phys.* **1967**, *38*, 1001.
(3) Croat, J. J.; Herbst, J. F.; Lee, R. W.; Pinkerton, F. E. *J. Appl. Phys.* **1984**, *55*, 2078.
(4) Sagawa, M.; Fujimura, S.; Togawa, N. *J. Appl. Phys.* **1984**, *55*, 2083.
(5) Croat, J. J.; Herbst, J. F.; Lee, R. W.; Pinkerton, F. E. *Appl. Phys. Lett.* **1984**, *44*, 148.
(6) Kahn, O. *Molecular Magnetism*; Wiley-VCH: New York, NY, 1993.
(7) Gatteschi, D.; Sessoli, R.; Villain, J. *Molecular Nanomagnets*; Oxford University Press: England, 2006.
(8) Anderson, P. W. *Phys. Rev.* **1959**, *115*, 2.
(9) Kollmar, C.; Kahn, O. *Acc. Chem. Res.* **1993**, *26*, 259.
(10) McConnell, H. M. *J. Chem. Phys.* **1963**, *39*, 1910.
(11) Kollmar, C.; Kahn, O. *J. Chem. Phys.* **1993**, *98*, 453.
(12) Miller, J. S.; Epstein, A. J. *Angew. Chem. Int. Ed.* **1994**, *33*, 385.
(13) Broderick, W. E.; Hoffman, B. M. *J. Am. Chem. Soc.* **1991**, *113*, 6334.
(14) Néel, M. L. *Annales de Physique* **1948**, *12*, 137.
(15) Mannini, M.; Pineider, F.; Sainctavit, P.; Danieli, C.; Otero, E.; Sciancalepore, C.; Talarico, A. M.; Arrio, M.-A.; Cornia, A.; Gatteschi, D.; Sessoli, R. *Nat. Mater.* **2009**, *8*, 194.
(16) Bogani, L.; Wernsdorfer, W. *Nat. Mater.* **2008**, *7*, 179.
(17) Bunting, P. C.; Gratta, G.; Melia, T.; Rajendran, S. *Phys. Rev. D* **2017**, *95*, 095001.
(18) Lis, T. *Acta. Cryst.* **1980**, *B36*, 2042.
(19) Caneschi, A.; Gatteschi, D.; Sessoli, R.; Barra, A. L.; Brunel, L. C.; Guillot, M. *J. Am. Chem. Soc.* **1991**, *113*, 5873.
(20) Sessoli, R.; Tsai, H. L.; Schake, A. R.; Wang, S. *J. Am. Chem. Soc.* **1993**.
(21) Sessoli, R.; Gatteschi, D.; Caneschi, A.; Novak, M. A. *Nature* **1993**, *365* (6442), 141.
(22) Rinehart, J. D.; Long, J. R. *Chem. Sci.* **2011**, *2*, 2078.
(23) Liddle, S. T.; van Slageren, J. *Chem. Soc. Rev.* **2015**, *44*, 6655.
(24) Chilton, N. F. *Inorg. Chem.* **2015**, *54*, 2097.
(25) Ungur, L.; Chibotaru, L. F. *Inorg. Chem.* **2016**, *55*, 10043.
(26) Blagg, R. J.; Muryn, C. A.; McInnes, E. J. L.; Tuna, F.; Winpenny, R. E. P. *Angew. Chem. Int. Ed.* **2011**, *50*, 6530.
(27) Blagg, R. J.; Ungur, L.; Tuna, F.; Speak, J.; Comar, P.; Collison, D.; Wernsdorfer, W.; McInnes, E. J. L.; Chibotaru, L. F.; Winpenny, R. E. P. *Nat. Chem.* **2013**, *5*, 673.
(28) Ding, Y.-S.; Chilton, N. F.; Winpenny, R. E. P.; Zheng, Y.-Z. *Angew. Chem. Int. Ed.* **2016**, *55*, 16071.
(29) Chen, Y.-C.; Liu, J.-L.; Ungur, L.; Liu, J.; Li, Q.-W.; Wang, L.-F.; Ni, Z.-P.; Chibotaru, L. F.; Chen, X.-M.; Tong, M.-L. *J. Am. Chem. Soc.* **2016**, *138*, 2829.
(30) Gupta, S. K.; Rajeshkumar, T.; Rajaraman, G.; Murugavel, R. *Chem. Sci.* **2016**, *7*, 5181.
(31) Liu, J.-L.; Chen, Y.-C.; Zheng, Y.-Z.; Lin, W.-Q.; Ungur, L.; Wernsdorfer, W.; Chibotaru, L. F.; Tong, M.-L. *Chem. Sci.* **2013**, *4*, 3310.
(32) Lunghi, A.; Totti, F.; Sessoli, R.; Sanvito, S. *Nat. Commun.* **2017**, *8*, 14620.
(33) Lunghi, A.; Totti, F.; Sanvito, S.; Sessoli, R. *Chem. Sci.* **2017**, *8*, 6051.
(34) Wernsdorfer, W.; Aliaga-Alcalde, N.; Hendrickson, D. N.; Christou, G. *Nature* **2002**, *416*, 406.

(35) Habib, F.; Lin, P.-H.; Long, J.; Korobkov, I.; Wernsdorfer, W.; Murugesu, M. *J. Am. Chem. Soc.* **2011**, *133*, 8830.
(36) Guo, Y.-N.; Xu, G.-F.; Wernsdorfer, W.; Ungur, L.; Guo, Y.; Tang, J.; Zhang, H.-J.; Chibotaru, L. F.; Powell, A. K. *J. Am. Chem. Soc.* **2011**, *133*, 11948.
(37) Neese, F.; Pantazis, D. A. *Faraday Discuss.* **2010**, *148*, 229.
(38) Demir, S.; Jeon, I.-R.; Long, J. R.; Harris, T. D. *Coord. Chem. Rev.* **2015**, *289–290*, 149.
(39) Rinehart, J. D.; Fang, M.; Evans, W. J.; Long, J. R. *Nat. Chem.* **2011**, *3*, 538.
(40) Vieru, V.; Iwahara, N.; Ungur, L.; Chibotaru, L. F. *Sci. Rep.* **2016**, *6*, 24046.
(41) Rinehart, J. D.; Fang, M.; Evans, W. J.; Long, J. R. *J. Am. Chem. Soc.* **2011**, *133*, 14236.
(42) Demir, S.; Gonzalez, M. I.; Darago, L. E.; Evans, W. J.; Long, J. R. *Nat. Commun.* **2017**, *8*, 2144.
(43) Zhang, P.; Perfetti, M.; Kern, M.; Hallmen, P. P.; Ungur, L.; Lenz, S.; Ringenberg, M. R.; Frey, W.; Stoll, H.; Rauhut, G.; van Slageren, J. *Chem. Sci.* **2018**, *9*, 1221.
(44) Mei, X.; Wang, X.; Wang, J.; Ma, Y.; Li, L.; Liao, D. *New J. Chem.* **2013**, *37*, 3620.
(45) Gould, C. A.; Darago, L. E.; Gonzalez, M. I.; Demir, S.; Long, J. R. *Angew. Chem. Int. Ed.* **2017**, *56*, 10103.
(46) Demir, S.; Nippe, M.; Gonzalez, M.; Long, J. R. *Chem. Sci.* **2014**, *5*, 4701.
(47) Guo, F.-S.; Layfield, R. A. *Chem. Commun.* **2017**, *53*, 3130.
(48) Meihaus, K. R.; Corbey, J. F.; Fang, M.; Ziller, J. W.; Long, J. R.; Evans, W. J. *Inorg. Chem.* **2014**, *53*, 3099.
(49) Hu, Z.; Dong, B.-W.; Liu, Z.; Liu, J.-J.; Su, J.; Yu, C.; Xiong, J.; Shi, D.-E.; Wang, Y.; Wang, B.-W.; Ardavan, A.; Shi, Z.; Jiang, S.-D.; Gao, S. *J. Am. Chem. Soc.* **2018**, *140*, 1123.
(50) Prša, K.; Nehrkorn, J.; Corbey, J.; Evans, W.; Demir, S.; Long, J.; Guidi, T.; Waldmann, O. *Magnetochemistry* **2016**, *2*, 45.
(51) Kofu, M.; Yamamuro, O.; Kajiwara, T.; Yoshimura, Y.; Nakano, M.; Nakajima, K.; Ohira-Kawamura, S.; Kikuchi, T.; Inamura, Y. *Phys. Rev. B* **2013**, *88*, 064405.
(52) Baker, M. L.; Tanaka, T.; Murakami, R.; Ohira-Kawamura, S.; Nakajima, K.; Ishida, T.; Nojiri, H. *Inorg. Chem.* **2015**, *54*, 5732.
(53) Long, J. R.; Yaghi, O. M. *Chem. Soc. Rev.* **2009**, *38*, 1213.
(54) Furukawa, H.; Go, Y. B.; Ko, N.; Park, Y. K.; Uribe-Romo, F. J.; Kim, J.; O'Keeffe, M.; Yaghi, O. M. *Inorg. Chem.* **2011**, *50*, 9147.
(55) Farha, O. K.; Eryazici, I.; Jeong, N. C.; Hauser, B. G.; Wilmer, C. E.; Sarjeant, A. A.; Snurr, R. Q.; Nguyen, S. T.; Yazaydın, A. Ö.; Hupp, J. T. *J. Am. Chem. Soc.* **2012**, *134*, 15016.
(56) Furukawa, H.; Cordova, K. E.; O'Keeffe, M.; Yaghi, O. M. *Science* **2013**, *341*, 1230444.
(57) Murray, L. J.; Dincă, M.; Long, J. R. *Chem. Soc. Rev.* **2009**, *38*, 1294.
(58) Sumida, K.; Rogow, D. L.; Mason, J. A.; McDonald, T. M.; Bloch, E. D.; Herm, Z. R.; Bae, T.-H.; Long, J. R. *Chem. Rev.* **2012**, *112*, 724.
(59) Corma, A.; García, H.; Llabrés i Xamena, F. X. *Chem. Rev.* **2010**, *110*, 4606.
(60) Kreno, L. E.; Leong, K.; Farha, O. K.; Allendorf, M.; Van Duyne, R. P.; Hupp, J. T. *Chem. Rev.* **2012**, *112*, 1105.
(61) Hendon, C. H.; Tiana, D.; Walsh, A. *Phys. Chem. Chem. Phys.* **2012**, *14*, 13120.
(62) Creutz, C.; Taube, H. *J. Am. Chem. Soc.* **1973**, *95*, 1086.
(63) Robin, M. B.; Day, P. Mixed Valence Chemistry-A Survey and Classification. In *Advances in Inorganic Chemistry and Radiochemistry*; Elsevier, 1968; Vol. 10, 247–422.
(64) Allen, G. C. and Hush, N.S. *Prog. Inorg. Chem.* **1967**, *8*, 357.
(65) D'Alessandro, D. M.; Keene, F. R. *Chem. Soc. Rev.* **2006**, *35*, 424.

(66) Hankache, J.; Wenger, O. S. *Chem. Rev.* **2011**, *111*, 5138.
(67) Bechlars, B.; D'Alessandro, D. M.; Jenkins, D. M.; Iavarone, A. T.; Glover, S. D.; Kubiak, C. P.; Long, J. R. *Nat. Chem.* **2010**, *2*, 362.
(68) Dei, A.; Gatteschi, D.; Pardi, L.; Russo, U. *Inorg. Chem.* **1991**, *30*, 2589.
(69) Jeon, I.-R.; Park, J. G.; Xiao, D. J.; Harris, T. D. *J. Am. Chem. Soc.* **2013**, *135*, 16845.
(70) DeGayner, J.; Jeon, I.-R.; Harris, T. D. *Chem. Sci.* **2015**, 1.
(71) Ward, M. D. *Inorg. Chem.* **1996**, *35*, 1712.
(72) Heinze, K.; Huttner, G.; Zsolnai, L.; Jacobi, A.; Schober, P. *Chemistry* **1997**, *3*, 732.
(73) Heinze, K.; Huttner, G.; Zsolnai, L. *Z. Naturforsch. B* **1999**, *54* (9), 1147.
(74) Carbonera, C.; Dei, A.; Létard, J.-F.; Sangregorio, C.; Sorace, L. *Angew. Chem. Int. Ed. Engl.* **2004**, *43*, 3136.
(75) Evangelio, E.; Ruiz-Molina, D. *Eur. J. Inorg. Chem.* **2005**, *2005*, 2957.
(76) Tao, J.; Maruyama, H.; Sato, O. *J. Am. Chem. Soc.* **2006**, *128*, 1790.
(77) Min, K. S.; Rheingold, A. L.; DiPasquale, A.; Miller, J. S. *Inorg. Chem.* **2006**, *45*, 6135.
(78) Min, K. S.; DiPasquale, A. G.; Golen, J. A.; Rheingold, A. L.; Miller, J. S. *J. Am. Chem. Soc.* **2007**, *129*, 2360.
(79) Guo, D.; McCusker, J. K. *Inorg. Chem.* **2007**, *46*, 3257.
(80) Min, K. S.; Swierczek, K.; DiPasquale, A. G.; Rheingold, A. L.; Reiff, W. M.; Arif, A. M.; Miller, J. S. *Chem. Commun.* **2008**, *3*, 317.
(81) Gaudette, A. I.; Jeon, I.-R.; Anderson, J. S.; Grandjean, F.; Long, G. J.; Harris, T. D. *J. Am. Chem. Soc.* **2015**, *137*, 12617.
(82) Caneschi, A.; Gatteschi, D.; Sessoli, R.; Rey, P. *Acc. Chem. Res.* **1989**, *22*, 392.
(83) Vaz, M. G. F.; Cassaro, R. A. A.; Akpinar, H.; Schlueter, J. A.; Lahti, P. M.; Novak, M. A. *Chem. Eur. J.* **2014**, *20*, 5460.
(84) Cassaro, R. A. A.; Reis, S. G.; Araujo, T. S.; Lahti, P. M.; Novak, M. A.; Vaz, M. G. F. *Inorg. Chem.* **2015**, *54*, 9381.
(85) Ishii, N.; Okamura, Y.; Chiba, S.; Nogami, T.; Ishida, T. *J. Am. Chem. Soc.* **2008**, *130*, 24.
(86) Benelli, C.; Caneschi, A.; Gatteschi, D.; Pardi, L.; Rey, P. *Inorg. Chem.* **1989**, *28*, 275.
(87) Benelli, C.; Caneschi, A.; Gatteschi, D.; Sessoli, R. *Adv. Mater.* **1992**, *4*, 504.
(88) Bogani, L.; Sangregorio, C.; Sessoli, R.; Gatteschi, D. *Angew. Chem. Int. Ed.* **2005**, *44*, 5817.
(89) Zheludev, A.; Grand, A.; Ressouche, E.; Schweizer, J.; Morin, B. G.; Epstein, A. J.; Dixon, D. A.; Miller, J. S. *Angew. Chem. Int. Ed.* **1994**, *33*, 1397.
(90) Miller, J. S.; Calabrese, J. C.; Rommelmann, H.; Chittipeddi, S. R.; Zhang, J. H.; Reiff, W. M.; Epstein, A. J. *J. Am. Chem. Soc.* **1987**, *109*, 769.
(91) Manriquez, J. M.; Yee, G. T.; McLean, R. S.; Epstein, A. J.; Miller, J. S. *Science* **1991**, *252*, 1415.
(92) Zhang, J.; Ensling, J.; Ksenofontov, V.; Gütlich, P.; Epstein, A. J.; Miller, J. S. *Angew. Chem. Int. Ed.* **1998**, *37*, 657.
(93) Pokhodnya, K. I.; Petersen, N.; Miller, J. S. *Inorg. Chem.* **2002**, *41*, 1996.
(94) McConnell, A. C.; Shurdha, E.; Bell, J. D.; Miller, J. S. *J. Phys. Chem. C* **2012**, *116*, 18952.
(95) Her, J.-H.; Stephens, P. W.; Pokhodnya, K. I.; Bonner, M.; Miller, J. S. *Angew. Chem.* **2007**, *119*, 1543.
(96) Ruiz, E.; Rodríguez-Fortea, A.; Alvarez, S.; Verdaguer, M. *Chem. Eur. J.* **2005**, *11*, 2135.
(97) Zhou, P.; Long, S. M.; Miller, J. S.; Epstein, A. J. *Phys. Lett. A* **1993**, *181*, 71.
(98) Morin, B. G.; Zhou, P.; Hahm, C.; Epstein, A. J.; Miller, J. S. *J. Appl. Phys.* **1993**, *73*, 5648.

(99) Pokhodnya, K. I.; Vickers, E. B.; Bonner, M.; Epstein, A. J.; Miller, J. S. *Chem. Mater.* **2004**, *16*, 3218.
(100) Du, G.; Joo, J.; Epstein, A. J.; Miller, J. S. *J. Appl. Phys.* **1993**, *73*, 6566.
(101) Prigodin, V. N.; Raju, N. P.; Pokhodnya, K. I.; Miller, J. S.; Epstein, A. J. *Adv. Mater.* **2002**, *14*, 1230.
(102) Yoo, J.-W.; Chen, C.-Y.; Jang, H. W.; Bark, C. W.; Prigodin, V. N.; Eom, C. B.; Epstein, A. J. *Nat. Mater.* **2010**, *9*, 638.
(103) Raju, N. P.; Prigodin, V. N.; Pokhodnya, K. I.; Miller, J. S.; Epstein, A. J. *Synth. Met.* **2010**, *160*, 307.
(104) Raebiger, J. W.; Miller, J. S. *Inorg. Chem.* **2002**, *41*, 3308.
(105) Schelter, E. J.; Morris, D. E.; Scott, B. L.; Thompson, J. D.; Kiplinger, J. L. *Inorg. Chem.* **2007**, *46*, 5528.
(106) Aumüller, A.; Erk, P.; Klebe, G.; Hünig, S.; Schütz, von, J. U.; Werner, H. P. *Angew. Chem. Int. Ed.* **1986**, *25*, 740.
(107) Kobayashi, A.; Kato, R.; Kobayashi, H.; Mori, T. *Solid State Commun.* **1987**, *64*, 45.
(108) Kato, R.; Kobayashi, H.; Kobayashi, A. *J. Am. Chem. Soc.* **1989**, *111*, 5224.
(109) Clérac, R.; O'Kane, S.; Cowen, J.; Ouyang, X.; Heintz, R.; Zhao, H.; Bazile, M. J.; Dunbar, K. R. *Chem. Mater.* **2003**, *15* (9), 1840.
(110) Motokawa, N.; Miyasaka, H.; Yamashita, M.; Dunbar, K. R. *Angew. Chem. Int. Ed.* **2008**, *47*, 7760.
(111) Miyasaka, H.; Motokawa, N.; Matsunaga, S.; Yamashita, M.; Sugimoto, K.; Mori, T.; Toyota, N.; Dunbar, K. R. *J. Am. Chem. Soc.* **2010**, *132*, 1532.
(112) Kosaka, W.; Liu, Z.; Miyasaka, H. *Dalton Trans.* **2018**, *46*, 248.
(113) Motokawa, N.; Matsunaga, S.; Takaishi, S.; Miyasaka, H.; Yamashita, M.; Dunbar, K. R. *J. Am. Chem. Soc.* **2010**, *132*, 11943.

Chapter 2: Electronic Conductivity, Ferrimagnetic Ordering, and Reductive Insertion Mediated by Organic Mixed-Valence in a Ferric Semiquinoid Metal–Organic Framework

2.1 Introduction

Long-range electronic communication and its consequent properties, including charge mobility and, if unpaired spins are present, magnetic coupling, are highly dependent on the distances between the participating atoms or ions within a material. As such, the realization of electronic conductivity and magnetic ordering in low-density materials presents an intriguing objective—one that is seemingly at odds with itself. Through reticular chemistry, metal-ligand bond strength has been used with remarkable success to produce extremely low-density, porous materials by design.[1] The resulting metal–organic frameworks are three-dimensional microporous materials composed of inorganic nodes and organic linkers. To date, this highly modular class of materials has proven most promising for applications in gas storage, separations, chemical sensing, and catalysis.[2] In contrast, engendering long-range charge transport and high-temperature magnetic ordering in this class of materials remains relatively unexplored. Mastery of these features could result in new applications for metal–organic frameworks as battery electrodes, thermoelectrics, electrochemical sensors, electrocatalysts, bulk magnets, and magnetoelectrics or multiferroics.[3,4] Recent advances in the field have taken advantage of methods such as π-π stacking, motifs with one-dimensional chains that promote short metal-metal distances, and donor-acceptor pairings to achieve electronic conductivity.[5] Moreover, study of two-dimensional frameworks exhibiting strong π-d conjugation has led to the observation of record electronic conductivities for metal–organic frameworks.[6] However, despite these notable examples, the field of metal–organic frameworks exhibiting non-insulating electronic structures presents an exciting and open research frontier.

While solid-state permanent magnets and most electronic conductors rely on band-type electronic structures constructed from itinerant electrons, most metal–organic frameworks are essentially ionic solids with large band gaps and little to no long-range electronic communication.[7] That is, their chemistry is localized and molecular in nature. Pervasive use of large diamagnetic linkers and oxophilic metal ions is in large part to blame. Although this combination helps promote framework stability, rigidity, and permanent porosity, it propagates large metal-metal distances, cutting off essential electronic exchange between the transition metal centered frontier orbitals responsible for charge transport and magnetic coupling.

The most promising means of gaining control over electronic structure in metal–organic frameworks is through the strategic manipulation of metal-ligand frontier orbital overlap and energy match. Judicious choice of metal and ligand, as well as the use of post-synthetic ion insertion, should enable control over electronic band gaps, carrier densities, magnetic coupling strength, and magnetic ordering behavior. To achieve a metal–organic framework with strong multi-dimensional electronic communication via this means, the metal and ligand should be open shell, have frontier orbitals of similar potential, and exhibit maximal orbital overlap to promote charge delocalization. While the topic of intramolecular electron exchange has long fascinated the molecular inorganic chemistry community, the bounty of metal-ligand combinations known to produce significant charge delocalization, with the exception of several variations on the valence-ambiguous nickel-dithiolene system, [6c-6f] has not yet been exploited in design of metal–organic frameworks.

One of the best-known redox-active organic moieties with frontier orbitals energetically similar to those of the transition metals is 2,5-dihydroxybenzoquinone.[8] Three valence states of this ligand (Figure 2.1) are accessible in a variety of metal–organic motifs.[8a] Transition metal-based systems containing the radical trianion $dhbq^{3-}$ reveal features characteristic of intramolecular charge delocalization, such as intervalence charge transfer bands in their electronic

absorption spectra and strong magnetic coupling.[9] Herein, we report a metal–organic framework constructed of Fe^{III} and mixed-valent $dhbq^{2-/3-}$ ligands that presents one of the highest conductivities yet observed for a metal–organic framework in addition to high-temperature magnetic interactions. We further demonstrate that this behavior is associated with the first instance of a Robin-Day Class II/III mixed-valency yet reported for a metal–organic framework. Finally, rare and precise control of reductive insertion within the porous structure is demonstrated to afford significant differences in electronic conductivity and magnetic coupling.

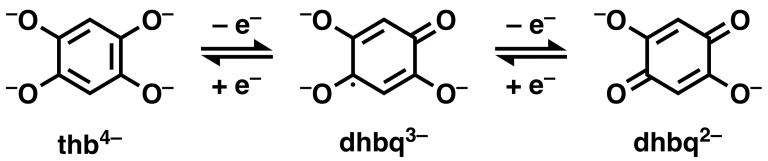

Figure 2.1. Redox states of linkers deriving from 2,5-dihydroxybenzoquinone that have previously been observed in metal–organic molecules or coordination solids. Notably, $dhbq^{3-}$ is a paramagnetic radical bridging ligand.

2.2 Experimental Information

General Information. All manipulations of $(NBu_4)_2Fe^{III}_2(dhbq)_3$ (**1**) following its initial synthesis were performed inside a N_2-filled glovebag or within the Ar atmosphere of a VAC Atmospheres glovebox. All reactions and subsequent manipulations for $Na_{0.9}(NBu_4)_{1.8}Fe^{III}_2(dhbq)_3$ (**2**) were performed within the Ar atmosphere of a VAC Atmospheres glovebox. Tetrahydrofuran (THF) was dried using a commercial solvent purification system designed by JC Meyer Solvent Systems and subsequently stored over 4-Å molecular sieves. The compound 2,5-diaminobenzoquinone was prepared from 2,5-diaminohydroquinone dihydrochloride following a published procedure.[10] The compound 2,5-diaminohydroquinone dihydrochloride (97%) was purchased from Alfa Aesar and used as received. The compounds $Fe(SO_4)\cdot 7H_2O$ (≥99%) and tetrabutylammonium bromide (≥98%) were purchased from Sigma-Aldrich and used as received. All other chemicals were purchased from commercial vendors and used as received. Carbon, hydrogen, and nitrogen analyses were obtained from the Microanalytical Laboratory at the University of California, Berkeley.

Synthesis of $(NBu_4)_2Fe^{III}_2(dhbq)_3$ (1). A suspension of 20.0 mg (0.144 mmol) of 2,5-diaminobenzoquinone, 121 mg of $Fe(SO_4)\cdot 7H_2O$ (0.434 mmol), and 250 mg of tetrabutylammonium bromide (0.775 mmol) in 3.0 mL of deionized water titrated to a pH of 3.0 with concentrated HCl was loaded into a thick-walled borosilicate tube. The reaction suspension was degassed via four freeze-pump-thaw cycles, following which the tube was flame-sealed and loaded into an oven set to 120 °C. *Caution*: improperly flame-sealed glass vessels may burst if heated above the boiling point of the reaction solvents they contain. The suspension was heated at 120 °C for 24 h, at which point the tube was removed from the oven and allowed to cool to room temperature. After cooling, the resulting black cubic crystals were recovered via vacuum filtration inside a N_2-atmosphere glovebag. The product was dried by heating the solid crystals at 150 °C under reduced pressure for 1 h. Yield: 21.0 mg, 43%. Anal. Calcd for $C_{50}H_{78}Fe_2N_2O_{12}$: C, 59.41; H, 7.78; N, 2.77. Found: C, 59.19; H, 7.87; N, 2.93. IR (solid-ATR): 2956 (w), 2929 (w), 2869 (w), 2731 (w), 2538 (w), 1804 (w), 1488 (s), 1470 (s), 1364 (s), 1291 (m), 1270 (m), 1244 (s), 1208 (s), 1025 (m), 884 (m), 860 (s), 830 (m), 807 (s), 758 (m), 731(m).

Synthesis of $Na_{0.9}(NBu_4)_{1.8}Fe^{III}_2(dhbq)_3$ (2). Prior to chemical reduction, cubic crystals of **1** were ground into a microcrystalline powder using a mortar and pestle in an Ar-atmosphere glovebox. Then, a stirred suspension of 50 mg (0.049 mmol) of **1** in 3.0 mL of THF was prepared. Na-naphthalenide was prepared by stirring 6.3 mg (0.049 mmol) of naphthalene ($C_{10}H_8$) over a roughly ten-fold excess of sodium metal in 2.0 mL of THF for 3 h. The resulting solution was filtered and added drop-wise to the stirred suspension of **1** in THF at room temperature. The mixture was stirred for 12 h, after which **2** was recovered as a brown microcrystalline powder by vacuum filtration, washed with 2 × 2.0 mL of THF, and dried for 1 h under reduced pressure. ICP analysis indicated that 0.9 molar equivalents of Na^+ ions were introduced per mole of **1**. Low percentages of C and H in elemental analysis indicated that roughly 10% of $(NBu_4)^+$ ions had been exchanged for Na^+. Thus, the true level of reduction in **2**, or otherwise stated the number of electrons introduced into framework **1**, was 0.7 e^- per mole of **1**. Two independently synthesized batches of **2** yielded identical elemental and ICP analyses. Yield: 46.0 mg, 96%. Anal. Calcd for $C_{46.8}H_{70.8}Fe_2N_{1.8}Na_{0.9}O_{12}$: C, 57.18; H, 7.26; N, 2.56. Found: C, 56.91; H, 7.07; N, 3.02. ICP Found: Fe:Na, 2.23(1):1. IR (solid-ATR): 2957 (w), 2931 (w), 2870 (w), 2738 (w), 2545 (w), 1820 (w), 1489 (s), 1470 (s), 1372 (s), 1292 (m), 1270 (m), 1246 (s), 1208 (s), 1026 (m), 876 (m), 861 (s), 830 (m), 807 (s), 758 (m), 731(m).

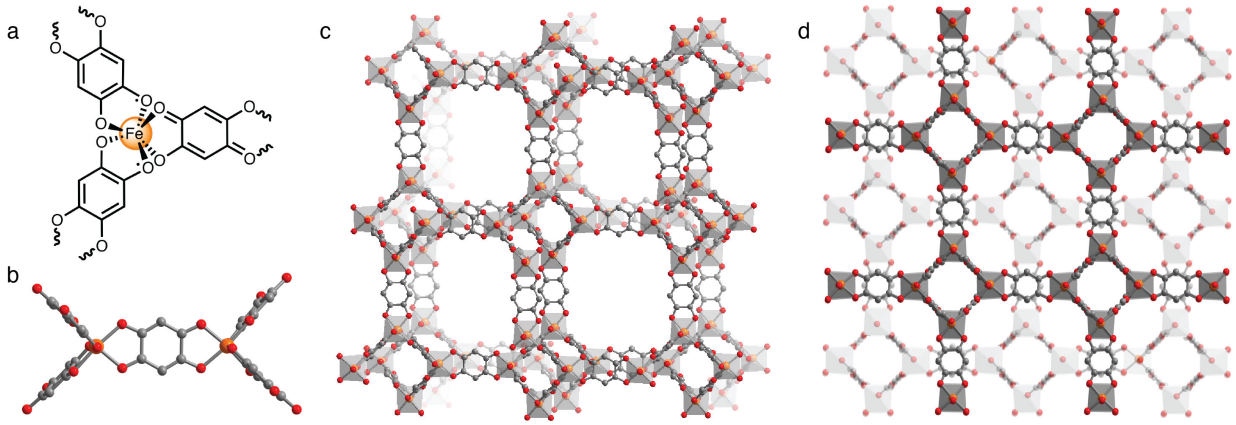

Figure 2.2. (a) Illustration of a single Fe^{III} center in **1**, showing that two radical ($dhbq^{3-}$) bridging ligands and one diamagnetic ($dhbq^{2-}$) bridging ligand are coordinated to each metal site. (b) A portion of the crystal structure of **1,** illustrating the local environment of two $dhbq^{n-}$-bridged Fe^{III} centers. (c) A larger portion of the crystal structure of **1**, showing one of the two interpenetrated (10,3)-*a* nets that together generate the porous three-dimensional structure. (d) The two interpenetrated (10,3)-*a* lattices of opposing chiralities that together compose **1**. Charge balancing NBu_4^+ cations are not depicted for clarity.

2.3 Results and Discussion

Synthesis and Characterization of $(NBu_4)_2Fe^{III}_2(dhbq)_3$ (1). Synthesis of **1** was performed under anaerobic conditions using the ligand 2,5-diaminobenzoquinone, which undergoes *in situ* hydrolysis to become $dhbq^{2-}$. The reaction of three molar equivalents of $Fe(SO_4)\cdot 7H_2O$ with one equivalent of 2,5-diaminobenzoquinone and excess tetrabutylammonium bromide in

deoxygenated water for 24 h at 120 °C afforded **1** as black cube-shaped crystals. Attempts to synthesize **1** starting with H_2dhbq rather than 2,5-diaminobenzoquinone only produced amorphous brown or black solids. The monohydrate of **1**, with the oxidation state assignment $(NBu_4)_2[Fe^{II}_2(dhbq^{2-})_3]\cdot H_2O$, was previously reported in Ref 11. However, in our hands, some modification on this reported synthesis was required in order to obtain phase-pure **1**. Notably, if **1** was prepared under pH-neutral conditions, an unidentified ferromagnetic impurity, likely some form of Fe_2O_3, was co-precipitated with **1**, preventing an unqualified magnetic analysis.

The structure of **1** was elucidated using single-crystal x-ray analysis. The compound crystallizes in the cubic space group $I\bar{4}3d$ as two interpenetrated (10,3)-*a* nets of opposing chiralities (Figure 2.2d). In this topology, which is rare for $dhbq^{2-}$-based coordination solids,[11,12] neighboring metal centers within each lattice of **1** are all of the same chirality (Figure 2.2b and 2.2c), generating a three-dimensional structure. This differs from the classic two-dimensional honeycomb structure-type frequently observed for coordination solids of $dhbq^{2-}$ and derivative ligands, in which neighboring metal centers are of opposing chiralities.[13] The tetrabutylammonium countercations in **1** were located crystallographically inside the pores and appear to be filling the pores near completely, with no large voids present. Interestingly, preliminary attempts at forming materials with the topology of **1** but with smaller countercations, such as tetrapropylammonium or methyltributylammonium, have thus far proven unsuccessful. This may imply that the tetrabutylammonium cations are crucial to templating the three-dimensional structure of **1**, as transition metal coordination solids containing the $dhbq^{2-}$ ligand typically adopt one- or two-dimensional structures.[8a,13,14] Similar cation-dependent morphology changes have been observed for transition metal-oxalate coordination solids with the analogous chemical formula $[A^+]_2M^{II}_2(ox)_3$.[15] Two adsorption isotherms, 77-K N_2 and 195-K CO_2, were performed for **1** after heating at 150 °C under vacuum for 1 h, with both measurements confirming a lack of microporosity (Figure S2.1).

While an early indication of the intervalence charge-transfer present in **1** came from its black color, as coordination solids composed solely of the dianionic $dhbq^{2-}$ ligand are typically bright or dark red,[8a,10] the crystal structure analysis provided additional evidence that electron transfer had taken place during synthesis (Table S2.1 and Figure S2.2). The Fe-O distances in **1** are 2.008(7) Å and 2.031(7) Å, significantly shorter than the Fe-O distances in Fe^{II}-based molecules and coordination solids containing dhbq-type ligands.[8a,9,16] Additionally, C-O distances for the $dhbq^{n-}$ ligands in **1** are slightly longer (1.281(11) Å, 1.308(12) Å) than those observed for $dhbq^{2-}$ coordination complexes (typically in the 1.26-1.29 Å range).[8a]

Mössbauer spectroscopy was used to unequivocally establish the oxidation state of the iron centers in **1**. At 100 K, the ^{57}Fe Mössbauer spectrum (Figure 2.3) is comprised of a doublet with an isomer shift of δ = 0.574(2) mm/s, a quadrupole splitting of $|\Delta E_Q|$ = 1.279(5) mm/s, and a line width of Γ = 0.326(8) mm/s (Figure 2.3, top). These parameters are similar to those of other high-spin Fe^{III} compounds; the isomer shift, in particular, is quite close to those exhibited by mononuclear high-spin Fe^{III} molecules ligated by three semiquinones.[17] The large quadrupole splitting is consistent with the extensive π-bonding presumed to occur in the compound. The Mössbauer spectrum does not show any significant changes across the temperature range 20 to 300 K. Below 20 K, however, a poorly resolved sextet begins to appear as a consequence of magnetic ordering in **1**.

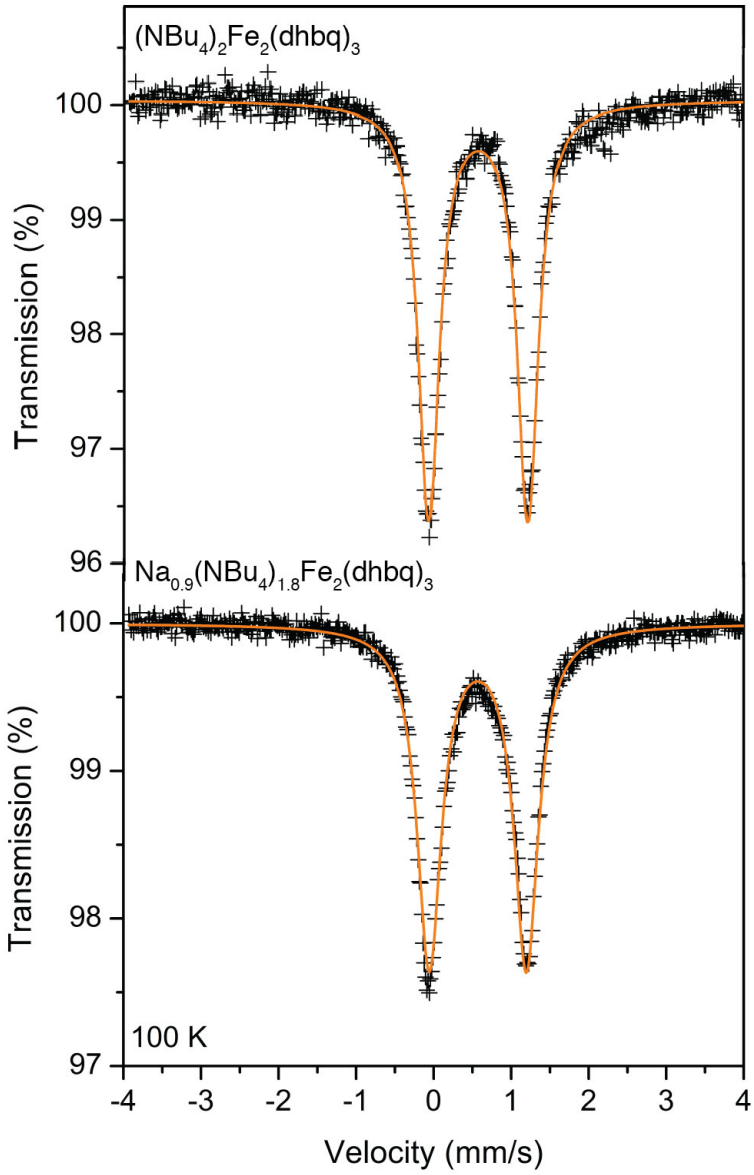

Figure 2.3. ^{57}Fe Mössbauer spectra for **1** (top) and **2** (bottom) at 100 K, with the fits to the spectra shown in orange. Both fits have parameters consistent with high-spin Fe^{III}.

The observations made from crystallographic analysis and Mössbauer spectroscopy led to the assignment of **1** as $(NBu_4)_2\,Fe^{III}_2(dhbq)_3$. Concomitant with the assignment of the iron centers as trivalent is the assumption that at least some of the $dhbq^{n-}$ ligands are spontaneously reduced by Fe^{II} during the synthesis in order to generate a charge-balanced material. Separate one-electron redox couples for $dhbq^{2-}/dhbq^{3-}$ and $dhbq^{3-}/thb^{4-}$ have been observed in previous work on $dhbq^{2-}$-containing molecules.[9] Thus, the ligands in **1** were assumed to be a combination of the $dhbq^{2-}$ and the organic radical $dhbq^{3-}$ oxidation states. Ignoring the possibility of ligand-based redox non-innocence, in order to achieve charge balance, the ligand redox states should be a 2:1 ratio of $dhbq^{3-}$ to $dhbq^{2-}$ (Figure 2.2a).

Slow-Scan Cyclic Voltammetry. In order to better understand the redox behavior of **1**, slow-scan cyclic voltammetry (SSCV) was performed. This technique, while in common use for

inorganic intercalation solids, has passed largely unutilized for redox-active metal–organic frameworks. This may be the result of the assumption that most metal–organic frameworks are completely insulating, prompting the use of fast-scanning CV techniques that only investigate redox activity at the crystallite surface. However, a number of recent reports have addressed the reductive insertion of lithium ions in certain metal–organic frameworks using galvanostatic methods.[18]

A voltammogram of **1** using lithium reference and counter electrodes in 0.1 M $LiBF_4$ in propylene carbonate was collected at a scan rate of 30 μV/s (Figure 2.4). Given a tentative composition of $Li_x[NBu_4]_2Fe^{III}_2(dhbq)_3$, the material could be reduced to $x = 3.7$ quasi-reversibly with 77% Faradaic efficiency. Despite this relatively low Faradaic efficiency for a reductive insertion reaction, we were encouraged by the possibility of reducing **1** to a composition with a radical located on every ligand in the framework. Integration of the first quasi-reversible peak corresponds to 1.1 electrons per mole of **1**. This one-electron couple likely corresponds to reduction of the remaining $dhbq^{2-}$ ligand in **1** to a $dhbq^{3-}$ radical. Moreover, the total reduction activity observed, close to four electrons per mole of **1**, is postulated to correspond to solely ligand-based reduction activity, since a four-electron reduction would correspond to reduction of all three $dhbq^{n-}$ ligands to the thb^{4-} oxidation state. As discussed below, these expectations are consistent with chemical reduction reactions using sodium naphthalenide as a stoichiometric reductant, as probed via Mössbauer spectroscopy of the resulting products. In light of the results from the chemical reductions, we expected the $Fe^{II/III}$ redox manifold to be accessible at more reducing potentials. Unfortunately, however, attempts to electrochemically reduce the material beyond $x = 3.7$ resulted in decomposition of the framework.

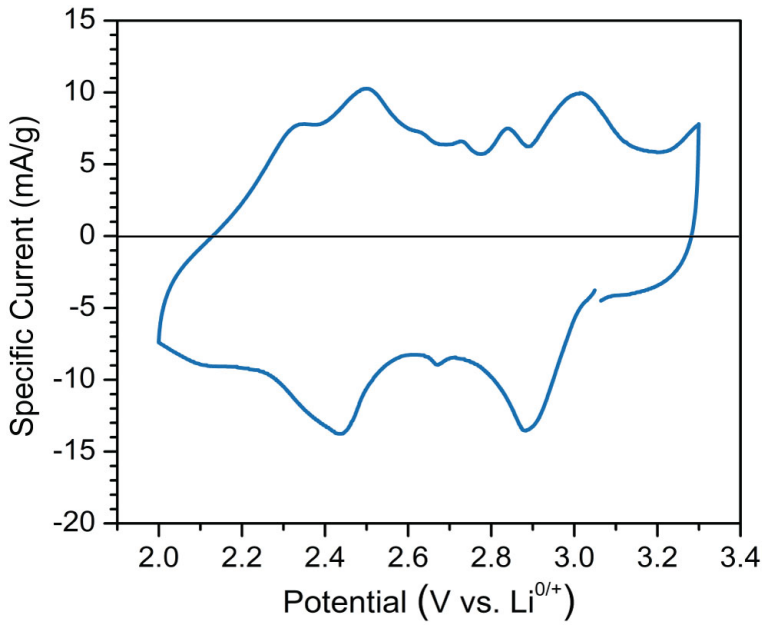

Figure 2.4. Slow-scan cyclic voltammetry of **1**. Lithium reference and counter electrodes were used with an electrolyte solution of 0.1 M $LiBF_4$ in propylene carbonate. A scan rate of 30 μV/s was used. The data shown uses the IUPAC current convention.

Chemical Reduction of 1. A one-electron chemical reduction of **1** was pursued using a stoichiometric amount of sodium naphthalenide in THF. The recovered product was studied using

ICP analysis and discovered to have a Fe:Na ratio of 2.23(1):1. In addition, elemental analysis revealed low amounts of carbon and hydrogen, indicating a small exchange (10%) of NBu_4^+ cations for Na^+. The combination of these analyses supports an assignment of the formula unit of the reduced material as $Na_{0.9}(NBu_4)_{1.8}Fe_2(dhbq)_3$ (**2**), which corresponds to a 0.7 e^-/mol reduction of **1**. The reduced framework shows a highly crystalline powder x-ray diffraction pattern that almost perfectly overlays with that simulated for **1**, indicating little if any change in unit cell (Figure S2.3).

The Mössbauer spectrum of **2** (Figure 2.3, bottom) also shows little change compared to that of **1**, indicating that the ligands, not the Fe^{III} centers, were reduced during the chemical reduction. Compound **2** exhibits an isomer shift of δ = 0.570(3) mm/s, a quadrupole splitting of $|\Delta E_Q|$ = 1.252(7) mm/s, and a line width of Γ = 0.381(6) mm/s, compared to the values of δ = 0.574(2) mm/s and $|\Delta E_Q|$ = 1.279(5) mm/s observed for **1**. Again ignoring possible ligand-based redox non-innocence, in order to achieve a charge balanced material the ligand redox states in **2** should be a 2.7:0.3 ratio of $dhbq^{3-}$ to $dhbq^{2-}$. Notably, the iron sites in this material are close to fully bridged by the radical trianion linker $dhbq^{3-}$.

A further chemical reduction was performed using four equivalents of sodium naphthalenide per mole of **1** (see the Supporting Information) in order to determine whether the redox chemistry observed in the electrochemical analysis was entirely ligand-based, or partially metal-based. ICP analysis indicated that the resulting product has a putative chemical formula of $Na_{3.2}(NBu_4)_{1.8}Fe^{III}_2(dhbq)_3$. As with **2**, the resulting powder x-ray diffraction pattern almost perfectly overlays with that of **1** (Figure S2.4). Mössbauer spectroscopy revealed two iron sites (Figure S2.5). The first site, accounting for 51% of the iron centers, exhibits δ = 0.47(3) mm/s, $|\Delta E_Q|$ = 0.79(2) mm/s, and Γ = 0.50(5) mm/s, while the second site, corresponding to 49% of the iron centers, exhibits δ = 0.58(1) mm/s and $|\Delta E_Q|$ = 1.26(3) mm/s, and Γ = 0.36(2) mm/s. Since both sites have parameters consistent with Fe^{III}, chemical reduction of **1**—at least up to 3 equivalents of Na^+ per mole—is ligand-based, generating first $dhbq^{3-}$ and then thb^{4-} ligands. On the basis of its hyperfine parameters, the first site could possibly be assigned to low-spin Fe^{II}, but at this time, the assignment to high-spin Fe^{III} is preferred. This further chemical reduction of **1** in addition to other chemical reductions beyond 0.7 e^-/mol of **1** are still under investigation due to the presence of multiple iron sites lending additional complexity to their electronic structures. Thus, only frameworks **1** and **2** will be discussed further here.

Infrared Spectroscopy. With the valency of the iron cations in **1** and **2** established, the valence of the ligands was further studied using infrared spectroscopy. The spectrum of **1** (Figure 2.5) presents strong near-IR absorption suggestive of intervalence charge transfer. In addition, the high degree of asymmetry of the peaks in the spectra for **1** and **2** is likely due to significant coupling of electronic modes to vibronic modes, a feature also associated with intervalence charge transfer (IVCT). Crucially, both spectra display a very broad peak over 1510-1450 cm^{-1}, which we assign to the C=O stretching vibration. This stretch is typically much sharper and at higher wavenumbers for materials containing only the $dhbq^{2-}$ ligand.[8a] Moreover, in $dhbq^{2-}$-containing molecules, this stretch is typically observed to shift to lower energy by ~50 cm^{-1} when reduced to $dhbq^{3-}$.[9] Thus, the appearance of one broad stretch or possibly two overlapping stretches across the 1510-1450 cm^{-1} region supports assignment of the $dhbq^{n-}$ ligands as $dhbq^{2-/3-}$. This broad C=O stretch, in addition to the strong absorbance in the near-IR region, encouraged further investigation of ligand intervalence using UV-Vis-NIR spectroscopy.

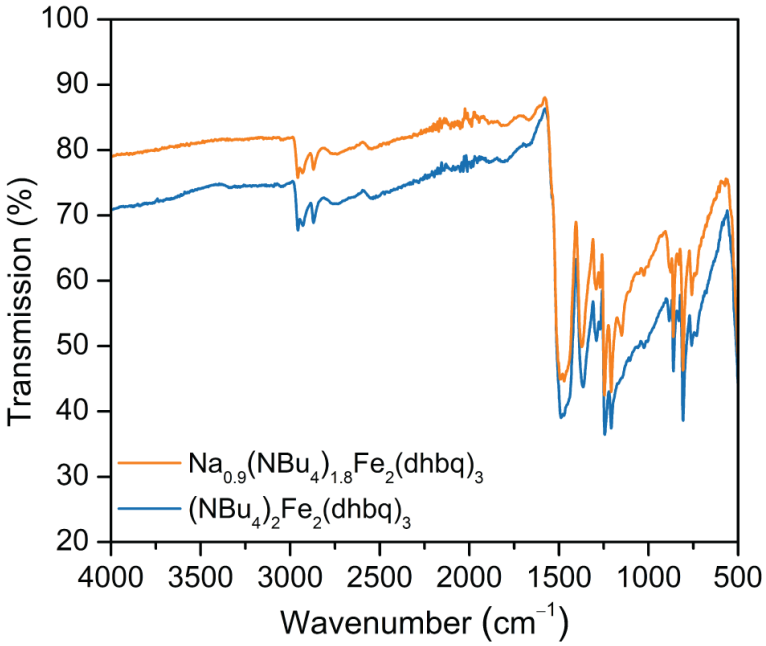

Figure 2.5. Solid-ATR infrared spectra of **1** and **2** shown in blue and orange, respectively.

UV-Vis-NIR Diffuse Reflectance Spectroscopy. The electronic absorption spectra of **1** and **2** (Figure 2.6) show a broad absorbance extending across the range 4500 to 14000 cm^{-1}, with ν_{max} = 7000 and 6300 cm^{-1}, respectively. These intense absorption features are attributed to ligand-based IVCT. Notably, a solid-state UV-Vis-NIR spectrum of a molecular Fe^{III} semiquinone-catecholate compound shows a similar, though narrower, IVCT band at ν_{max} = 5200 cm^{-1}.[19] Since all of the iron centers in **1** and **2** were confirmed to be trivalent by Mössbauer spectroscopy, the origin of the IVCT must be the organic $dhbq^{2-/3-}$ moieties. Interestingly, in both cases the bands display a very sharp absorption edge at low energy (4500 cm^{-1}), one of the best-known signatures of Robin-Day Class II/III mixed-valency.[20] This represents the first observation of a Class II/III mixed-valency in a metal–organic framework of which we are aware, and provides a definitive signature of strong electronic correlation within these materials. A higher energy absorbance observed at 21500 cm^{-1} is tentatively assigned to a π-π* transition, though the feature may also be due to ligand-to-metal charge transfer (Figure S2.6). The observation of a low-lying IVCT band in the electronic absorption spectra of **1** and **2** is indicative of thermally activated charge transport within the lattice, and this motivated us to explore the electronic conductivity of these materials.

Metal–organic frameworks seldom exhibit either metal[5d,18,21] or ligand[5c,5f,6c,18,22] redox activity, and control of the redox states in a framework is even more rarely achieved. Post-synthetic chemical redox reactions of metal–organic frameworks are typically performed using a large excess of a redox reagent or not quantified, making full characterization of the resulting products difficult. Also, the majority of ligand redox activity observed in metal–organic frameworks thus far has been characterized using spectroelectrochemical measurements, in contrast to post-synthetic analysis of bulk redox reaction products. Thus, the synthesis of **1** and **2** provided a unique opportunity to study a pair of materials with precise chemical redox states and correlate their electronic and magnetic behaviors.

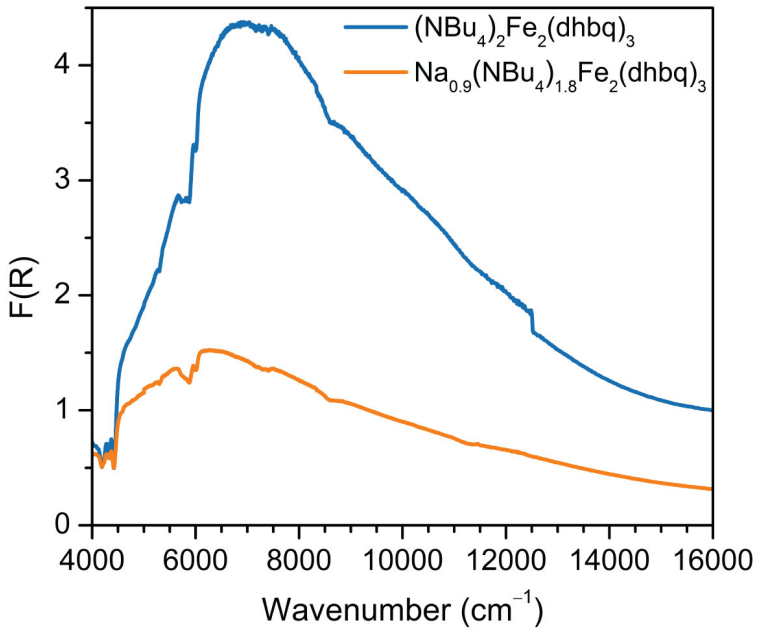

Figure 2.6. Diffuse reflectance UV-Vis-NIR spectra of **1** and **2** shown in blue and orange, respectively. F(R) is a Kubelka-Munk conversion of the raw diffuse reflectance spectrum.

Electronic Conductivity. Electronic conductivity was investigated via two-point dc conductivity measurements performed on pressed pellets of **1** and **2**. For compound **1**, a room-temperature conductivity of 0.16(1) S/cm was determined and found to be Ohmic within ±1 V of open circuit. To the best of our knowledge, this is the highest conductivity value yet observed for a three-dimensionally connected metal–organic framework. While several higher values have been reported for lamellar solids, the mode of conductivity in these materials is often attributed to π-d conjugation through square planar metal centers.[6f] To date, no clear strategy of extending this mechanism to three-dimensional solids has emerged. In contrast, compound **2** was found to be considerably less conductive, exhibiting a conductivity of 0.0062(1) S/cm at 298 K.

The foregoing results suggest a mode of conductivity consistent with electron hopping within the $dhbq^{2-/3-}$ redox manifold. Considering the reduction to yield **2**, this model would agree that with population of the $dhbq^{2-}$ vacancies, such that fewer unpaired electrons on radical $dhbq^{3-}$ linkers have a nearest neighbor $dhbq^{2-}$ vacancy to hop to, the carrier mobility and in turn the conductivity should indeed decrease. As such, fractional oxidation of **1** could be expected to yield even higher conductivities. Unfortunately, clean synthetic conditions for the oxidative deinsertion of the tetrabutylammonium cations have not yet been identified.

Variable-temperature conductivity measurements were performed in the temperature range 70-300 K. Both **1** and **2** were confirmed to be semiconducting with an Arrhenius temperature dependence. An Arrhenius fit to the data revealed an activation energy of just 110 meV for **1** (Figure 2.7, Figures S2.7 and S2.8). In contrast, a considerably larger activation energy of 180 meV was obtained for **2** (Figure 2.7, Figures S2.7, S2.8, and S2.9). The stronger temperature dependence of the conductivity for **2** is again consistent with a further divergence of the $dhbq^{3-}$ to $dhbq^{2-}$ ligand ratio from the optimal mixed-valence ratio of 1:1.

While it is expected that the conductivity results obtained by two-point pressed pellet measurements may be limited by crystallite boundaries and electrode contacts, the activation energies of **1** and **2** are of reasonable magnitude to be consistent with the broad low energy

absorption bands observed in the infrared and UV-Vis-NIR spectra. The cubic symmetry of the conduction pathway is quite rare for conductive coordination solids. It was found to be advantageous in this case, however, owing to mitigation of the texturing effects often observed in pressed pellet measurements of one- and two-dimensional conductors. A final consideration is that while the carrier mobility should decrease as the stoichiometry moves further from that of optimal mixed-valence, the charge carrier density should increase as more $dhbq^{2-}$ ligands are reduced to the radical $dhbq^{3-}$ species. Our present work suggests that charge carrier mobility is the greater predictor of conductivity in these materials, as **2** has a decreased conductivity compared to **1**.

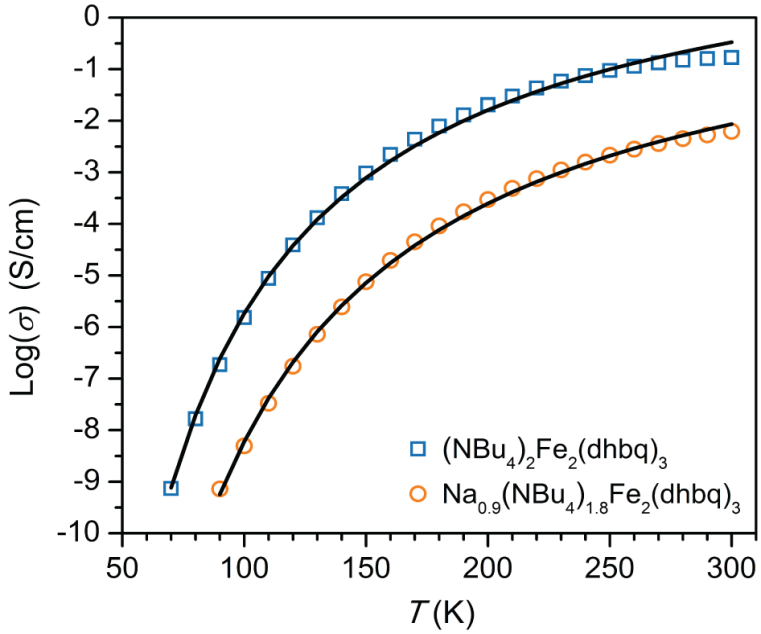

Figure 2.7. Variable-temperature conductivity data for **1** and **2**, shown by blue squares and orange circles, respectively. Arrhenius fits to the data are shown by black lines.

Magnetic Properties. Concurrently, the presence of $dhbq^{3-}$ radicals in **1** and **2** prompted us to investigate their magnetic behaviors. Previously studied metal–organic materials with transition metals bridged by organic radicals have demonstrated strong magnetic coupling, leading to high-temperature magnetic ordering.[23] The most famous example is the room-temperature magnet $V(TCNE)_2 \cdot xCH_2Cl_2$ (TCNE = tetracyanoethylene).[24] Variable-temperature dc magnetic susceptibility measurements of **1** under an applied magnetic field of 0.1 T revealed strong metal-radical magnetic interactions, eventually leading to magnetic ordering at 8 K (Figure 2.8, top). The ordering temperature, confirmed using ac magnetic susceptibility measurements (Figure S2.10), was significantly lower than anticipated based on the strong magnetic coupling that has previously been observed in Fe^{III}-$dhbq^{3-}$ molecules.[9c] However, strong deviations from Curie-Weiss behavior below 250 K shed some light onto the low magnetic ordering temperature (Figure 2.8, middle). Such deviations from Curie-Weiss behavior have been previously observed in systems with strong π-d interactions,[25] and previously attributed to local magnetic order (in contrast to bulk magnetic ordering) or competing ferromagnetic and antiferromagnetic interactions leading to magnetic glassiness,[26] both of which could be present in **1**.

A Curie-Weiss fit of the inverse magnetic susceptibility data for **1** from 250 K to 300 K results in a Curie temperature of θ = 134 K and a Curie constant of C = 6.1 emu·K/mol. The positive

Curie temperature reveals that ferromagnetic interactions are dominant at high-temperature in **1**, and its magnitude suggests that quite high temperature magnetic coupling occurs in **1**. In contrast, the magnetic behavior at low temperature indicates that ferrimagnetic coupling predominates. The shape of the magnetization (Figure S2.11) versus temperature from 40 to 2 K is a gradual, nearly linear increase, rather than the sharp increase and magnetization saturation typically associated with bulk ferromagnets. In addition, low temperature magnetic hysteresis data reveal a saturation magnetization of 7.3 μ_B/mol, much closer to the 8.94 μ_B/mol expected for ferrimagnetic coupling rather than the 10.95 μ_B/mol expected for ferromagnetic coupling. Thus, the low magnetic ordering temperature of **1** is attributed to a competition of ferromagnetic and antiferromagnetic interactions that prevents true three-dimensional order, until antiferromagnetic metal-radical interactions and thus bulk ferrimagnetic order prevails at low temperature.

Compound **2**, which is much closer to a fully $dhbq^{3-}$-bridged framework, was expected to show an increased magnetic ordering temperature due to the greater number of paramagnetic linkers. Indeed, a higher magnetic transition temperature of 12 K was observed, as determined using ac magnetic susceptibility measurements (Figure S2.10). The room-temperature product of magnetic susceptibility and temperature ($\chi_M T$) for **2** is 11.2 emu·K/mol, compared to 10.9 emu·K/mol for **1**. Accordingly, the difference between the two frameworks is 0.3 emu·K/mol at 300 K, close to the 0.26 emu·K/mol difference expected with addition of 0.7 equivalents of an $S = ½$ spin, assuming magnetically isolated metal and radical spins. Moreover, Curie-Weiss analysis of the magnetic susceptibility data for **2** in the temperature range 250 to 300 K results in θ =144 K and C = 5.90 emu·K/mol (Figure 2.9). The higher Curie temperature as compared to **1** is in keeping with the greater density of magnetic exchange interactions expected for **2**.

Finally, low temperature (2 K) magnetic hysteresis measurements reveal that **2** is a harder magnet than **1**, with coercive fields of 350 Oe and 100 Oe observed, respectively (Figure 2.8, bottom). The saturation magnetization (Figure S2.12) of **2** is 7.11 μ_B/mol, lower than that of **1**, as expected due to the additional ligand radical spins coupling antiferromagnetically to the Fe^{III} centers, and close to the predicted value of 7.94 μ_B/mol for ferrimagnetic coupling. The lower than predicted saturation magnetization values of both **1** and **2** at low temperature are attributed to antiferromagnetic interactions between the two sublattices that comprise the framework. In general, the conflict between the high Curie temperatures observed for **1** and **2** and their comparatively low magnetic ordering temperatures can potentially be resolved by counterion changes. Altering the counter-ion A^+ in the two-dimensional materials $[A^+]Fe^{II}Fe^{III}(oxalate)_3$, for example, has been shown to shift their magnetic ordering temperatures across a temperature range of 17 K.[23,27]

Interestingly, the foregoing results qualitatively adhere to the relation between the number of magnetic neighbors (z) and magnetic ordering temperature, $T_C \propto z$, first introduced by Néel and later popularized during magnetic studies of Prussian blue analogues.[28] As a result, we believe there is an exciting future in chemically tuning metal–organic radical frameworks to maximize the number of magnetic neighbors and the magnitude of metal-radical magnetic coupling in order to achieve high-temperature magnetic ordering.

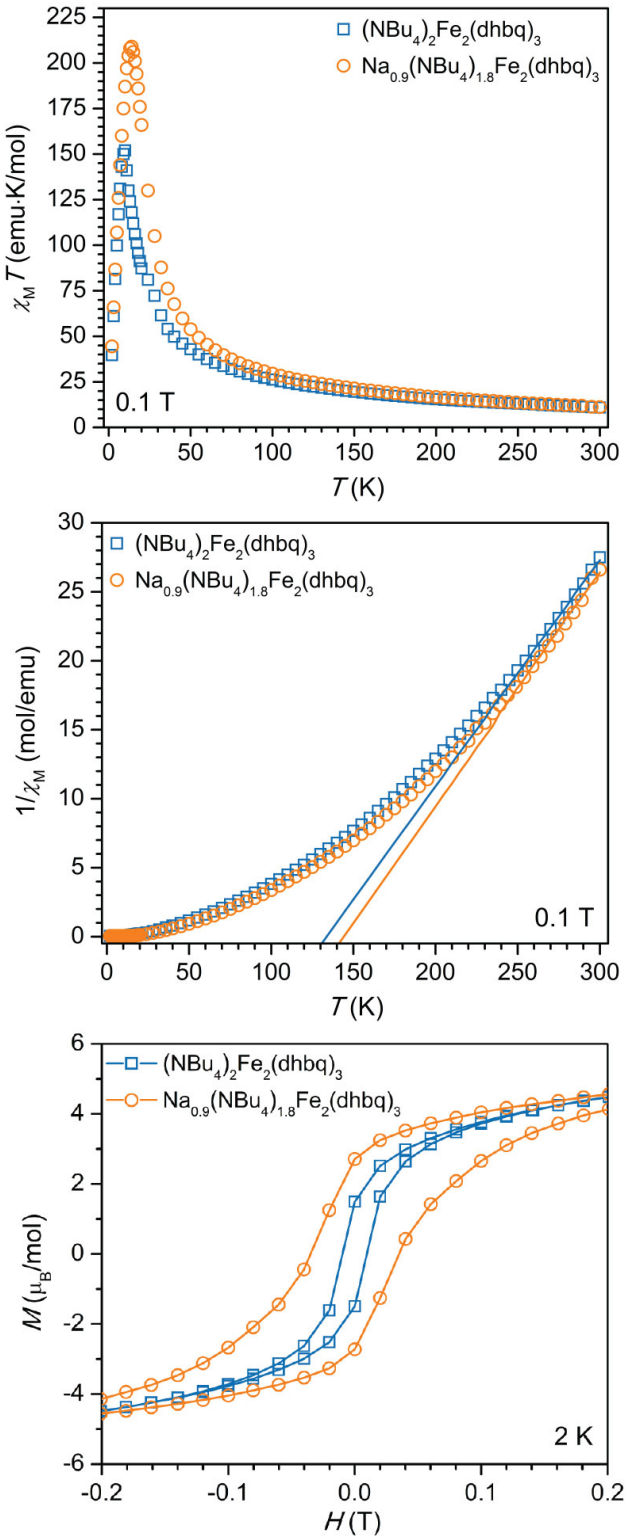

Figure 2.8. Top: Dc magnetic susceptibility data for **1** and **2** represented by blue squares and orange circles, respectively. Middle: Inverse of magnetic susceptibility versus temperature for **1** and **2**. Curie-Weiss fits to the data in the temperature range 250-300 K are shown by solid blue and orange lines for **1** and **2**, respectively. Bottom: Magnetization (*M*) versus applied dc magnetic field (*H*) data for **1** and **2** in blue and orange, respectively. Hysteresis loops were recorded at a sweep

rate of 2 mT/s. Solid lines are guides for the eye. Figure S2.12 shows the full hysteresis loops in an applied dc magnetic field range of –7 T to 7 T.

2.4 Conclusions and Outlook

Overall, the work herein extends the oft-praised tunability of metal–organic frameworks to affect electronic structure, enabling control over bulk electronic and magnetic properties. Ongoing efforts are directed towards altering the transition metal, linker substituents, and charge-balancing cations in **1** to control the mixed-valency behavior, provoking changes in magnetic ordering temperature and electronic conductivity. In addition, we believe that further work on the transition metal-semiquinoid framework studied here could potentially expose new applications for metal–organic frameworks. For instance, organic mixed-valence has long been considered an appealing means for achieving high gravimetric density electrochemical energy storage, despite the common pitfall of large structural changes upon reduction or oxidation that result in limited cyclability.[29] Metal–organic frameworks with redox-active linkers can circumvent this issue since the redox-active moieties are locked within a rigid metal-ligand lattice. While the materials studied here show only quasi-reversible ligand redox couples, ion exchange of the tetrabutylammonium ions for smaller cations may engender permanent porosity in **1**, allowing for ion-insertion with enhanced reversibility. Further, chemical oxidation of **1** to the charge neutral $Fe^{III}_2(dhbq^{2-})_3$ formula could result in a metal–organic framework whose pores are filled only by solvent. This hypothetical material is predicted[30,31] to have a large accessible surface area of 5070 m^2/g upon activation and could likely support both cation and anion insertion. Overall, the $Fe_2(dhbq)_3$ system could potentially exhibit up to 8 electrons per formula unit of redox activity, making it an intriguing candidate for metal–organic framework-based electrodes.

Furthermore, magnetic ordering and semiconducting or metallic behaviors typically stem from separate sub-lattices when observed in the same coordination solid, such as in tetrathiafulvalene salts with paramagnetic counterions.[32] In contrast, materials like **1** and **2**, for which the electronic and magnetic properties extend from the same origin (in this case ligand mixed-valency), present an especially valuable opportunity to pursue magnetoelectric or multiferroic metal–organic frameworks.

In conclusion, the foregoing work demonstrates a rare example of a metal–organic framework composed of metal ions bridged by paramagnetic linkers that additionally displays ligand mixed-valency. The effects of ligand-mixed valency on the electronic, magnetic, and ion-insertion behaviors of the framework have been explored. Importantly, the electronic conductivities obtained are some of the highest yet observed for metal–organic frameworks, indicating that ligand mixed-valency can serve as a highly effective charge transport mechanism within metal–organic frameworks. Also included is one of the first instances of post-synthetic chemical redox control over a metal–organic framework. Specifically, control over the ligand redox states in the framework was established using post-synthetic chemical redox reactions, resulting in synthesis of a 0.7-electron reduction of framework **1.** Correlated changes in electronic conductivity and magnetic ordering temperature were observed for the two frameworks. Explicitly, this work establishes the transition metal-semiquinoid system as a promising scaffold for delocalized and tunable electronic structures in metal–organic frameworks. More broadly, it highlights the technique of post-synthetic redox control over a metal–organic framework as a means to achieving specific desired electronic properties, possibly enabling new applications for these materials in electronic devices.

2.5 Acknowledgements

This work was supported by NSF award number DMR-1309066, with the exception of the magnetic measurements, which were supported by the Nanoporous Materials Genome Center of the U.S. Department of Energy, Office of Basic Energy Sciences, Division of Chemical Sciences, Geosciences and Biosciences under Award Number DE-FG02–12ER16362. We thank NSF for graduate fellowship support of L.E.D. We further thank Dianne J. Xiao for assisting with the Mössbauer spectroscopy experiments, Julia Oktawiec and the 17-BM staff at the Advanced Photon Source for assisting with the powder X-ray diffraction experiments, and Dr. Simon J. Teat for helpful discussions regarding the single-crystal X-ray crystallography data. Powder X-ray diffraction data were collected at Beamline 17-BM at the Advanced Photon Source. The Advanced Photon Source is a U.S. Department of Energy (DoE) Office of Science User Facility operated for the DoE Office of Science by Argonne National Laboratory under Contract No. DE-AC02-06CH11357. Single-crystal X-ray diffraction data were collected at Beamline 11.3.1 at the Advanced Light Source. The Advanced Light Source is supported by the Director, Office of Science, Office of Basic Energy Sciences, of the U.S. Department of Energy under Contract No. DE-AC02-05CH11231.

2.6 References

(1) (a) Furukawa, H.; Go, Y. B.; Ko, N.; Park, Y. K.; Uribe-Romo, F. J.; Kim, J.; O'Keeffe, M.; Yaghi, O. M. *Inorg. Chem.* **2011**, *50*, 9147. (b) Farha, O. K.; Eryazici, I.; Jeong, N. C.; Hauser, B. G.; Wilmer, C. E.; Sarjeant, A. A.; Snurr, R. Q.; Nguyen, S. T.; Yazaydın, A. Ö.; Hupp, J. T. *J. Am. Chem. Soc.* **2012**, *134*, 15016. (c) Furukawa, H.; Cordova, K. E.; O'Keeffe, M.; Yaghi, O. M. *Science*, **2013**, *341*, 1230444.

(2) (a) Eddaoudi, M.; Kim, J.; Rosi, N.; Vodak, D.; Wachter, J.; O'Keeffe, M.; Yaghi, O. M. *Science*. **2002**, *295*, 469. (b) Kreno, L. E.; Leong, K.; Farha, O. K.; Allendorf, M.; Van Duyne, R. P.; Hupp, J. T. *Chem. Rev.* **2012**, *112*, 1105. (c) Sumida, K.; Rogow, D. L.; Mason, J. A.; McDonald, T. M.; Bloch, E. D.; Herm, Z. R.; Bae, T.-H.; Long, J. R. *Chem. Rev.* **2012**, *112*, 724. (d) Zhou, H.-C. J.; Kitagawa, S. *Chem. Soc. Rev.* **2014**, *43*, 5415. (e) Corma, A.; García, H.; Llabrés i Xamena, F. X. *Chem. Rev.* **2010**, *110*, 4606.

(3) Electronics applications: (a) D'Alessandro, D. M.; Kanga, J.; Caddy, J. S. *Aus. J. Chem*. **2011**, *64*, 718. (b) Morozan, A.; Jaouen, F. *Energy Environ. Sci*. **2012**, *5*, 9269. (c) Erickson, K. J.; Léonard, F.; Stavila, V.; Foster, M. E. *Adv. Mater.* **2015**, *27*, 3453.

(4) Magnetism applications: (a) Kurmoo, M. *Chem. Soc. Rev.* **2009**, *38*, 1353. (b) Dechambenoit, P.; Long, J. R. *Chem. Soc. Rev*. **2011**, *40*, 3249. (c) Coronado, E.; Mínguez Espallargas, G. *Chem*. Soc. Rev. **2013**, *41*, 1525.

(5) (a) Givaja, G.; Amo-Ochoa, P.; Gómez-García, C. J.; Zamora, F. *Chem. Soc. Rev*. **2012**, *41*, 115. (b) Takaishi, S.; Hosoda, M.; Kajiwara, T.; Miyasaka, H.; Yamashita, M.; Nakanishi, Y.; Kitagawa, Y.; Yamaguchi, K.; Kobayashi, A.; Kitagawa, H. *Inorg. Chem.* **2009**, *48*, 9048. (c) Kobayashi, Y.; Jacobs, B.; Allendorf, M. D.; Long, J. R. *Chem. Mater*. **2010**, *22*, 4120. (d) Gándara, F.; Uribe-Romo, F. J.; Britt, D. K.; Furukawa, H.; Lei, L.; Cheng, R.; Duan, X.; O'Keeffe, M.; Yaghi, O. M. *Chem. Eur. J*. **2012**, *18*, 10595. (e) Narayan, T. C.; Miyakai, T.; Seki, S.; Dincă, M. *J. Am. Chem. Soc.* **2012**, *134*, 12932. (f) Sun, L.; Miyakai, T.; Seki, S.; Dincă, M. *J. Am. Chem. Soc.* **2013**, *135*, 8185. (g) Talin, A. A.; Centrone, A.; Ford, A. C.; Foster, M. E.; Stavila, V.; Haney, P.; Kinney, R. A.; Szalai, V.; Gabaly, El, F.; Yoon, H. P.; Léonard, F.; Allendorf, M. D. *Science* **2014**, *343*, 66.

(h) Sun, L.; Hendon, C. H.; Minier, M. A.; Walsh, A.; Dincă, M. *J. Am. Chem. Soc.* **2015**, *137*, 6164. (i) Park, S. S.; Hontz, E. R.; Sun, L.; Hendon, C. H.; Walsh, A.; Van Voorhis, T.; Dincă, M. *J. Am. Chem. Soc.* **2015**, *137*, 1774.

(6) (a) Hmadeh, M.; Lu, Z.; Liu, Z.; Gándara, F.; Furukawa, H.; Wan, S.; Augustyn, V.; Chang, R.; Liao, L.; Zhou, F.; Perre, E.; Ozolins, V.; Suenaga, K.; Duan, X.; Dunn, B.; Yamamto, Y.; Terasaki, O.; Yaghi, O. M. *Chem. Mater*. **2012**, *24*, 3511. (b) Kambe, T.; Sakamoto, R.; Hoshiko, K.; Takada, K.; Miyachi, M.; Ryu, J.-H.; Sasaki, S.; Kim, J.; Nakazato, K.; Takata, M.; Nishihara, H. *J. Am. Chem. Soc*. **2013**, *135*, 2462. (c) Kambe, T.; Sakamoto, R.; Kusamoto, T.; Pal, T.; Fukui, N.; Hoshiko, K.; Shimojima, T.; Wang, Z.; Hirahara, T.; Ishizaka, K.; Hasegawa, S.; Liu, F.; Nishihara, H. *J. Am. Chem*. Soc. **2014**, *136*, 14357. (d) Sheberla, D.; Sun, L.; Blood-Forsythe, M. A.; Er, S.; Wade, C. R.; Brozek, C. K.; Aspuru-Guzik, A.; Dincă, M. *J. Am. Chem. Soc*. **2014**, *136*, 8859. (e) Campbell, M. G.; Sheberla, D.; Liu, S. F.; Swager, T. M.; Dincă, M. *Angew. Chem. Int. Ed*. **2015**, *54*, 4349. (f) Huang, X.; Sheng, P.; Tu, Z.; Zhang, F.; Wang, J.; Geng, H.; Zou, Y.; Di, C.-A.; Yi, Y.; Sun, Y.; Xu, W.; Zhu, D. *Nat. Comm*. **2015**, *6*, 7408.

(7) Hendon, C. H.; Tiana, D.; Walsh, A. *Phys. Chem. Chem. Phys*. **2012**, *14*, 13120.

(8) (a) Kitagawa, S.; Kawata, S. *Coord. Chem. Rev*. ***2002***, *224*, 11. (b) Guo, D.; McCusker, J. K. *Inorg. Chem.* **2007**, *46,* 3257.

(9) (a) Pierpont, C. G.; Francesconi, L. C. *Inorg. Chem.* **1977**, *16*, 2367. (b) Dei, A.; Gatteschi, D.; Pardi, L.; Russo, U. *Inorg. Chem*. **1991**, *30*, 2589. (c) Ward, M. D. *Inorg. Chem.* **1996**, *35*, 1712. (d) Min, K. S.; Rheingold, A. L.; DiPasquale, A.; Miller, J. S. *Inorg. Chem*. **2006**, *45*, 6135. (e) Min, K. S.; DiPasquale, A. G.; Golen, J. A.; Rheingold, A. L.; Miller, J. S. *J. Am. Chem. Soc.* **2007**, *129*, 2360. (f) Min, K. S.; Swierczek, K.; DiPasquale, A. G.; Rheingold, A. L.; Reiff, W. M.; Arif, A. M.; Miller, J. S. *Chem. Commun*. **2008**, 317. (g) Min, K. S.; DiPasquale, A. G.; Rheingold, A. L.; White, H. S.; Miller, J. S. *J. Am. Chem. Soc*. **2009**, *131*, 6229.

(10) Das, H. S.; Weisser, F.; Schweinfurth, D.; Su, C. Y.; Bogani, L.; Fiedler, J.; Sarkar, B. *Chem. Eur. J.* **2010**, *16*, 2977.

(11) Abrahams, B. F.; Hudson, T. A.; McCormick, L. J.; Robson, R. *Cryst. Growth Des.* **2011**, *11*, 2717.

(12) Benmansour, S.; Vallés-García, C.; Gómez-Claramunt, P.; Mínguez Espallargas, G.; Gómez-García, C. J. *Inorg. Chem*. **2015**, *54*, 5410.

(13) (a) Luo, T.-T.; Liu, Y.-H.; Tsai, H.-L.; Su, C.-C.; Ueng, C.-H.; Lu, K.-L. *Eur. J. Inor. Chem.* **2004**, 4253. (b) Atzori, M.; Benmansour, S.; Mínguez Espallargas, G.; Clemente-León, M.; Abhervé, A.; Gómez-Claramunt, P.; Coronado, E.; Artizzu, F.; Sessini, E.; Deplano, P.; Serpe, A.; Mercuri, M. L.; Gómez-García, C. J. *Inorg. Chem*. **2013**, *52*, 10031.

(14) (a) Wrobleski, J. T.; Brown, D. B. *Inorg. Chem*. **1979**, *18*, 498. (b) Wrobleski, J. T.; Brown, D. B. *Inorg. Chem*. **1979**, *18*, 2738. (c) Kawata, S.; Kitagawa, S.; Kumagai, H.; Ishiyama, T.; Honda, K.; Tobita, H.; Adachi, K.; Katada, M. *Chem. Mater*. **1998**, *10,* 3902.

(15) (a) Tamaki, H.; Zhong, Z. J.; Matsumoto, N.; Kida, S. *J. Am. Chem. Soc.* **1992**, *114*, 6974. (b) Decurtins, S.; Schmalle, H. W.; Schneuwly, P. *J. Am. Chem. Soc.* **1994**, *116*, 9521. (c) Coronado, E.; Galan-Mascaros, J. R.; Gómez-García, C. J.; Martínez-Ferrero, E.; Almeida, M.; Waerenborgh, J. C. *Eur. J. Inorg. Chem*. **2005**, 2064. (d) Clemente-León, M.; Coronado, E.; Gómez-García, C. J.; Soriano-Portillo, A. *Inorg. Chem*. **2006**, *45*, 5653.

(16) Baum, A. E.; Lindeman, S. V.; Fiedler, A. T. *Chem Commun*. **2013**, *49*, 6531.

(17) Buchanan, R. M.; Kessel, S. L.; Downs, H. H. *J. Am. Chem. Soc.* **1978**, *100*, 7894.

(18) (a) Férey, G.; Millange, F.; Morcrette, M.; Serre, C.; Doublet, M.-L.; Grenèche, J.-M.; Tarascon, J.-M. *Angew. Chem. Int. Ed*. **2007**, *46*, 3259. (b) Fateeva, A.; Horcajada, P.; Devic, T.;

Serre, C.; Marrot, J.; Grenèche, J.-M.; Morcrette, M.; Tarascon, J.-M.; Maurin, G.; Férey, G. *Eur. J. Inorg. Chem*. **2010**, *24*, 3789. (c) Zhang, Z.; Yoshikawa, H.; Awaga, K. *J Am. Chem. Soc*. **2014**, *136*, 16112. (d) Shin, J.; Kim, M.; Cirera, J.; Chen, S.; Halder, G. J.; Yersak, T. A.; Paesani, F.; Cohen, S. M.; Meng, Y. S. *J. Mater. Chem. A* **2015**, *3*, 4738.

(19) Shaikh, N.; Goswami, S.; Panja, A.; Wang, X.-Y.; Gao, S.; Butcher, R. J.; Banerjee, P. *Inorg. Chem*. **2004**, *43*, 5908.

(20) (a) Demadis, K. D.; Hartshorn, C. M.; Meyer, T. J. *Chem. Rev*. **2001**, *101*, 2655. (b) D'Alessandro, D. M.; Keene, F. R. *Chem. Rev.* **2006**, *106*, 2270. (c) D'Alessandro, D. M.; Keene, F. R. *Chem. Soc. Rev*. **2006**, *35*, 424. (d) Hankache, J.; Wenger, O. S. *Chem. Rev.* **2011**, *111*, 5138.

(21) Meilikhov, M.; Yusenko, K.; Torrisi, A.; Jee, B.; Mellot-Draznieks, C.; Pöppl, A.; Fischer, R. A. *Angew. Chem. Int. Ed*. **2010**, *49*, 6212.

(22) (a) Abrahams, B. F.; Bond, A. M.; Le, T. H.; McCormick, L. J.; Nafady, A.; Robson, R.; Vo, N. *Chem. Commun*. **2012**, *48*, 11422. (b) Kung, C.-W.; Wang, T. C.; Mondloch, J. E.; Fairen-Jimenez, D.; Gardner, D. M.; Bury, W.; Klingsporn, J. M.; Barnes, J. C.; Van Duyne, R.; Stoddart, J. F.; Wasielewski, M. R.; Farha, O. K.; Hupp, J. T. *Chem. Mater*. **2013**, *25*, 5012. (c) Wade, C. R.; Li, M.; Dincă, M. *Angew. Chem. Int. Ed.* **2013**, *52*, 13377. (d) Cozzolino, A. F.; Brozek, C. K.; Palmer, R. D.; Yano, J.; Li, M.; Dincă, M. *J. Am. Chem. Soc*. **2014**, *136*, 3334. (e) Leong, C. F.; Chan, B.; Faust, T. B.; D'Alessandro, D. M. *Chem. Sci.* **2014**, *5*, 4724.

(23) Miller, J. S. *Chem. Soc. Rev*. **2011**, *40*, 3266.

(24) Manriquez, J. M.; Yee, G. T.; McLean, R. S.; Epstein, A. J. *Science* **1991**, *152*, 1415.

(25) Miyazaki, A.; Yamazaki, H.; Aimatsu, M.; Enoki, T.; Watanabe, R.; Ogura, E.; Kuwatani, Y.; Iyoda, M. *Inorg. Chem*. **2007**, *46*, 3353.

(26) Clérac, R.; O'Kane, S.; Cowen, J.; Ouyang, X.; Heintz, R.; Zhao, H.; Bazile, M. J.; Dunbar, K. R. *Chem. Mater*. **2003**, *15*, 1840.

(27) Mathonière, C.; Nuttall, C. J.; Carling, S. G.; Day, P. *Inorg. Chem*. **1996**, *35*, 1201.

(28) Verdaguer, M.; Bleuzen, A.; Marvaud, V. *Coord. Chem. Rev.* **1999**, *190*, 1023.

(29) Zhu, Z.; Li, H.; Liang, J.; Tao, Z.; Chen, J. *Chem. Commun*. **2014**, *51*, 1446.

(30) Düren, T.; Millange, F.; Férey, G.; Walton, K. S.; Snurr, R. Q. *J. Phys. Chem C* **2007**, *111*, 15350.

(31) Note: Surface area was calculated using the crystallographic data obtained for **1** (Table S2.1) and a crystal density that was calculated by excluding the tetrabutylammonium ions in order to mimic the charge-balanced $Fe^{III}_2(dhbq^{2-})_3$ framework (ρ_{calcd} = 0.644 mg/m^3).

(32) Coronado, E.; Day, P. *Chem Rev.* **2004**, *104*, 5419.

Chapter 2 Supporting Information

S2.1 Experimental Details

Synthesis of $Na_{3.2}(NBu_4)_{1.8}Fe^{III}_2(dhbq)_3$. Prior to chemical reduction, cubic crystals of **1** were ground into a microcrystalline powder using a mortar and pestle inside an Ar-atmosphere glovebox. Then, a suspension of 53.3 mg (0.053 mmol) of **1** in 3.0 mL of THF was prepared. Na-naphthalenide was prepared by stirring 27.0 mg (0.211 mmol) of naphthalene ($C_{10}H_8$) over a roughly 10-fold excess of sodium metal in 2.0 mL of THF for 3 h. The resulting solution was filtered and added drop-wise to the stirred suspension of **1** in THF at room temperature. The mixture was stirred for 12 h, after which $Na_{3.2}(NBu_4)_{1.8}Fe^{III}_2(dhbq)_3$ was recovered as a dark brown microcrystalline powder by vacuum filtration, washed with 2 x 2.0 mL THF, and dried for 1 h under reduced pressure. ICP analysis indicated that 3.2 molar equivalents of Na^+ ions were introduced per mole of **1**. Unfortunately, C, H, and N elemental analysis was unsuccessful for $Na_{3.2}(NBu_4)_{1.8}Fe^{III}_2(dhbq)_3$, resulting in unrealistically low percentages of C, H, and N. While originally we believed that this result could indicate that much higher levels of cation exchange had occurred than previously observed for framework **2**, the obvious crystallinity and lack of unit cell change for $Na_{3.2}(NBu_4)_{1.8}Fe^{III}_2(dhbq)_3$ (Figure S2.4) to us was indicative that no significant increase in cation exchange had taken place. Thus, the level of cation exchange in $Na_{3.2}(NBu_4)_{1.8}Fe^{III}_2(dhbq)_3$ was assumed to be the same as for **2** (10% exchange of NBu_4^+ for Na^+) due to the similar conditions of the reduction. This resulted in a chemical formula assignment of $Na_{3.2}(NBu_4)_{1.8}Fe^{III}_2(dhbq)_3$, which corresponds to 3.0 electrons introduced per mole of framework **1**. Notably, during the synthesis of **2**, 0.7 moles of electrons were introduced into framework **1** per mole of the reducing agent sodium naphthalenide added. In the case of $Na_{3.2}(NBu_4)_{1.8}Fe^{III}_2(dhbq)_3$, 0.75 moles of electrons were introduced into the framework per mole of sodium naphthalenide added. Considering this similarity in addition to the other characterization performed (ICP analysis, powder x-ray diffraction, IR spectroscopy, Mössbauer spectroscopy), we believe that the postulated chemical formula $Na_{3.2}(NBu_4)_{1.8}Fe^{III}_2(dhbq)_3$ is a reasonable one. ICP Found: Fe:Na, 0.63(1):1. IR (solid-ATR): 2955 (w), 2931 (w), 2861 (w), 1498 (s), 1469 (s), 1379 (s), 1292 (m), 1270 (m), 1248 (s), 1209 (s), 1150 (s), 1029 (m), 878 (m), 864 (s), 834 (m), 810 (s), 755 (m).

Procedure for Metal Content Analysis via ICP-OES. About 15 mg of sample were placed in a 20 mL glass vial and digested with 5 mL 5% HNO_3 in Millipore water at 80 °C. This solution was then diluted with 15 mL 5% HNO_3 in Millipore water. Standard solutions ranging from 1 to 32 ppm of Fe and Na were prepared for the calibration curve.

Single Crystal X-Ray Diffraction. X-ray diffraction analyses were performed on single crystals coated with Paratone-N oil and mounted on MiTeGen loops. Crystals were frozen at a temperature of 100 K by an Oxford Cryosystems Cyrostream 800 Plus using N_2 during the experiment. Data was collected at Beamline 11.3.1 at the Advanced Light Source, Lawrence Berkeley National Laboratory using synchrotron radiation (λ = 0.8856 Å) and a Bruker PHOTON100 CMOS diffractometer. Raw data were integrated and corrected for Lorentz and polarization effects using Bruker AXS SAINT software.[2] Absorption corrections were applied using SADABS.[3] The structure was solved using direct methods with SHELXS[4,5] and refined using SHELXL[6] operated in the OLEX2[7] interface. Thermal parameters were refined anisotropically for all non-hydrogen atoms. Hydrogen atoms were placed in ideal position and refined using a riding model. Refinement

of the crystal of **1** resulted in a Flack parameter of 0.507(8). Thus, it was refined as a 2-component inversion twin, resulting in a lower R1 and wR2. The tetrabutylammonium countercation required distance and extended rigid bond restraints, due to its severe disorder over three positions on a three-fold axis in the structure.

Powder X-Ray Diffraction. Microcrystalline samples of **1** and **2** were loaded into 1.0 mm boron-rich glass capillaries inside an Ar atmosphere glovebox, and then the capillaries were flame-sealed. High-resolution x-ray powder diffraction data were subsequently collected at beamline 17-BM at the Advanced Photon Source (APS) at Argonne National Laboratory. Diffraction patterns were collected at 100 K with a wavelength of 0.72768 Å.

NIR-UV-Visible Spectroscopy. UV-visible-NIR diffuse reflectance spectra were collected using a CARY 5000 spectrophotometer interfaced with Varian Win UV software. The samples were held in a Praying Mantis air-free diffuse reflectance cell. Polyvinylidene fluoride (PVDF) powder was used as a non-adsorbing matrix. The Kubelka-Munk conversion (F(R) vs. wavenumber) of the raw diffuse reflectance spectrum (R vs. wavenumber) was obtained by applying the formula $F(R) = (1 - R)^2/2R$.

Mössbauer Spectroscopy. Iron-57 Mössbauer spectra were obtained at 100 K with a constant acceleration spectrometer and a cobalt-57 rhodium source. Prior to measurements the spectrometer was calibrated at 290 K with α-iron foil. The isomer shifts are relative to room temperature α-iron foil. Samples were prepared inside an Ar atmosphere glovebox and contained roughly 25 mg/cm^2 of sample (2.8 mg/cm^2 of iron) diluted with boron nitride. All spectra were fit with symmetric Lorentzian quadrupole doublets using the WMOSS Mössbauer Spectral Analysis Software.[1]

Variable Temperature Two-Point Electronic Conductivity. Variable temperature conductivity was conducted in a home built 2-electrode screw cell (Scheme S2.1) with a contact area of 0.04757 cm^2. In an argon-filled glove box, pellets of the materials studied were pressed between two copper rods with contacts polished to a mirror finish. Sample thicknesses were measured with a caliper and were typically in the range of 300 to 700 μm; thicker pellets were used for **1** to accommodate the larger crystallite size. The screw cell was sealed with Torr Seal ® low vapor pressure epoxy to make an airtight seal.

Conductivity measurements were performed in a Quantum Design MPMS2 SQUID magnetometer with a standard sample rod modified to accommodate two 26 AWG silver coated copper cables sealed at the top of the rod with a air tight Swagelok fitting and Torr Seal ® low vapor pressure epoxy. The sample cell was attached to the SQUID sample rod and descended into the cryostat-equipped SQUID chamber. I-V profiles were collected with a Bio-Logic SP200 potentiostat with 30 nA current resolution. All data collected was Ohmic within a ±1 V window with a very small apparent temperature hysteresis that vanished after thermal cycling and equilibration at 300 K.

The resulting I-V profiles were modeled with Ohm's law, $E \cdot \sigma = I$, where E is the applied field and I is the current density, to determine the sample conductivity, σ, with units of Ω^{-1} cm^{-1}. The temperature dependence of conductivity was fit the to the Arrhenius equation, $\sigma = \sigma_0^{-\frac{E_A}{k_B T}}$, where σ is the conductivity, σ_0 is the pre-exponential factor, E_A is the Arrhenius activation energy, k_B is the Boltzmann constant, and T is the temperature.

Electrochemical Methods. Materials were characterized electrochemically in an argon-filled glovebox. A custom build air tight three-electrode cell was constructed using a 1/2 inch diameter Swagelok PFA union tee and Ti current collectors machined to fit snugly. Lithium metal was smeared onto the counter and reference electrodes and polished to a mirror finish. Electrodes were prepared by drop casting a slurry of 60 wt% sample, 30 wt% conductive carbon Super P (Alfa Aesar), and 10 wt% PVDF (Sigma Aldrich) and electrolyte soaked quartz fiber was used as the separator. Slow-scan cyclic voltammograms were collected at 30 μV/s using a Bio-Logic VMP-3 multipotentiostat fitted to an argon glovebox. Data were analyzed with the free software package EC-Lab v10.41 offered by Bio-Logic.

Magnetic Measurements. Samples were prepared by adding crystalline powder of **1** (50.0 mg) and **2** (20.5 mg) to a 5 mm inner diameter quartz tube containing a raised quartz platform. Solid eicosane was added to cover the sample to prevent crystallite torqueing and provide good thermal contact between the sample and the cryostat. The tubes were fitted with Teflon sealable adapters, evacuated on a Schlenk line, and flame-sealed under static vacuum. Following flame sealing, the solid eicosane was melted in a water bath held at 40 °C. Magnetic susceptibility measurements were performed using a Quantum Design MPMS2 SQUID magnetometer. Dc magnetic susceptibility measurements were collected in the temperature range 2-300 K under applied magnetic fields of 0.1 T, 0.5 T, and 1 T. Magnetic hysteresis measurements were performed at a sweep rate of 2 mT/s. Diamagnetic corrections were applied to the data using Pascal's constants to give $\chi_D = -0.00060348$ emu/mol (**1**), $\chi_D = -0.00056417$ emu/mol (**2**), and $\chi_D = -0.00024306$ emu/mol (eicosane).

Table S2.1. Crystal data and structure refinement for $(NBu_4)_2Fe^{III}_2(dhbq)_3$ (**1**).

Empirical formula	$C_{50}H_{78}Fe_2N_2O_{12}$
Formula weight	1010.84
Temperature	100(2) K
Wavelength	0.8856 Å
Crystal system	Cubic
Space group	I-43d
a (Å)	22.1401(5)
b (Å)	22.1401(5)
c (Å)	22.1401(5)
α (°)	90
B (°)	90
γ (°)	90
Volume ($Å^3$)	10852.7(7)
Z	8
P_{calcd} (mg/m^3)	1.237
μ (mm^{-1})	1.061
F(000)	4320
Crystal size	0.05 x 0.05 x 0.05 mm^3
Theta range (°)	2.808–30.185
Reflections	46510
Independent reflections	1397 [R(int) = 0.0640]
Completeness to theta = 30.185°	100.0 %
Absorption correction	Semi-empirical from equivalents
Max. and min. transmission	0.979 and 0.857
Refinement method	Full-matrix least-squares on F^2
Data / restraints / parameters	1397 / 118 / 203
Goodness-of-fit on F^2	1.168
Final R indices [I>2σ(I)]	R1 = 0.0733, wR2 = 0.1966
R indices (all data)	R1 = 0.0834, wR2 = 0.2064
Largest diff. peak and hole (e./$Å^3$)	0.344 and –0.527

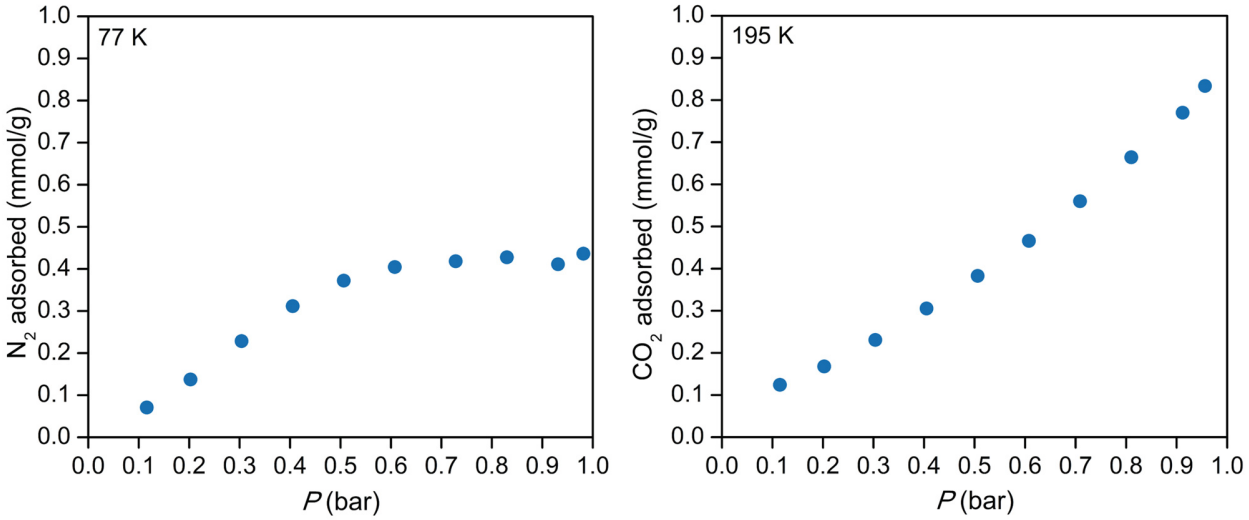

Figure S2.1. 77-K N_2 (left) and 195-K CO_2 (right) adsorption isotherms for **1** confirming nonexistent microporosity. Adsorption isotherms were performed after heating solid samples of **1** under vacuum at 150 °C for 1 h.

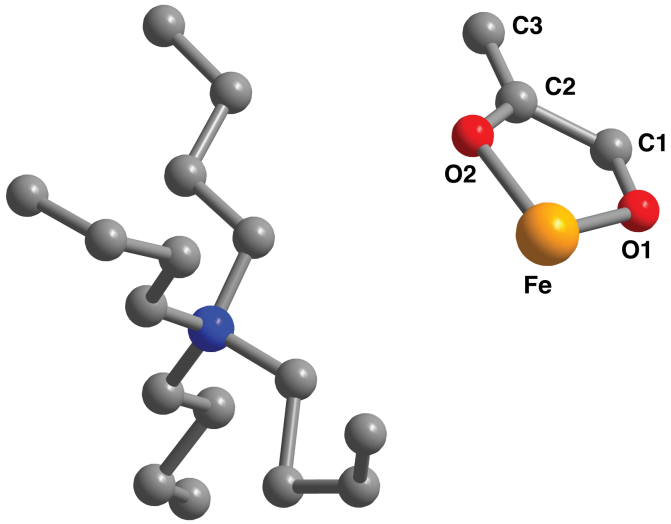

Fe-O1 (Å)	2.005(7)
Fe-O2 (Å)	2.030(7)
O1-C1 (Å)	1.278(13)
O2-C2 (Å)	1.312(14)
C1-C2 (Å)	1.521(12)
C2-C3 (Å)	1.324(16)

Figure S2.2. Asymmetric unit of the single crystal x-ray diffraction structure of **1** with selected bond distances shown.

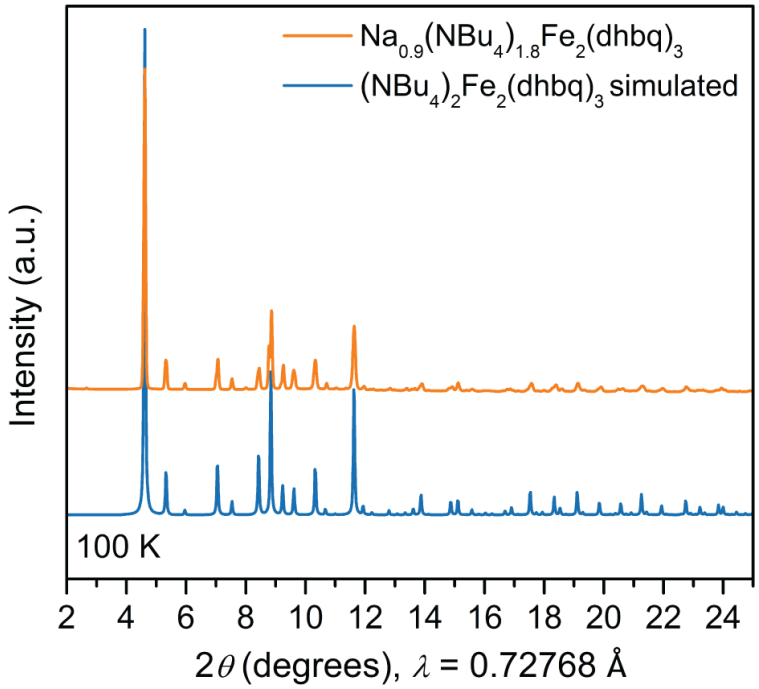

Figure S2.3. Simulated x-ray powder diffraction pattern for **1** and x-ray powder diffraction pattern for **2** at 100 K.

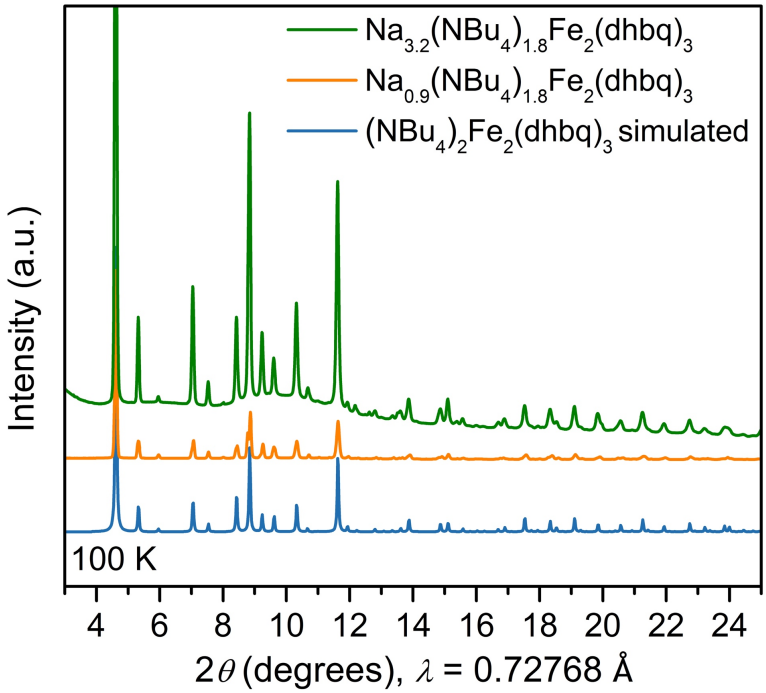

Figure S2.4. Simulated x-ray powder diffraction pattern for **1** and x-ray powder diffraction patterns for **2** and $Na_{3.2}(NBu_4)_{1.8}Fe^{III}_2(dhbq)_3$ at 100 K, shown by blue, orange, and green lines, respectively.

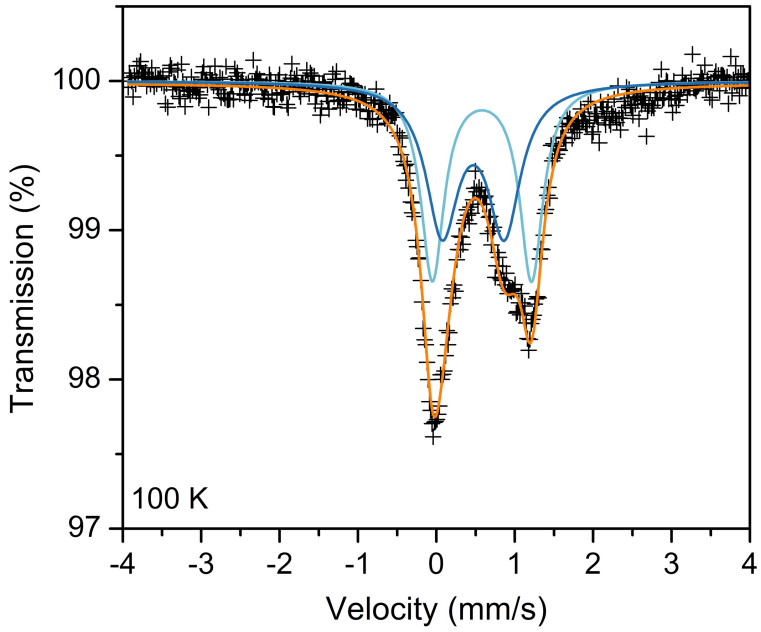

Figure S2.5. ^{57}Fe Mössbauer spectrum for $Na_{3.2}(NBu_4)_{1.8}Fe^{III}_2(dhbq)_3$ at 100 K with the fit to the spectrum shown in orange. The fit has parameters consistent with two different high-spin Fe^{III} centers (dark blue: Area = 51(1)%, δ = 0.47(3) mm s^{-1}, $|\Delta E_Q|$ = 0.79(2) mm s^{-1}, Γ = 0.50(5) mm s^{-1}; pale blue: Area = 49(1)%, δ = 0.58(1) mm s^{-1}, $|\Delta E_Q|$=1.26(3) mm s^{-1}, Γ = 0.36(2) mm s^{-1}).

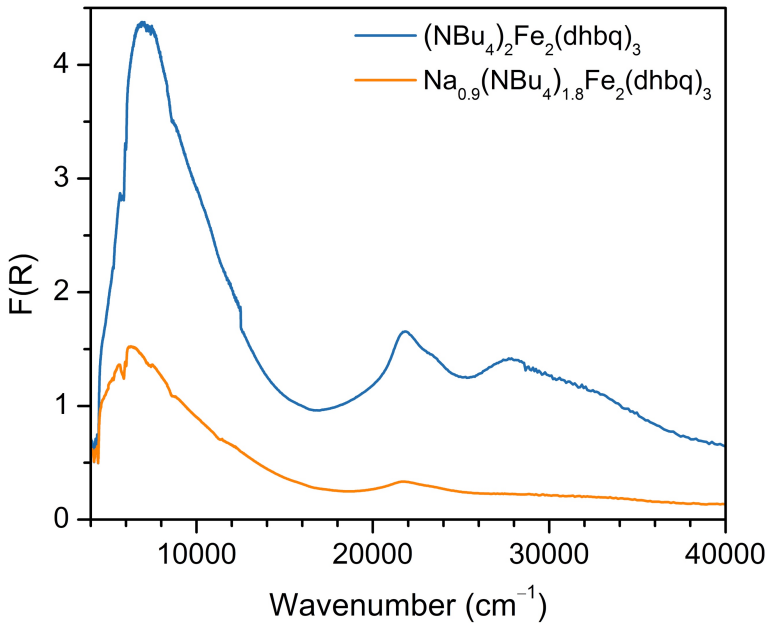

Figure S2.6. Full UV-Vis-NIR diffuse reflectance spectra for **1** and **2**. F(R) is a Kubelka-Munk conversion of the raw diffuse reflectance spectrum.

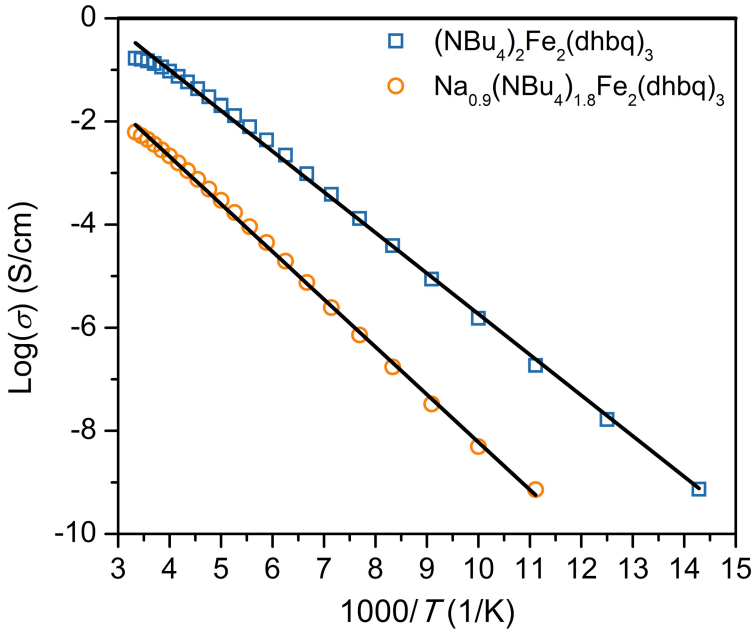

Figure S2.7. Variable-temperature conductivity data for **1** and **2** shown by blue squares and orange circles, respectively. Arrhenius fits to the data are shown by black lines.

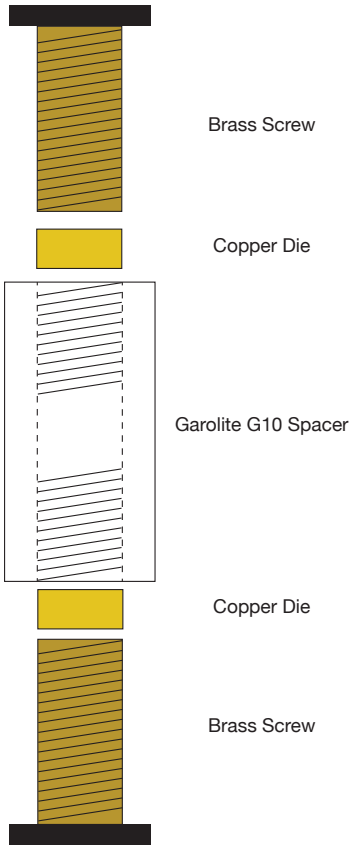

Scheme S2.1. Schematic of the cell used for variable-temperature conductivity. Outer diameter of the cell is 7 mm.

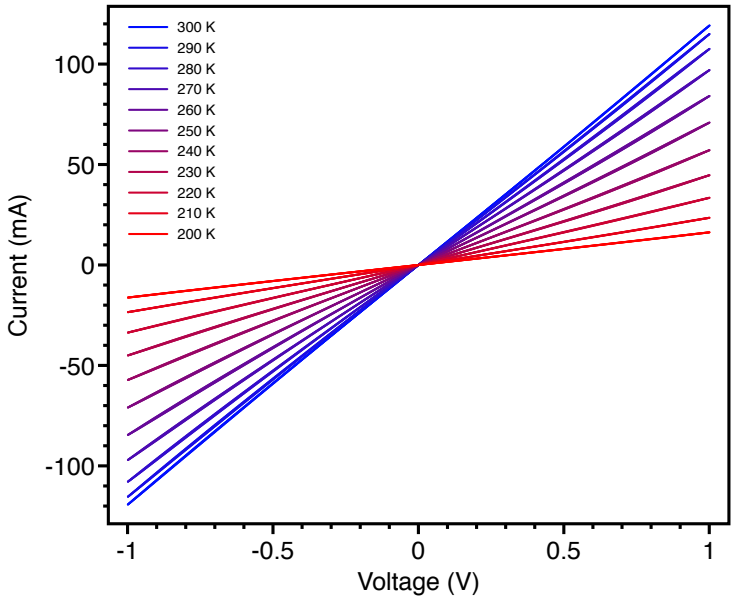

Figure S2.8: I-V curves collected on **1** from 300 K to 200 K display Ohmic response between +1 and –1 V. Similar linearity was observed down to 60 K for this sample.

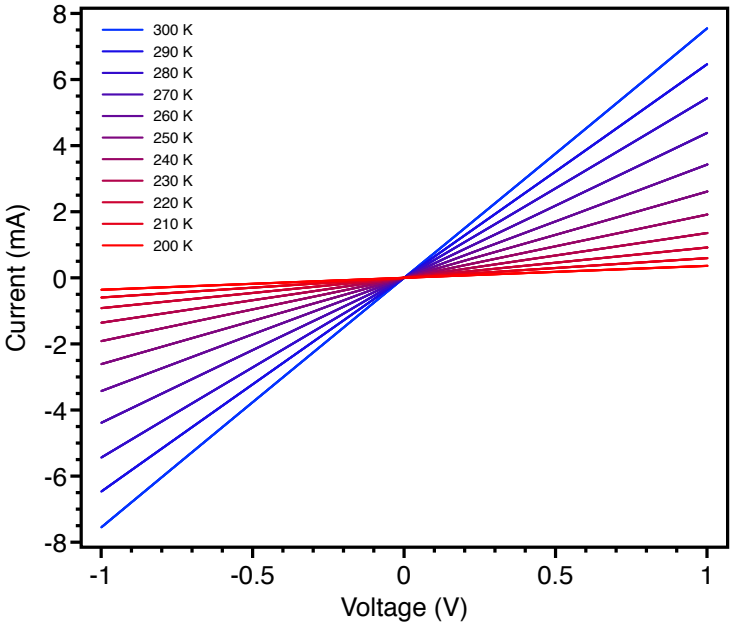

Figure S2.9: I-V curves collected on **2** from 300 K to 200 K display Ohmic response between +1 and –1 V. Similar linearity was observed down to 90 K for this sample.

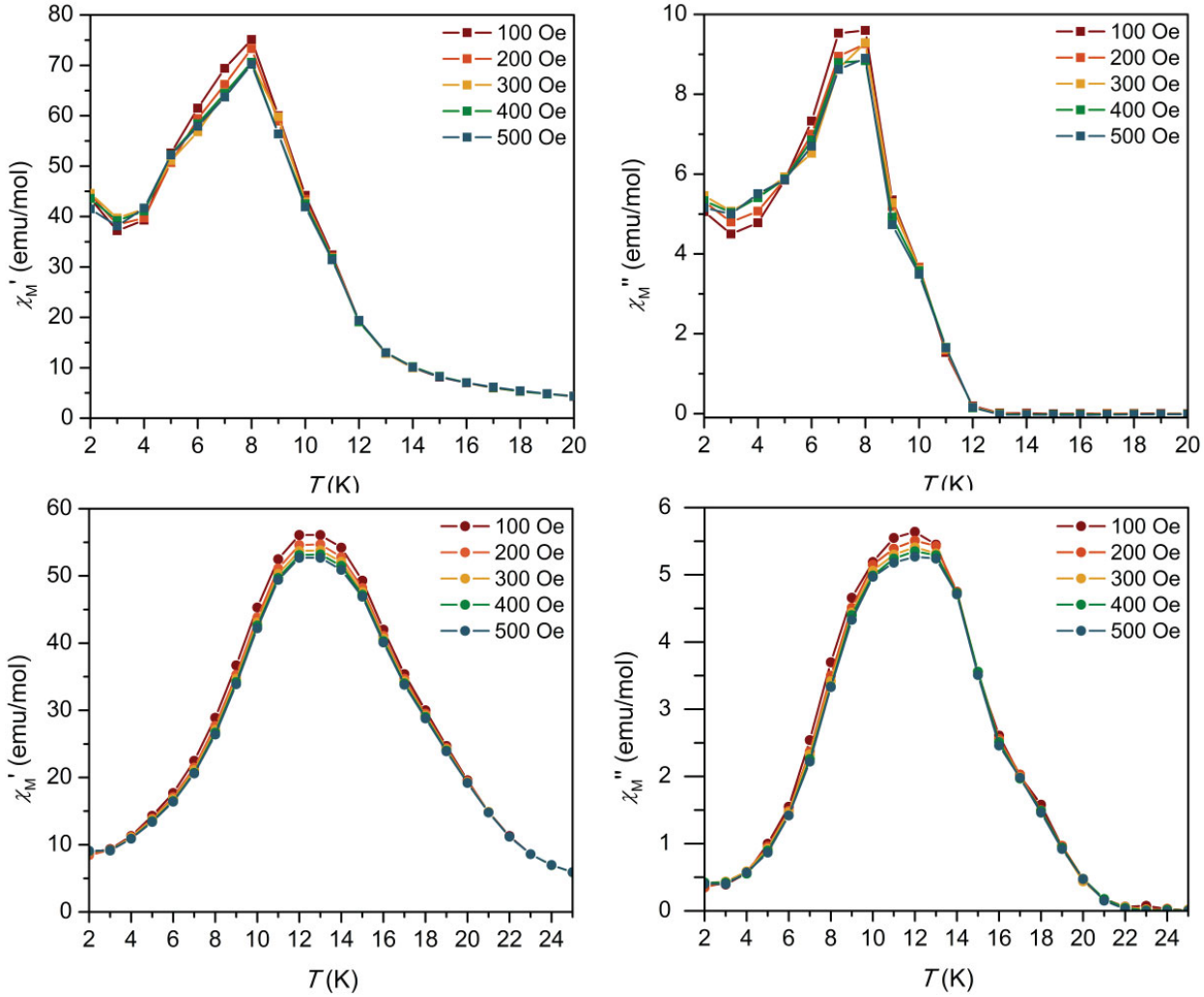

Figure S2.10. Variable-temperature ac magnetic susceptibility data at zero dc magnetic field and in a 4 Oe ac oscillating magnetic field for **1** (top, circles) and **2** (bottom, squares). Data under frequencies of 100 Oe, 200 Oe, 300 Oe, 400 Oe, and 500 Oe is shown by red, orange, yellow, green, and blue symbols, respectively. Lines are to guide the eye.

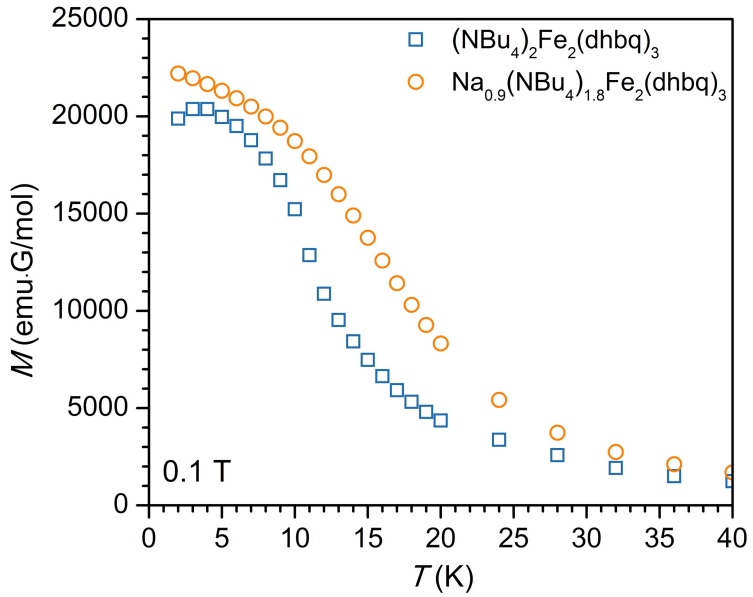

Figure S2.11. Variable-temperature magnetization data for **1** and **2** at low temperature. The gradual increase in magnetization and lack of obvious magnetization saturation below the magnetic ordering temperature is indicative of ferrimagnetic ordering.

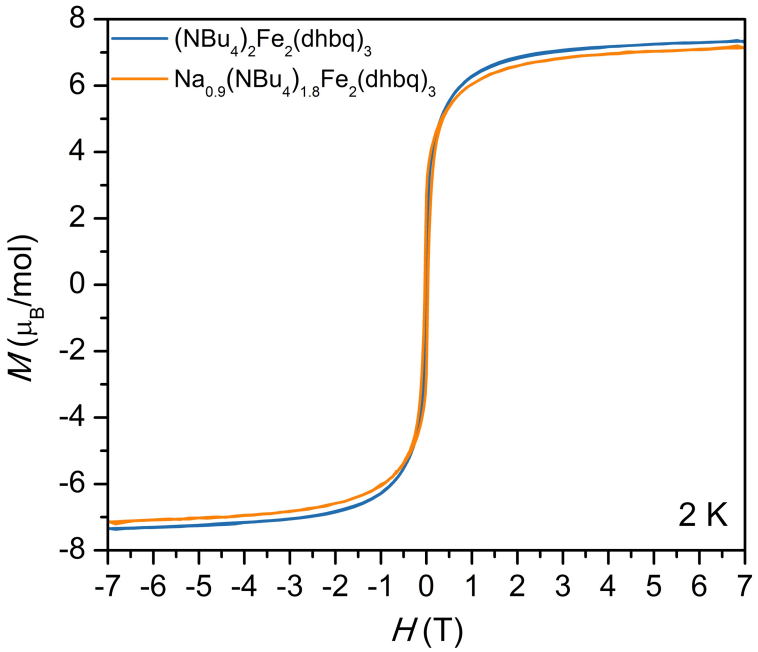

Figure S2.12. Magnetization (*M*) versus applied dc magnetic field data (*H*) for **1** and **2** in blue and orange, respectively. Hysteresis loops were recorded at a sweep rate of 2 mT/s.

S2.2 References for Chapter 2 Supporting Information

(1) Ion Prisecaru, WMOSS4 Mössbauer Spectral Analysis Software, www.wmoss.org, 2009-2013.
(2) SAINT and APEX 2 Software for CCD Diffractometers, Bruker Analytical X-ray Systems Inc., Madison, WI, USA, 2014.
(3) Sheldrick, G. M. SADABS, Bruker Analytical X-ray Systems Inc., Madison, WI, USA, 2014.
(4) Sheldrick, G. M. SHELXS, University of Göttingen, Germany, 2014.
(5) Sheldrick, G. M. *Acta Crystallogr., A, Found. Crystallogr*. **2008**, *64*, 112.
(6) Sheldrick, G. M. SHELXL, University of Göttingen, Germany, 2014.
(7) Dolomanov, O. V.; Bourhis, L. J.; Gildea, R. J.; Howard, J. A. K.; Puschmann, H. *J. Appl. Cryst.* **2009**, *42*, 339.

Chapter 3: Magnetic Exchange in Two-Dimensional Lanthanide-Semiquinoid Frameworks

3.1 Introduction

The lanthanide ions have been an enduring component of high-performance magnetic materials for the last century due to their unquenched orbital angular momentum, leading to intrinsic magnetic anisotropy, along with, for the later lanthanide ions, large magnetic moments. Many of the technological gains of the 20th century, including portable electronics, data recording media, and electric motors and generators were enabled by the discovery and optimization of lanthanide-based permanent magnets.[1] Magnetic materials such as $Nd_2Fe_{14}B$[2,3] and $SmCo_5$[4] utilize the intrinsic anisotropy of the lanthanide ions, along with exchange coupling with itinerant 3d electrons, to yield high-ordering-temperature magnets with both large magnetic anisotropy and large saturation magnetization.

In contrast to these dense intermetallic solids, metal–organic frameworks, a comparatively new class of solids consisting of metal ion or cluster units bridged by organic linkers, have utilized modularity of metal, linker, and framework topology to produce an enormous range of low-density, porous materials with applications in gas storage, separations, sensing, and catalysis.[5,6] Development of metal–organic magnets with characteristics mirroring those of their solid-state counterparts, namely high-temperature magnetic ordering and large coercive fields, is intrinsically challenging due to the low-density nature of metal–organic systems. Magnetic ordering temperature in particular is known to be proportional to the number of magnetic neighbors and the strength of their magnetic exchange,[7] the latter of which is limited by the long distances between paramagnetic metal centers in metal–organic frameworks, often greater than 10 Å. As such, strategies to enhance magnetic exchange, and thereby magnetic ordering temperature, in metal–organic frameworks are critical to their use in magnetic applications, including magnetic shielding,[8] magnetically-responsive guest sensing,[9,10] and even simply as bulk magnets.[11,12]

Conveniently, use of paramagnetic radical bridging ligands as the linker in extended solids concomitantly increases the number of magnetic neighbors and the strength of magnetic exchange— metals participate in direct exchange with the spin-carrying ligand orbitals, rather than in superexchange interactions across a diamagnetic linker. Combinations of transition metals and radical ligands have already yielded a number of high-performance magnetic materials, including the room-temperature magnet $V(TCNE)_2 \cdot yCH_2Cl_2$ (TCNE = tetracyanoethylene).[13] In contrast, only a few lanthanide-radical frameworks have been investigated thus far, and are mainly based on the TCNE ligand and the related linker 7,7,8,8-tetracyanoquinodimethane (TCNQ).[14-17] Recent work has revealed that the paramagnetic trianion of the redox-active ligand 2,5-dihydroxy-1,4-benzoquinone linker (Figure 3.1) can be incorporated into extended two- and three-dimensional frameworks to provoke strong magnetic exchange and electronic conductivity.[18-23] However, thus far $dhbq^{3-}$ radical ligands have been incorporated into extended solids primarily via combination of sufficiently reducing metal ions, such as Fe^{II}, with the $dhbq^{2-}$ ligand to prompt a metal-to-ligand electron transfer during framework synthesis. Considering the majority of lanthanide chemistry, excepting that performed in extremely reducing conditions, utilizes trivalent, redox-inert lanthanide ions, methods such as post-synthetic chemical redox reactions must be pursued in order to incorporate $dhbq^{3-}$ linkers into extended solids of the lanthanide ions. Herein, $dhbq^{2-}$-bridged two-dimensional lanthanide frameworks, $Ln_2(dhbq)_3(DMF)_x \cdot y$DMF (**1-Ln**, Ln = Y, Sm–Yb), are synthesized and post-synthetically reduced to produce, in the cases of Ln = Y, Tb–Yb, their $dhbq^{3-}$-bridged congeners (**2-Ln**). These radical-bridged lanthanide frameworks are characterized spectroscopically and magnetically, revealing, in some variants, low-temperature metamagnetic behavior and glassy magnetic ordering.

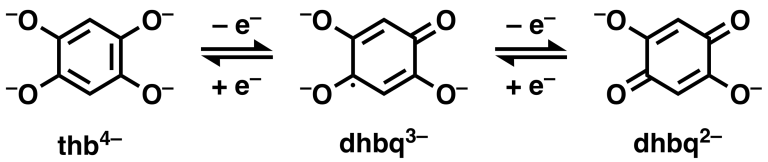

Figure 3.1. Redox states of 2,5-dihydroxy-1,4-benzoquinone that have previously been isolated in metal–organic molecules or coordination solids.

3.2 Experimental Information

General Information. The compounds 2,5-dihydroxy-1,4-benzoquinone (H_2dhbq) (98%), $Sm(NO_3)_3{\cdot}6H_2O$ (99.999%), $Eu(NO_3)_3{\cdot}H_2O$ (99.99%), $Dy(NO_3)_3{\cdot}6H_2O$ (99.9%), $Tm(NO_3)_3{\cdot}5H_2O$ (99.9%), naphthalene (99%), and sodium metal (99.9%) were purchased from Sigma Aldrich and used as received. The compound $Yb(NO_3)_3{\cdot}6H_2O$ (99.99%) was purchased from Alfa Aesar and used as received. The salts $Ln(NO_3)_3{\cdot}6H_2O$ (Ln = Gd, Tb; 99.9%) and $Ln(NO_3)_3{\cdot}H_2O$ (Ln = Ho, Er, Y; 99.9%) were purchased from Strem and used as received. For the synthesis of **1-Ln**, *N*,*N*-dimethylformamide (DMF) was purchased from Sigma-Aldrich and used as received. Anhydrous DMF—used in the synthesis of DMF-solvated **1-Ln** and **2-Ln**—was prepared by passage over activated molecular sieves using a JC Meyer solvent system and stored over 4 Å sieves. Tetrahydrofuran (THF) was prepared by passage over activated molecular sieves using a JC Meyer solvent system and stored over 4 Å sieves. The compounds **1-Ln** were prepared under a combination of ambient (in air) and anhydrous conditions. Following the isolation of **1-Ln**, subsequent preparation of **2-Ln** (Ln = Y, Tb–Yb) and all manipulations of **2-Ln** were performed under an Ar atmosphere in a VAC glovebox. Carbon, hydrogen, and nitrogen analyses were obtained from the Microanalytical Laboratory at the University of California, Berkeley.

Synthesis of $Tb_2(dbhq)_3(DMF)_4{\cdot}2DMF$ (1-Tb). A solution of H_2dhbq (260.6 mg, 1.860 mmol) in DMF (4 mL) was layered on top of a solution of $Tb(NO_3)_3{\cdot}6H_2O$ (561.7 mg, 1.240 mmol) in DMF (4 mL) in a 20 mL scintillation vial. The vial was then placed in a steel heating block atop a hot plate set to 60 °C. Dark red solid **1-Tb**, including single crystals, formed after 1 d. Heating was continued for a total of 3 d, upon which the vial was removed from the heating block and allowed to cool. After cooling, crystalline **1-Tb** was isolated by filtration and the product was dried under reduced pressure for 4 h. The **1-Tb** material is quite hydroscopic. Rigorously water-free material was required in the preparation of **2-Tb**, which uses water-reactive sodium naphthalenide as a reducing agent. Accordingly, solid $Tb_2(dbhq)_3(DMF)_6(H_2O)_x$ was brought into an argon-atmosphere VAC glovebox, crushed into a pink powder, and soaked in anhydrous DMF for 12 h. The solid was subsequently isolated by filtration and dried under reduced pressure for 15 min. Elemental analysis indicated that material treated in this manner is fully solvated by DMF, with a formula unit of $Tb_2(dbhq)_3(DMF)_6$, and this solid was subsequently used for preparation of **2-Tb**. Yield: 211.8 mg (14.6%). Anal. Calcd. for $C_{36}H_{48}Tb_2N_6O_{18}$: C, 36.94; H, 4.13; N, 7.18. Found: C, 36.63; H, 3.98; N, 7.10.

The same synthesis and DMF-solvation procedures described above were followed in the preparation of the other **1-Ln** materials (Ln = Y, Sm, Eu, Gd, Dy, Ho, Er, Tm, Yb, see Supporting Information).

Synthesis of $Na_{2.7}Tb_2(dbhq)_3(DMF)_{2.3}(THF)_{0.6}$ (2-Tb). A solution of sodium naphthalenide was prepared by stirring naphthalene (42.8 mg, 0.334 mmol) in THF over ~2-fold excess sodium for 3

h. The dark green sodium naphthalenide solution was then added to a stirring suspension of **1-Tb** (130.3 mg, 0.1110 mmol) in THF (4 mL). This suspension was stirred for 12 h, during which time the suspended solids changed in color from pink-red to green. Solids of **2-Tb** were isolated by filtration, washed with 2 mL of THF, and dried for 15 min. The formula unit was determined by simultaneous fitting of C, H, N, and Na elemental analysis, in which Na content was obtained by inductively coupled plasma (ICP) analysis. Yield: 113 mg (100%). Anal. Calcd. for $C_{27.3}H_{26.9}N_{2.3}Na_{2.7}O_{14.9}Tb_2$ ($Na_{2.7}Tb_2(dbhq)_3(DMF)_{2.3}(THF)_{0.6}$): C, 32.61; H, 2.70; N, 3.20. Found: C, 32.47; H, 3.16; N, 3.09. ICP Calcd: Na, 6.17; Found: Na, 6.13.

The same procedure was followed in the preparation of **2-Ln** (Ln = Y, Dy, Ho, Er, Tm, Yb, see the Supporting Information).

Attempted reduction of 1-Sm, 1-Eu, and 1-Gd. Post-synthetic reduction reactions were attempted using materials **1-Sm**, **1-Eu**, and **1-Gd** in a manner similar to preparation of **2-Tb**. However, the resulting solids were amorphous, and the magnetic data of these solids showed only minimal differences compared to that of their starting materials (see Figure S3.1 for a comparison of magnetic susceptibility data of **1-Gd** and "1-Gd-reduction conditions"). To complicate matters, elemental analysis and ICP data of the resulting solids yielded found molar values of Na close to that found for **2-Tb** and expected for the corresponding **2-Ln** materials, indicating that some reduction, and corresponding incorporation of sodium countercations, did occur. Similarly, IR spectroscopy revealed a shift in the $dhbq^{n-}$ carbonyl stretch of the reduced products, indicating that at least surface reduction of the $dhbq^{2-}$ ligands had occurred (see Figure S3.2 for a comparison of infrared spectra of **1-Gd** and "1-Gd-reduction"). The amorphous nature of the reduction products and negligible change in magnetic behavior likely indicate that the sodium naphthalenide diffused less efficiently into the two-dimensional frameworks **1-Sm**, **1-Eu**, and **1-Gd** compared to the other **1-Ln** materials. The materials **1-Sm**, **1-Eu**, and **1-Gd** conspicuously crystallize in a different structure type compared to the materials **1-Y**, **1-Tb**, **1-Dy**, **1-Ho**, **1-Er**, **1-Tm**, and **1-Yb**, making such a difference in reactivity plausible. A buildup of reducing reagent on the surface of the materials **1-Sm**, **1-Eu**, and **1-Gd** would enable over-reduction of the ligand to the tetraanionic redox state, thb^{4-}. Materials containing this diamagnetic linker would be expected to show magnetic behavior similar to that of the starting material **1-Ln**, and would explain the presence of sodium countercations in the reduced products.

3.3 Results and Discussion

Synthesis and structural characterization of 1-Ln. Two-dimensional frameworks of the general formula $Ln_2(X_2dhbq)_3(solv)_x\cdot(solv)_y$ have been previously characterized—in particular the series $Ln_2(dhbq)_3(H_2O)_x\cdot yH_2O$ (Ln = Y, La, Ce, Gd, Yb, Lu), $Ln_2(Cl_2dhbq)_3(H_2O)_x\cdot yH_2O$ (Ln = Sc, Y, La, Pr, Nd, Gd, Tb, Yb), and $Ln_2(Br_2dhbq)_3(solv)_x\cdot ysolv$ (solv = dimethylsulfoxide or H_2O; Ln = La–Yb).[24-26] However, frameworks of the type $Ln_2(dhbq)_3(DMF)_x\cdot yDMF$ were not previously known. The compounds **1-Ln** were prepared by initially combining 3 equivalents of 1,4-dihydroxy-2,5-benzoquinone (H_2dhbq) with 2 equivalents of $Ln(NO_3)_3\cdot(H_2O)_x$ in *N*,*N*-dimethylformamide (DMF). Each mixture was heated between one and three days at 60 °C to yield dark red crystalline powders and single crystals of $Ln_2(dhbq)_3(DMF)_x\cdot yDMF$ (**1-Ln**), in yields ranging from 7–30%. Longer reaction times (~3 d) were used for the preparation of **1-Sm**, **1-Eu**, **1-Gd**, and **1-Tb**, which formed much more slowly than the other variants. Reaction times longer than 3 days, or reaction temperatures much greater than 60 °C (e.g. 120 °C) resulted in the gradual

production of amorphous brown solids, attributed to thermal decomposition of DMF. Yields of **1-Ln** for lanthanides with larger ionic radii than Eu^{3+} were too low to allow for full characterization.

Single-crystal X-ray characterization of **1-Ln** revealed that the material crystallizes in two different space groups depending on the size of the lanthanide ion. For the larger lanthanides Sm, Eu, and Gd, **1-Ln** crystallizes in the space group *C2/c* with the formula unit $Ln_2(dhbq)_3(DMF)_6{\cdot}y$DMF (Figure 3.2, left). Each lanthanide ion is nine-coordinate, with its coordination sphere occupied by three $dhbq^{2-}$ ligands and three DMF molecules; intersheet DMF molecules could not be crystallographically resolved. In contrast, compounds of the smaller lanthanides Tb–Yb crystallized in the space group $P2_1/c$ with the formula unit $Ln_2(dhbq)_3(DMF)_4{\cdot}2$DMF (Figure 3.2). In this case, each lanthanide ion is eight-coordinate, with three $dhbq^{2-}$ ligands and two DMF molecules filling the coordination sphere; two intersheet DMF molecules could also be crystallographically resolved, in agreement with the elemental analysis results. It was not possible to obtain a single-crystal structure for **1-Y** due to poor crystal quality, but this compound appears to be isostructural with the $P2_1/c$ frameworks based on its powder X-ray diffraction pattern (Figure S3.3), an unsurprising result given the similar ionic radii of Y^{3+} and the later lanthanides. Elemental analysis of bulk **1-Y** was also consistent with the analysis performed for the later lanthanides, yielding a formula unit of $Y_2(dhbq)_3(DMF)_4{\cdot}2$DMF.

These frameworks were particularly appealing from a synthetic standpoint due to the high reduction potential of DMF, which is unreactive toward reducing agents as strong as sodium naphthalenide (−3.1 V vs. Fc/Fc^+).[27] As such, isolation of the series **1-Ln** allowed for use of post-synthetic reduction techniques to obtain extended frameworks containing radical $dhbq^{3-}$ ligands. All **1-Ln** powders were found to be quite hygroscopic, however, requiring removal of adventitious water prior to reaction of **1-Ln** with strong reducing reagents. Thus, the as-isolated powders were soaked in anhydrous DMF and dried under reduced pressure in an anhydrous argon atmosphere (see Experimental Details). Elemental analysis of **1-Ln** (Ln = Sm, Eu, Gd) indicated that only the coordinated DMF molecules remain in the isolated anhydrous powders—giving a formula of $Ln_2(dhbq)_3(DMF)_6$. In contrast, elemental analysis of anhydrous **1-Ln** (Ln = Tb–Yb) indicated that all of the crystallographically-ordered DMF molecules remained present in the dry powders, yielding a formula unit of $Ln_2(dhbq)_3(DMF)_4{\cdot}2$DMF.

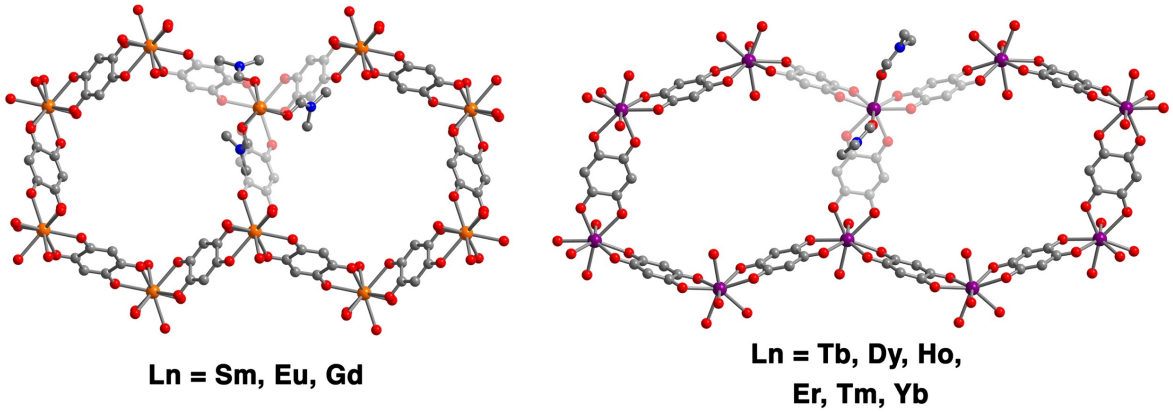

Figure 3.2. Left: Representative structure of $Ln_2(dhbq)_3(DMF)_6{\cdot}y$DMF (Ln = Sm, Eu, Gd) with Ln = Gd. Right: Representative structure of $Ln_2(dhbq)_3(DMF)_4{\cdot}2$DMF (Ln = Tb–Yb) with Ln = Ho. Dark grey, blue, red, orange, and purple spheres represent C, N, O, Gd, and Ho atoms, respectively. Coordinated DMF molecules are highlighted on one lanthanide center in each

structure. Other coordinated DMF molecules, DMF molecules of solvation, and hydrogen atoms are omitted for clarity.

Synthesis and powder X-ray diffraction characterization of 2-Ln (Ln = Y, Tb–Yb). Post-synthetic chemical reduction has only been utilized in a few cases to achieve stoichiometric control over metal and ligand valence states in metal–organic frameworks, and thereby over the framework electronic structure.[18,20,28,29] The choice of reducing agent is important both to ensure a sufficiently high reduction potential and to provide a charge-balancing cation of size suitable for incorporation into the pores or free space of the extended solid. The electrochemical reduction of dhbq-type ligands has been studied in a variety of molecular complexes, and the $dhbq^{2-/3-}$ and $dhbq^{3-}/thb^{4-}$ couples can been placed at approximately −1.4 and −2.0 V versus Fc/Fc^{+} (Fc = ferrocene), respectively.[30,31] We chose sodium naphthalenide as our reducing agent since it is sufficiently reducing (−3.1 V vs. Fc/Fc^{+})[27] to generate $dhbq^{3-}$ and because the relatively small charge-balancing sodium cation should be able to intercalate between the $Ln_2(dhbq)_3(DMF)_x$ sheets. Given that the potential of sodium naphthalenide is high enough to over-reduce the $dhbq^{2-}$ ligand to diamagnetic thb^{4-}, we utilized a 1:1 ratio of $dhbq^{2-}$ to reducing reagent to target clean formation of the desired $dhbq^{3-}$ species. A dark green THF solution of sodium naphthalenide was added dropwise to a stirring suspension of powdered crystalline **1-Ln** in THF at ambient temperature; over the course of the reaction (12 h), the solids changed in color from red-pink to green, and the solution color changed from dark green to colorless. The resulting green solids were isolated by filtration in ≥ 88% yield, indicating a clean reaction and minimal framework decomposition. In the case of **1-Sm**, **1-Eu**, and **1-Gd**, the reduction reactions produced only amorphous powders that were not characterized further—likely the result of a buildup of sodium napthalenide on the particle surfaces that was attributed to the distinct structure of **1-Sm**, **1-Eu**, and **1-Gd** relative to the other **1-Ln** congeners.

Powder X-ray diffraction data for **2-Ln** (Ln = Y, T–Yb) revealed crystalline materials with several low angle peaks similar to those of **1-Ln** (Ln = Tb–Yb, see Figures S3.2 and S3.3), but structural solutions were not pursued due to the low crystal symmetry. Instead, the **2-Ln** compounds were characterized by CHN combustion and sodium ICP analysis to quantify the extent of chemical reduction. It was found that each framework contained 2.2 to 3 molar equivalents of sodium, in addition to a mixture of DMF and THF solvent molecules (see Supporting Information for further details).

Spectroscopic Characterization of 1-Ln and 2-Ln. The carbonyl infrared stretch of quinoid-type ligands is considered a diagnostic handle for the ligand oxidation state. Thus, we first turned to infrared spectroscopy to investigate changes to the ligand manifold in **1-Ln** upon chemical reduction (Figure 3.3, Figures S3.4–S3.6). In **1-Ln**, the carbonyl stretch ranges from 1491–1496 cm^{-1}, which is consistent with the expected $dhbq^{2-}$ assignment,[32] while in **2-Ln** the carbonyl stretch shifts to lower energies ranging from 1452–1454 cm^{-1}, indicative of ligand reduction.[33] Indeed, in the dilanthanide complexes $[CoCp^*_2][(HBpz_3)_2Ln(\mu\text{-}Cl_2dhbq)Ln(HBpz_3)_2]$ (Ln = Dy, Tb, Gd, Y; $HBpz_3^-$ = hydrotris(pyrazol-1-yl)borate) bridged by Cl_2dhbq^{3-}, the radical carbonyl stretch was reported at 1450 cm^{-1},[31] coinciding well with the observed carbonyl stretches and supporting reduction of $dhbq^{2-}$ ligands to the $dhbq^{3-}$ state. When the **2-Ln** compounds are exposed to air, the carbonyl frequencies shift back to higher energies, consistent with aerobic oxidation of $dhbq^{3-}$ to $dhbq^{2-}$ (Figure S3.6).

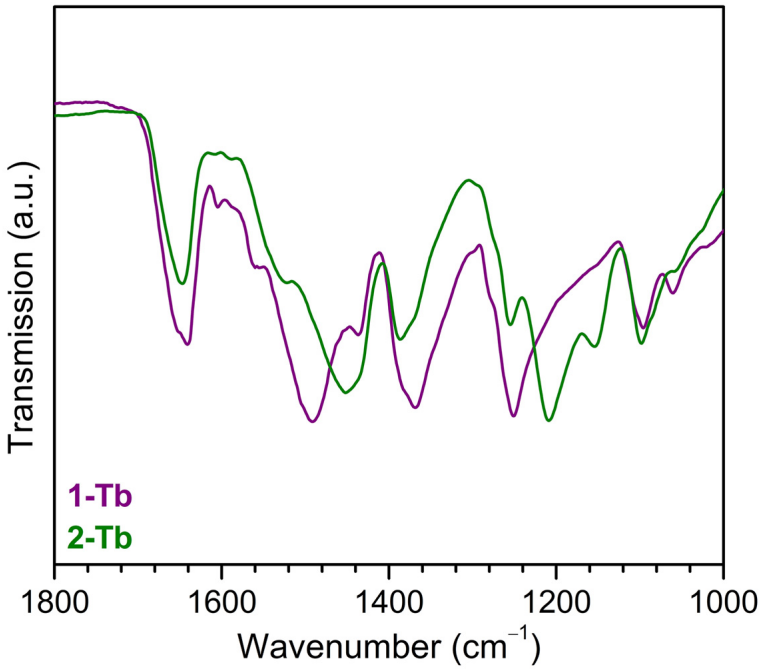

Figure 3.3. Expanded view of the solid-ATR infrared spectra of **1-Tb** (purple) and **2-Tb** (green) highlighting the carbonyl stretch of the dhbq^{n-} ligands. The full IR spectrum of **2-Tb** is given in Figure S3.4.

Similarly, UV-Vis-NIR spectra of **1-Ln** and **2-Ln** were collected to further study framework changes upon chemical reduction. The spectra within each series were found to be qualitatively similar, exhibiting the same features across a small range of shifts, and thus the spectra of the Tb congeners are discussed in detail below as representative examples (Figure 3.4). In the case of **1-Ln**, the UV-Vis-NIR spectra exhibit two bands; for **1-Tb**, the first band centered at 30,000 cm^{-1} was assigned to the π-π^* transition of the dhbq^{2-} ligand, and the second, much less intense band centered at 19,300 cm^{-1} was tentatively assigned to an n-π^* transition. The latter assignment is consistent with electronic transitions of the related ligand *p*-benzoquinone,[34] and a similar band was also observed in the UV-Vis-NIR spectra of $[(HBpz_3)_2Ln(\mu\text{-}Cl_2dhbq)Ln(HBpz_3)_2]^-$.[31] As expected, no charge transfer transitions were observed in the spectra due to the poor energy match of the dhbq^{2-} ligands with the Ln^{III} cations.

In contrast, the spectra of **2-Ln** exhibit five features (Figure 3.4). Again using the representative spectrum of **2-Tb**, a feature centered at 30,500 cm^{-1} was assigned to a ligand π-π^* transition, and three somewhat sharp bands at 21,550, 22,890, and ~24,300 cm^{-1} were assigned to dhbq^{3-} π^*-π^* transitions—again consistent with features in the spectrum of $[(HBpz_3)_2Ln(\mu\text{-}Cl_2dhbq)Ln(HBpz_3)_2]^{-}$[31] as well as the spectrum of the two-dimensional material $((CH_3)_2NH_2)_3Al_4(dhbq^{2-})_3(dhbq^{3-})_3\cdot 3DMF$[35] and molecular $(dhbq\text{-}Cl_2)^{3-}$-bridged complexes.[36] Finally, a weaker, broad feature at 14,600 cm^{-1} was assigned to an intervalence charge transfer (IVCT) transition, arising from the mixture of dhbq^{2-} and dhbq^{3-} ligands in the material. This broad band may obscure n-π^* transitions, predicted to occur at 19837 cm^{-1} and 22062 cm^{-1} for the radical anion *p*-benzosemiquinone.[37] Intervalence charge transfer bands have been previously observed for extended transition metal solids containing mixed-valence dhbq^{n-} ligands,[18,21-23] but these bands typically appear at lower energies and with higher intensities than reported here for **2-**

Ln due to better energy matching of the transition metal frontier orbitals with those of the dhbq^{n-} manifold. Such close metal–ligand orbital energy match can enable Class II/III mixed valence, in which an electron experiences a small thermal barrier to charge transfer and can exhibit spectroscopic characteristics associated with localization or delocalization, depending on the timescale. Alternatively, Class III mixed-valence, in which an electron is fully delocalized across the involved centers, can also be observed. Both scenarios can produce IVCT bands with increased intensity.[38-40] In the case of **2-Ln**, the lanthanide 4f orbitals are much higher in energy than the dhbq^{n-} orbitals and also have very limited radial extension. As a result, dhbq$^{2-/3-}$ ligands are unlikely to communicate extensively via lanthanide orbitals, leading to Class II mixed valence wherein electrons on units of differing valence are localized on their respective centers and experience a thermal barrier to electron transfer.

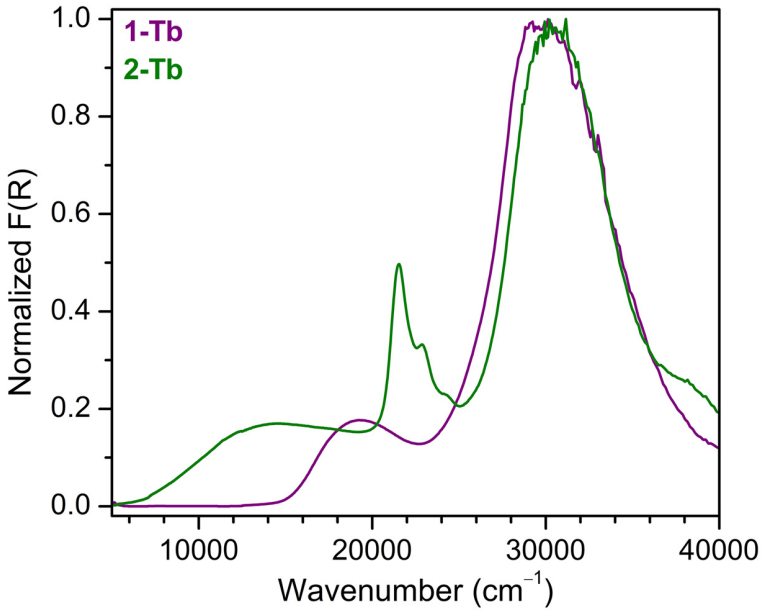

Figure 3.3. Normalized UV-Vis-NIR diffuse reflectance spectra of **1-Tb** (purple) and **2-Tb** (green), with the most intense feature set to F(R) = 1.

Magnetic characterization of 2-Ln. The compounds **2-Ln** were further characterized via dc magnetic susceptibility measurements to better quantify the paramagnetic dhbq^{3-} ligands present and to investigate the degree of magnetic exchange between the lanthanide ions and radicals. A summary of the resulting relevant magnetic parameters is given in Table 3.1.

Table 3.1. Calculated values of the magnetic susceptibility times temperature ($\chi_M T$) or Curie constant (C) in units of emu·K/mol; experimental values of $\chi_M T$ (emu·K/mol); and experimental Curie-Weiss temperatures (θ, units of K) for **2-Ln** (Ln = Y, Tb–Yb). All data were collected at 300 K and 0.1 T, unless otherwise specified.

2-Ln	$dhbq^{3-}$ ligands[†]	Calcd $\chi_M T$ or C	Expt $\chi_M T$	θ	C
2-Y	2.2	0.83	0.75 (0.65)[‡]	−89.6[*]	0.84[*]
2-Tb	2.7	24.69	23.27	−10.0	24.2
2-Dy	2.5	29.28	29.75	−10.5	31.0
2-Ho	3	29.27	27.57	−12.7	28.8
2-Er	2.7	23.97	23.79	−11.9	24.8
2-Tm	3	15.43	14.97	−17.6	15.9
2-Yb	2.2	5.97	5.70 (5.12)[‡]	(−70.9)[*§]	(6.3)[*§]

[†]Proposed number per formula unit based on molar equivalents of Na

[‡]Data collected at 1 T

*Fits to the Curie-Weiss equation were performed on data collected at 1 T in order to minimize contributions from excited states.

[§]Curie-Weiss fit values are potentially distorted by contributions from excited states that persisted even under a 1 T magnetic field, as reflected by the imperfect matching between C and Calcd $\chi_M T$ (equivalent to Calcd C).

Compound **2-Y** was first measured as a benchmark to confirm that the chemical reduction of **1-Ln** results in paramagnetic $dhbq^{3-}$ linkers, and not simply a mixture of diamagnetic $dhbq^{2-}$ and thb^{4-} ligands—indeed, because Y^{III} is diamagnetic, the presence of any paramagnetism for **2-Y** should be solely ligand-based. Under an applied magnetic field of 0.1 T, the room-temperature (300 K) value of the magnetic susceptibility times temperature ($\chi_M T$) for **2-Y** is 0.75 emu·K/mol, while under an applied field of 1 T this value decreases slightly to 0.65 emu·K/mol (Figure 3.5). Both these $\chi_M T$ products approach the value of 0.83 emu·K/mol expected for 2.2 magnetically-isolated $S = 1/2$ spins. The $\chi_M T$ product decreases steadily with decreasing temperature, behavior indicative of antiferromagnetic coupling between radical spins. The 1 T data were fit to the Curie-Weiss equation:

$$\chi = \frac{C}{T - \theta} \qquad (3.1)$$

where C and θ represent the Curie and Weiss constants, respectively. The fit yielded a value of C = 0.84 emu·K/mol—consistent with the expected value of 0.83 emu·K/mol for 2.2 isolated $S = 1/2$ spins—and a large negative θ of −89.6 K. The magnitude and sign of the Weiss constant affords a qualitative picture of the nature and strength of magnetic exchange within a system, and such a large negative value is indicative of substantial antiferromagnetic exchange between radical spins. For comparison, ligand radical-radical exchange across Y^{III} cations has been evaluated for a series of yttrium nitronyl nitroxide chains to range from −15 to −24 cm^{-1}.[41] High-resolution X-ray diffraction, polarized neutron diffraction, and DFT characterization of an yttrium–semiquinone radical complex indicated that charge and spin transfer from the semiquinone to Y^{III} occurs from a π-type orbital—delocalized on the semiquinone oxygen and carbon atoms—to both the 4d and 5s orbitals of Y^{III}.[42] Similarly, superexchange between $dhbq^{3-}$ radicals in **2-Y** is expected to proceed through the unoccupied yttrium 4d and 5s orbitals. The magnetization of **2-Y** at 7 T and

2 K is 0.37 μ_B, somewhat higher than the expected value of 0.2 μ_B for antiferromagnetic ordering between radical spins, possibly indicating that the framework has a noncollinear magnetic ground state. Unexpectedly, **2-Y** also exhibits waist-restricted magnetic hysteresis at 2 K (Figure 3.5, inset). Low-temperature ac magnetic susceptibility measurements revealed that this hysteresis arises from metamagnetic behavior, wherein magnetic ordering is triggered by an applied magnetic field of requisite strength. A field of 2 T promotes magnetic ordering in the case of **2-Y**, as indicated by a cusp in the in-phase magnetic susceptibility (χ') data collected at 3 K (Figure S3.7).

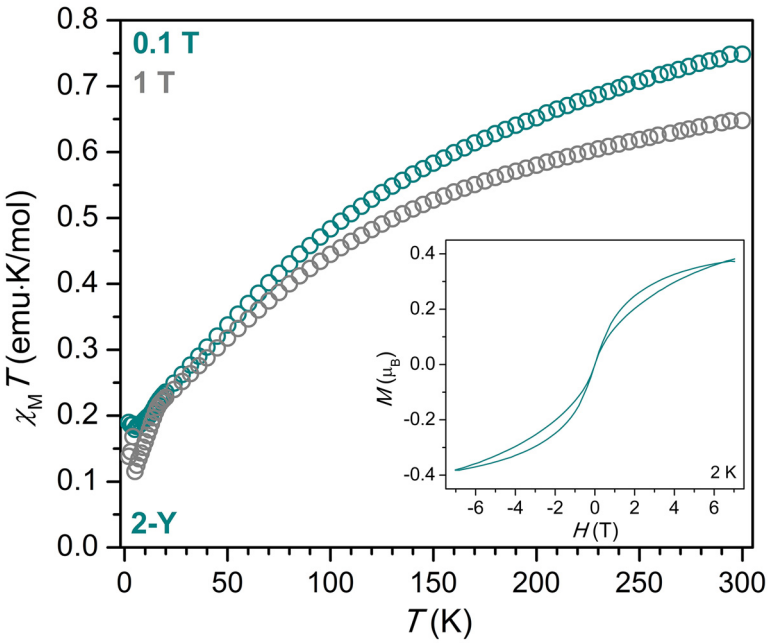

Figure 3.5. Magnetic susceptibility times temperature product ($\chi_M T$) versus temperature for the material **2-Y**, collected under applied magnetic fields of 0.1 T and 1 T. Inset: Magnetization versus field data for **2-Y** collected at 2 K, using a magnetic field sweep rate of 0.20 mT/s.

Most of the lanthanide ions exhibit intrinsic magnetic anisotropy due to spin-orbit coupling of their spin and orbital angular momentum. It was anticipated that this magnetic anisotropy may produce magnetic materials with enhanced magnetic hysteresis behavior. To begin, material **2-Tb** was studied under an applied magnetic field of 0.1 T, at which a $\chi_M T$ product of 23.27 emu·K/mol was observed, somewhat lower than the expected 24.69 emu·K/mol, for two Tb^{III} ions and 2.7 radical ligands (Figure 3.6). The $\chi_M T$ product decreased to 19.97 emu·K/mol at 20 K, followed by a rise in $\chi_M T$ to 24.03 emu·K/mol at 4 K. Magnetic hysteresis measurements at 2 K revealed a small magnetic hysteresis with a coercive field, H_C, of 130 Oe. In order to determine whether bulk magnetic ordering occurred, ac magnetic susceptibility measurements were performed. A peak in the out-of-phase magnetic susceptibility was observed for **2-Tb** at 3 K and 1000 Hz, concurrent with a rise in the in-phase susceptibility (Figure S3.9). Both the in- and out-of-phase magnetic susceptibility signals moved to lower temperatures with lower frequency, indicative of glassy magnetic ordering. Magnetic glassiness can be ascribed to either local magnetic order, in which ordered spin clusters of varying size are present, or to magnetic frustration. [43] Due to the anticipated localized nature of lanthanide-radical magnetic exchange in the **2-Ln** series, we ascribe the glassy behavior observed for **2-Tb** to local magnetic ordering.

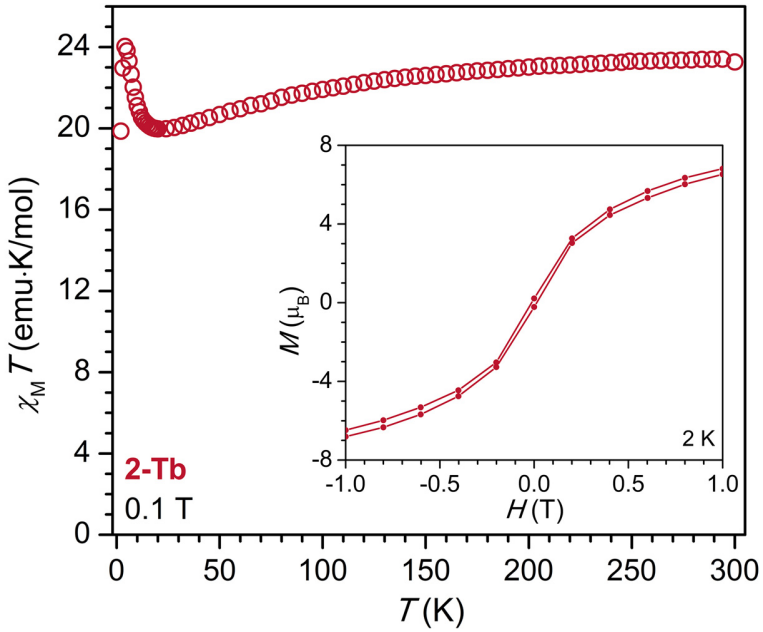

Figure 3.6. Magnetic susceptibility times temperature product ($\chi_M T$) versus temperature for the material **2-Tb**, collected under an applied magnetic field of 0.1 T. Inset: Zoomed-in hysteresis (magnetization versus field) data for **2-Tb** collected at 2 K, using a field sweep rate of 0.20 mT/s.

Materials **2-Dy**, **2-Ho**, **2-Er**, **2-Tm**, and **2-Yb** exhibit magnetic behavior similar to that of **2-Tb** (Table 3.1 and Figure 3.7). Each material shows a $\chi_M T$ product close to that expected for its number of radical dhbq^{3-} ligands (Table 1), followed by a decrease in $\chi_M T$ with decreasing temperature. None of these four materials exhibited magnetic ordering or magnetic hysteresis. The compounds **2-Dy**, **2-Ho**, **2-Tm**, and **2-Yb** show local minima in their $\chi_M T$ products at 18 K, 19 K, 12 K, and 17 K, respectively, followed by a small rise in $\chi_M T$ with further decreasing temperature. Unusually, **2-Er** shows a much higher-temperature local minimum, occurring at 75 K, but with little if any subsequent rise in $\chi_M T$. When **2-Ln** incorporates an anisotropic lanthanide ion, the temperature dependence of its $\chi_M T$ product reflects the combination of magnetic exchange effects and effects due to depopulation of the lanthanide ions' crystal-field-split M_J multiplets, as well as a typically small contribution from Zeeman splitting. It is possible that **2-Er** experiences stronger crystal field splitting of its Ln^{III} ions than **2-Tb**, **2-Dy**, **2-Ho**, and **2-Tm**, obscuring the effects of lanthanide-radical and radical-radical magnetic exchange. Though the crystal structure of **2-Ln** is unknown, a predominantly equatorial crystal field would be expected to lead to stronger crystal field splitting in the case of lanthanide ions with axially-elongated ("prolate") electron density, such as **2-Er**, **2-Tm**, and **2-Yb**.[44] While the difference in temperature dependence of $\chi_M T$ is most obvious for **2-Er**, the local minima and subsequent increases in $\chi_M T$ ascribed to magnetic exchange are less pronounced for **2-Tm** and **2-Yb** as well when compared to those of **2-Tb**, **2-Dy**, and **2-Ho**.

Interestingly, the Curie-Weiss temperature, θ, the magnitude of which should reflect the strength of radical-radical and lanthanide-radical magnetic exchange, appears to trend with decreasing lanthanide ionic radius, increasing from –10 K for **2-Tb** to –17.6 K for **2-Tm** (Table 3.1). This trend may possibly be ascribed to a decreasing bond distance between the lanthanide ions and the oxygen atoms of the dhbq^{n-} ligands, expected as the ionic radius of the lanthanide ion

decreases and effective nuclear charge increases. Magnetic exchange strength, both for direct magnetic exchange and superexchange, is dependent on the distance between participating spin centers. Considering that substantial spin density resides on the oxygen atoms of the dhbq^{3-} ligands, small changes in the lanthanide-oxygen distance, such as those expected with changing lanthanide ionic radius, may significantly affect magnetic exchange strength.

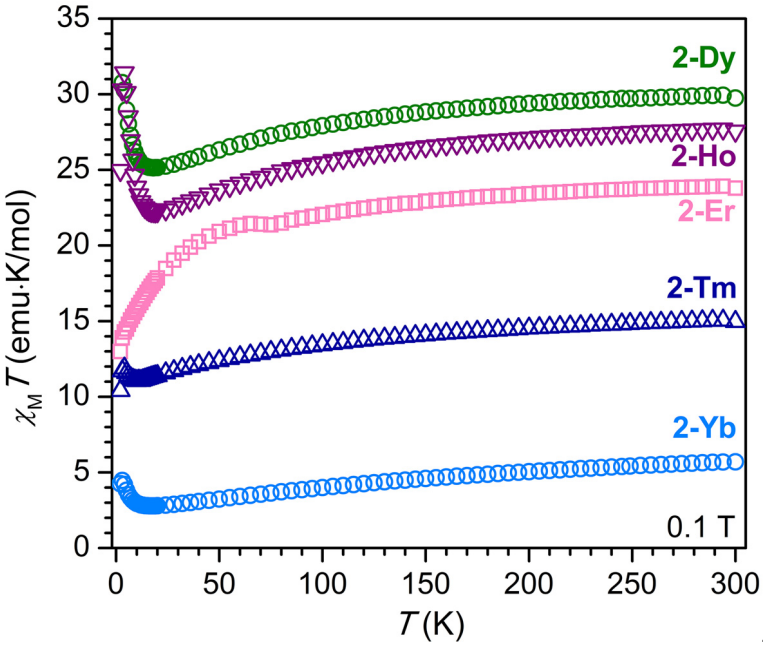

Figure 3.7. Magnetic susceptibility times temperature product ($\chi_M T$) versus temperature for the materials **2-Dy**, **2-Ho**, **2-Er**, **2-Tm**, and **2-Yb**, represented by green circles, purple upside-down triangles, pink squares, dark blue triangles, and light blue circles, respectively, collected under an applied magnetic field of 0.1 T.

Next, the compound **2-Yb** was of particular interest due to its lower reduction potential, which may enable better energy match of the 4f orbitals with the frontier orbitals of the dhbq^{n-} ligands, leading to stronger metal-radical magnetic exchange. Unfortunately, **2-Yb** did not exhibit magnetic ordering. The material **2-Yb** appears to exhibit temperature-independent paramagnetism behavior, in which magnetic excited states are populated with increasing temperature, leading to a linear increase in $\chi_M T$ with increasing temperature (Figure 3.7). At 300 K, $\chi_M T$ values of 5.70 (0.1 T) and 5.12 (1 T) emu·K/mol are observed for **2-Yb**, compared to the expected value of 5.97 emu·K/mol. While the $\chi_M T$ values of **2-Yb** were not unrealistic, the corresponding Curie-Weiss fit of the 1 T data produced a large θ value of –70.9 K (Table 3.1). Given the lack of bulk magnetic ordering in **2-Yb**, this large θ value seemed unrealistic, likely reflecting a disruption in ideal Curie behavior due to participation of magnetic excited states. This assumption notwithstanding, large θ values have been previously observed without leading to bulk magnetic ordering in cases of localization of metal-radical exchange, for instance in the related material $(H_2NMe_2)_{1.5}Cr_2(dhbq)_3$, which may produce exchange-coupled metal-radical clusters that are magnetically isolated from one another, rather than a continuous magnetic exchange pathway throughout the bulk material.[23] Given the previously mentioned limitation of dhbq^{n-} ligand communication via the poor radial extension and high energy of the 4f orbitals, it is not impossible that such a θ value is real, and

simply reflects highly localized magnetic exchange. These competing scenarios may only be distinguished through continued study of lanthanide-radical coordination solids in series.

Finally, the lack of bulk magnetic order in the series **2-Ln** (Ln = Tb –Yb), though disappointing, is interesting to explore. One related system of interest, a three-dimensional lanthanide-catecholate framework composed of Ho^{III} ions and thb^{4-} ions, has been shown to ferromagnetically order at 11 K with a moderate coercive field of 170 Oe at 2 K. [45] It was anticipated that incorporation of paramagnetic $dhbq^{3-}$ centers in the place of thb^{4-} ions could only increase the magnetic ordering temperature in this class of materials. One explanation for this discrepancy lies in the substantial antiferromagnetic radical-radical exchange observed for **2-Y**. Antiferromagnetic radical-radical superexchange is likely to compete with comparatively weaker lanthanide-radical antiferromagnetic exchange, preventing bulk magnetic order. An ideal lanthanide-radical magnetic material would instead exhibit strong antiferromagnetic lanthanide-radical exchange and either ferromagnetic radical-radical exchange or negligible radical-radical magnetic exchange to generate a ferrimagnetic ground state with opposing lanthanide and radical spins.

3.4 Conclusions and Outlook

In conclusion, a series of semiquinoid radical-bridged lanthanide frameworks has been synthesized via post-synthetic chemical reduction techniques and investigated spectroscopically and magnetically. IR and UV-Vis-NIR spectroscopy exhibit features consistent with the presence of $dhbq^{3-}$ radical ligands in the two-dimensional frameworks **2-Ln**. Magnetic susceptibility measurements on the yttrium derivative **2-Y** indicate that antiferromagnetic radical-radical exchange occurs. While the material **2-Tb** exhibits glassy magnetic ordering at low temperature with a small coercive field of 130 Oe at 2 K, the materials **2-Dy**, **2-Ho**, **2-Er**, **2-Tm**, and **2-Yb** surprisingly do not exhibit magnetic ordering. Effects such as the crystal field environment generated by the radical ligands and competing radical-radical and lanthanide-radical exchange pathways are discussed as complicating factors for the pursuit of bulk magnetic order in lanthanide-radical extended solids.

3.5 Acknowledgements

This work was supported by the Nanoporous Materials Genome Center of the U.S. Department of Energy, Office of Basic Energy Sciences, Division of Chemical Sciences, Geosciences and Biosciences under Award No. DE-FG02-17ER16362. Single-crystal X-ray diffraction data and powder X-ray diffraction patterns were collected, respectively, at Beamlines 12.2.1 and 12.2.2 at the Advanced Light Source. The Advanced Light Source is supported by the Director, Office of Science, Office of Basic Energy Sciences, of the U.S. Department of Energy under Contract No. DE-AC02-05CH11231. L.E.D. thanks the NSF GRFP program for graduate fellowship support and Ari B. Turkiewicz for assistance with the single-crystal X-ray diffraction experiments and data analysis.

3.6 References

(1) Gutfleisch, O.; Willard, M. A.; Brück, E.; Chen, C. H.; Sankar, S. G.; Liu, J. P. *Adv. Mater.* **2010**, *23*, 821.
(2) Croat, J. J.; Herbst, J. F.; Lee, R. W.; Pinkerton, F. E. *Appl. Phys. Lett.* **1984**, *44*, 148.
(3) Hirosawa, S.; Matsuura, Y.; Yamamoto, H.; Fujimura, S.; Sagawa, M.; Yamauchi, H. *J. Appl. Phys.* **1986**, *59*, 873.
(4) Strnat, K.; Hoffer, G.; Olson, J.; Ostertag, W.; Becker, J. J. *J. Appl. Phys.* **1967**, *38*, 1001.
(5) Kreno, L. E.; Leong, K.; Farha, O. K.; Allendorf, M.; Van Duyne, R. P.; Hupp, J. T. *Chem. Rev.* **2012**, *112*, 1105.
(6) Furukawa, H.; Cordova, K. E.; O'Keeffe, M.; Yaghi, O. M. *Science* **2013**, *341*, 1230444.
(7) Verdaguer, M.; Bleuzen, A.; Marvaud, V.; Vaissermann, J.; Seuleiman, M.; Desplanches, C.; Scuiller, A.; Train, C.; Garde, R.; Gelly, G.; Lomenech, C.; Rosenman, I.; Veillet, P.; Cartier, C.; Villain, F. *Coord. Chem. Rev.* **1999**, *190-192*, 1023.
(8) Morin, B. G.; Hahm, C.; Miller, J. S.; Epstein, A. J. *J. Appl. Phys.* **1994**, *74*, 5782.
(9) Dechambenoit, P.; Long, J. R. *Chem. Soc. Rev.* **2011**, *40*, 3249.
(10) Coronado, E.; Mínguez Espallargas, G. *Chem. Soc. Rev.* **2013**, *42* (4), 1525.
(11) Kurmoo, M. *Chem. Soc. Rev.* **2009**, *38*, 1353.
(12) Miller, J. S. *Chem. Soc. Rev.* **2011**, *40*, 3266.
(13) Manriquez, J. M.; Yee, G. T.; McLean, R. S.; Epstein, A. J.; Miller, J. S. *Science* **1991**, *252*, 1415.
(14) Datcu, A.; Roques, N.; Jubera, V.; Imaz, I.; Maspoch, D.; Sutter, J.-P.; Rovira, C.; Veciana, J. *Chem. Eur. J.* **2011**, *17*, 3644.
(15) Raebiger, J. W.; Miller, J. S. *Inorg. Chem.* **2002**, *41*, 3308.
(16) Zhao, H.; Bazile, M. J.; Galán-Mascarós, J. R.; Dunbar, K. R. *Angew. Chem. Int. Ed.* **2003**, *42*, 1015.
(17) Ballesteros-Rivas, M.; Zhao, H.; Prosvirin, A.; Reinheimer, E. W.; Toscano, R. A.; Valdés-Martínez, J.; Dunbar, K. R. *Angew. Chem. Int. Ed.* **2012**, *51*, 5124.
(18) Darago, L. E.; Aubrey, M. L.; Yu, C. J.; Gonzalez, M. I.; Long, J. R. *J. Am. Chem. Soc.* **2015**, *137*, 15703.
(19) Jeon, I.-R.; Negru, B.; Van Duyne, R. P.; Harris, T. D. *J. Am. Chem. Soc.* **2015**, *137*, 15699.
(20) DeGayner, J. A.; Jeon, I.-R.; Sun, L.; Dincă, M.; Harris, T. D. *J. Am. Chem. Soc.* **2017**, *139*, 4175.
(21) Murase, R.; Abrahams, B. F.; D'Alessandro, D. M.; Davies, C. G.; Hudson, T. A.; Jameson, G. N. L.; Moubaraki, B.; Murray, K. S.; Robson, R.; Sutton, A. L. *Inorg. Chem.* **2017**, *56*, 9025.
(22) Kingsbury, C. J.; Abrahams, B. F.; D'Alessandro, D. M.; Hudson, T. A.; Murase, R.; Robson, R.; White, K. F. *Cryst. Grow. Des.* **2017**, *17*, 1465.
(23) Ziebel, M. E.; Darago, L. E.; Long, J. R. *J. Am. Chem. Soc.* **2018**, *140*, 3040.
(24) Abrahams, B. F.; Coleiro, J.; Hoskins, B. F.; Robson, R. *Chem. Commun.* **1996**, *5*, 603.
(25) Benmansour, S.; Hernández-Paredes, A.; Gómez-García, C. J. *J. Coord. Chem.* **2018**, *71*, 845.
(26) Gómez-Claramunt, P.; Benmansour, S.; Hernández-Paredes, A.; Cerezo-Navarrete, C.; Rodríguez-Fernández, C.; Canet-Ferrer, J.; Cantarero, A.; Gómez-García, C. *Magnetochemistry* **2018**, *4*, 6.
(27) Connelly, N. G.; Geiger, W. E. *Chem. Rev.* **1996**, *96*, 877.

(28) Meilikhov, M.; Yusenko, K.; Torrisi, A.; Jee, B.; Mellot-Draznieks, C.; Pöppl, A.; Fischer, R. A. *Angew. Chem. Int. Ed.* **2010**, *49*, 6212.
(29) Kambe, T.; Sakamoto, R.; Kusamoto, T.; Pal, T.; Fukui, N.; Hoshiko, K.; Shimojima, T.; Wang, Z.; Hirahara, T.; Ishizaka, K.; Hasegawa, S.; Liu, F.; Nishihara, H. *J. Am. Chem. Soc.* **2014**, *136*, 14357.
(30) Min, K. S.; DiPasquale, A. G.; Golen, J. A.; Rheingold, A. L.; Miller, J. S. *J. Am. Chem. Soc.* **2007**, *129*, 2360.
(31) Zhang, P.; Perfetti, M.; Kern, M.; Hallmen, P. P.; Ungur, L.; Lenz, S.; Ringenberg, M. R.; Frey, W.; Stoll, H.; Rauhut, G.; van Slageren, J. *Chem. Sci.* **2018**, *9*, 1221.
(32) Kitagawa, S.; Kawata, S. *Coord. Chem. Rev.* **2002**, *224*, 11.
(33) Zhao, X.; Imahori, H.; Zhan, C.-G.; Sakata, Y.; Iwata, S.; Kitagawa, T. *J. Phys. Chem. A* **1997**, *101*, 622.
(34) Trommsdorff, H. P. *J. Chem. Phys.* **1972**, *56*, 5358.
(35) Halis, S.; Inge, A. K.; Dehning, N.; Weyrich, T.; Reinsch, H.; Stock, N. *Inorg. Chem.* **2016**, *55*, 7425.
(36) Guo, D.; McCusker, J. K. *Inorg. Chem.* **2007**, *46*, 3257.
(37) Wheeler, R. A. *J. Phys. Chem.* **1993**, *97*, 1533.
(38) Robin, M. B.; Day, P. Mixed Valence Chemistry-A Survey and Classification. In *Advances in Inorganic Chemistry and Radiochemistry*; Elsevier, 1968; Vol. 10, 247–422.
(39) Demadis, K. D.; Hartshorn, C. M.; Meyer, T. J. *Chem. Rev.* **2001**, *101*, 2655.
(40) D'Alessandro, D. M.; Keene, F. R. *Chem. Soc. Rev.* **2006**, *35*, 424.
(41) Jung, J.; Puget, M.; Cador, O.; Bernot, K.; Calzado, C. J.; Le Guennic, B. *Inorg. Chem.* **2017**, *56*, 6788.
(42) Claiser, N.; Souhassou, M.; Lecomte, C.; Gillon, B.; Carbonera, C.; Caneschi, A.; Dei, A.; Gatteschi, D.; Bencini, A.; Pontillon, Y.; Lelièvre-Berna, E. *J. Phys. Chem. B* **2005**, *109*, 2723.
(43) Clérac, R.; O'Kane, S.; Cowen, J.; Ouyang, X.; Heintz, R.; Zhao, H.; Bazile, M. J.; Dunbar, K. R. *Chem. Mater.* **2003**, *15*, 1840.
(44) Rinehart, J. D.; Long, J. R. *Chem. Sci.* **2011**, *2*, 2078.
(45) Nakabayashi, K.; Ohkoshi, S.-I. *Inorg. Chem.* **2009**, *48*, 8647.

Chapter 3 Supporting Information

S3.1 Experimental Details.

Synthesis of $Sm_2(dbhq)_3(DMF)_6$ (1-Sm). Material **1-Sm** was prepared in a manner similar to **1-Tb**. A solution of 329.0 mg (2.35 mmol) of H_2dhbq in 4 mL of DMF was layered on top of a solution of 695.9 mg (1.57 mmol) of $Sm(NO_3)_3 \cdot 6H_2O$ in 4 mL of DMF in a 20 mL scintillation vial. The vial was then placed in a steel heating block placed on a hot plate set to 60 °C. Solids of **1-Sm**, including single crystals, formed after 1 d. Heating was continued for a total of 3 d, upon which the vial was removed from the heating block and allowed to cool. After cooling, dark red crystalline solids of **1-Sm** were isolated by filtration. The product was dried under reduced pressure for 4 h. Solids of **1-Sm** were brought into a VAC glovebox under an argon atmosphere. These solids were crushed into a pink powder and soaked in anhydrous DMF for 12 h, isolated by filtration, and dried under reduced pressure for 15 m. Yield: 137.0 mg (6.7%). Anal. Calcd. for $C_{36}H_{48}Sm_2N_6O_{18}$: C, 37.48; H, 4.19; N, 7.29. Found: C, 37.35; H, 4.05; N, 7.33.

Synthesis of $Eu_2(dbhq)_3(DMF)_6$ (1-Eu). Material **1-Eu** was prepared in a manner similar to **1-Tb**. A solution of 245.4 mg (1.75 mmol) of H_2dhbq in 4 mL of DMF was layered on top of a solution of 415.7 mg (1.17 mmol) of $Eu(NO_3)_3 \cdot H_2O$ in 4 mL of DMF in a 20 mL scintillation vial. The vial was then placed in a steel heating block placed on a hot plate set to 60 °C. Solids of **1-Eu**, including single crystals, formed after 1 d. Heating was continued for a total of 3 d, upon which the vial was removed from the heating block and allowed to cool. After cooling, dark red crystalline solids of **1-Eu** were isolated by filtration. The product was dried under reduced pressure for 4 h. Solids of **1-Eu** were brought into a VAC glovebox under an argon atmosphere. These solids were crushed into a pink powder and soaked in anhydrous DMF for 12 h, isolated by filtration, and dried under reduced pressure for 15 m. Yield: 103.5 mg (7.7%). Anal. Calcd. for $C_{36}H_{48}Eu_2N_6O_{18}$: C, 37.38; H, 4.18; N, 7.27. Found: C, 37.75; H, 4.29; N, 7.49.

Synthesis of $Gd_2(dbhq)_3(DMF)_6$ (1-Gd). Material **1-Gd** was prepared in a manner similar to **1-Tb**. A solution of 237.3 mg (1.69 mmol) of H_2dhbq in 4 mL of DMF was layered on top of a solution of 509.6 mg (1.13 mmol) of $Gd(NO_3)_3 \cdot 6H_2O$ in 4 mL of DMF in a 20 mL scintillation vial. The vial was then placed in a steel heating block placed on a hot plate set to 60 °C. Solids of **1-Gd**, including single crystals, formed after 1 d. Heating was continued for a total of 3 d, upon which the vial was removed from the heating block and allowed to cool. After cooling, dark red crystalline solids of **1-Gd** were isolated by filtration. The product was dried under reduced pressure for 4 h. Solids of **1-Gd** were brought into a VAC glovebox under an argon atmosphere. These solids were crushed into a pink powder and soaked in anhydrous DMF for 12 h, isolated by filtration, and dried under reduced pressure for 15 m. Yield: 115.3 mg (8.7%). Anal. Calcd. for $C_{36}H_{48}Gd_2N_6O_{18}$: C, 37.04; H, 4.14; N, 7.20. Found: C, 37.26; H, 4.23; N, 7.40.

Synthesis of $Dy_2(dbhq)_3(DMF)_4 \cdot 2$ DMF (1-Dy). Material **1-Dy** was prepared in a manner similar to **1-Tb**. A solution of 246.0 mg (1.76 mmol) of H_2dhbq in 4 mL of DMF was layered on top of a solution of 534.6 mg (1.17 mmol) of $Dy(NO_3)_3 \cdot 6H_2O$ in 4 mL of DMF in a 20 mL scintillation vial. The vial was then placed in a steel heating block placed on a hot plate set to 60 °C. Solids of **1-Dy**, including single crystals, formed after 1 d. Heating was continued for a total of 36 h, upon

which the vial was removed from the heating block and allowed to cool. After cooling, dark red crystalline solids of **1-Dy** were isolated by filtration. The product was dried under reduced pressure for 4 h. Solids of **1-Dy** were brought into a VAC glovebox under an argon atmosphere. These solids were crushed into a pink powder and soaked in anhydrous DMF for 12 h, isolated by filtration, and dried under reduced pressure for 15 m. Yield: 237.0 mg (17.1%). Anal. Calcd. for $C_{36}H_{48}Dy_2N_6O_{18}$: C, 36.71; H, 4.11; N, 7.14. Found: C, 36.46; H, 3.99; N, 7.08.

Synthesis of $Ho_2(dbhq)_3(DMF)_4 \cdot 2$ DMF (1-Ho). Material **1-Ho** was prepared in a manner similar to **1-Tb**. A solution of 318.9 mg (2.28 mmol) of H_2dhbq in 4 mL of DMF was layered on top of a solution of 532.6 mg (1.52 mmol) of $Ho(NO_3)_3 \cdot H_2O$ in 4 mL of DMF in a 20 mL scintillation vial. The vial was then placed in a steel heating block placed on a hot plate set to 60 °C. Solids of **1-Ho**, including single crystals, formed after 1 d. Heating was continued for a total of 36 h, upon which the vial was removed from the heating block and allowed to cool. After cooling, dark red crystalline solids of **1-Ho** were isolated by filtration. The product was dried under reduced pressure for 4 h. Solids of **1-Ho** were brought into a VAC glovebox under an argon atmosphere. These solids were crushed into a pink powder and soaked in anhydrous DMF for 12 h, isolated by filtration, and dried under reduced pressure for 15 m. Yield: 279.3 mg (15.6%). Anal. Calcd. for $C_{36}H_{48}Er_2N_6O_{18}$: C, 36.56; H, 4.09; N, 7.11. Found: C, 36.24; H, 3.94; N, 7.04.

Synthesis of $Er_2(dbhq)_3(DMF)_4 \cdot 2$ DMF (1-Er). Material **1-Er** was prepared in a manner similar to **1-Tb**. A solution of 337.4 mg (2.41 mmol) of H_2dhbq in 4 mL of DMF was layered on top of a solution of 567.2 mg (1.61 mmol) of $Er(NO_3)_3 \cdot H_2O$ in 4 mL of DMF in a 20 mL scintillation vial. The vial was then placed in a steel heating block placed on a hot plate set to 60 °C. Solids of **1-Er**, including single crystals, formed after 1 d. Heating was continued for a total of 36 h, upon which the vial was removed from the heating block and allowed to cool. After cooling, dark red crystalline solids of **1-Er** were isolated by filtration. The product was dried under reduced pressure for 4 h. Solids of **1-Er** were brought into a VAC glovebox under an argon atmosphere. These solids were crushed into a pink powder and soaked in anhydrous DMF for 12 h, isolated by filtration, and dried under reduced pressure for 15 m. Yield: 358.7 mg (19.0 %). Anal. Calcd. for $C_{36}H_{48}Er_2N_6O_{18}$: C, 36.42; H, 4.08; N, 7.08. Found: C, 36.27; H, 3.92; N, 7.08.

Synthesis of $Tm_2(dbhq)_3(DMF)_4 \cdot 2$ DMF (1-Tm). Material **1-Tm** was prepared in a manner similar to **1-Tb**. A solution of 204.3 mg (1.46 mmol) of H_2dhbq in 4 mL of DMF was layered on top of a solution of 432.7 mg (0.97 mmol) of $Tm(NO_3)_3 \cdot 5H_2O$ in 4 mL of DMF in a 20 mL scintillation vial. The vial was then placed in a steel heating block placed on a hot plate set to 60 °C. Solids of **1-Tm**, including single crystals, formed after 1 d. Heating was continued for a total of 36 h, upon which the vial was removed from the heating block and allowed to cool. After cooling, dark red crystalline solids of **1-Tm** were isolated by filtration. The product was dried under reduced pressure for 4 h. Solids of **1-Tm** were brought into a VAC glovebox under an argon atmosphere. These solids were crushed into a pink powder and soaked in anhydrous DMF for 12 h, isolated by filtration, and dried under reduced pressure for 15 m. Yield: 339.0 mg (29.3%). Anal. Calcd. for $C_{36}H_{48}Tm_2N_6O_{18}$: C, 36.32; H, 4.06; N, 7.06. Found: C, 36.28; H, 4.07; N, 7.17.

Synthesis of $Yb_2(dbhq)_3(DMF)_4 \cdot 2$ DMF (1-Yb). Material **1-Yb** was prepared in a manner similar to **1-Tb**. A solution of 222.9 mg (1.59 mmol) of H_2dhbq in 4 mL of DMF was layered on top of a solution of 495.6 mg (1.06 mmol) of $Yb(NO_3)_3 \cdot 6H_2O$ in 4 mL of DMF in a 20 mL scintillation vial. The vial was then placed in a steel heating block placed on a hot plate set to 60 °C. Solids of **1-Yb**, including single crystals, formed after 1 d. Heating was continued for a total of 36 h, upon which the vial was removed from the heating block and allowed to cool. After cooling, dark red crystalline solids of **1-Yb** were isolated by filtration. The product was dried under reduced pressure for 4 h. Solids of **1-Yb** were brought into a VAC glovebox under an argon atmosphere. These solids were crushed into a pink powder and soaked in anhydrous DMF for 12 h, isolated by filtration, and dried under reduced pressure for 15 m. This allowed all manipulations of **1-Yb** to be performed under ambient conditions. Yield: 385.6 mg (30.3%). Anal. Calcd. for $C_{36}H_{48}Yb_2N_6O_{18}$: C, 36.07; H, 4.04; N, 7.01. Found: C, 36.04; H, 3.93; N, 7.01.

Synthesis of $Y_2(dbhq)_3(DMF)_4 \cdot 2$ DMF (1-Y). Material **1-Y** was prepared in a manner similar to **1-Tb**. A solution of 266.5 mg (1.90 mmol) of H_2dhbq in 4 mL of DMF was layered on top of a solution of 485.8 mg (1.27 mmol) of $Y(NO_3)_3 \cdot H_2O$ in 4 mL of DMF in a 20 mL scintillation vial. The vial was then placed in a steel heating block placed on a hot plate set to 60 °C. Solids of **1-Y**, including single crystals, formed after 1 d. Heating was continued for a total of 36 h, upon which the vial was removed from the heating block and allowed to cool. After cooling, dark red crystalline solids of **1-Y** were isolated by filtration. The product was dried under reduced pressure for 4 h. Solids of **1-Y** were brought into a VAC glovebox under an argon atmosphere. These solids were crushed into a pink powder and soaked in anhydrous DMF for 12 h, isolated by filtration, and dried under reduced pressure for 15 m. Yield: 243.3 mg (18.6%). Anal. Calcd. for $C_{36}H_{48}Y_2N_6O_{18}$: C, 41.96; H, 4.69; N, 8.15. Found: C, 41.58; H, 4.41; N, 7.91.

Synthesis of $Na_{2.7}Tb_2(dbhq)_3(DMF)_{2.3}(THF)_{0.6}$ (2-Tb). A solution of the reducing agent sodium napthalenide was prepared by stirring 42.8 mg (0.334 mmol) of naphthalene in tetrahydrofuran over roughly 2-fold excess sodium for 3 h. The dark green sodium naphthalenide solution was then added to a stirring suspension of 130.3 mg (0.111 mmol) of **1-Tb** in 4 mL of THF. This suspension was stirred for 12 h, during which the suspended solids changed in color from pink-red to green. Solids of **2-Tb** were isolated by filtration, washed with 2 mL of THF, and dried for 15 m. The formula unit was determined by simultaneous fitting of C, H, N, and Na elemental analysis, in which Na content was obtained by inductively coupled plasma (ICP) analysis. Yield: 112.5 mg (100%). Anal. Calcd. for $C_{27.3}H_{26.9}N_{2.3}Na_{2.7}O_{14.9}Tb_2$ ($Na_{2.7}Tb_2(dbhq)_3(DMF)_{2.3}(THF)_{0.6}$): C, 32.61; H, 2.70; N, 3.20. Found: C, 32.47; H, 3.16; N, 3.09. ICP Calcd: Na, 6.17; Found: Na, 6.13.

Synthesis of $Na_{2.5}Dy_2(dbhq)_3(DMF)_{2.9}(THF)_{1.7}$ (2-Dy). A solution of the reducing agent sodium napthalenide was prepared by stirring 57.1 mg (0.446 mmol) of naphthalene in tetrahydrofuran over roughly 2-fold excess sodium for 3 h. The dark green sodium naphthalenide solution was then added to a stirring suspension of 175.0 mg (0.149 mmol) of **1-Dy** in 4 mL of THF. This suspension was stirred for 12 h, during which the suspended solids changed in color from pink-red to green. Solids of **2-Dy** were isolated by filtration, washed with 2 mL of THF, and dried for 15 m. The formula unit was determined by simultaneous fitting of C, H, N, and Na elemental analysis, in which Na content was obtained by inductively coupled plasma (ICP) analysis. Yield: 155.9 mg

(92.7%). Anal. Calcd. for $C_{33.5}H_{39.9}N_{2.9}Na_{2.5}O_{16.6}Dy_2$ ($Na_{2.5}Dy_2(dbhq)_3(DMF)_{2.9}(THF)_{1.7}$): C, 35.57; H, 3.56; N, 3.59. Found: C, 35.60; H, 3.40; N, 3.59. ICP Calcd: Na, 5.08; Found: Na, 5.18.

Synthesis of $Na_3Ho_2(dbhq)_3(DMF)_{2.9}(THF)_{1.4}$ (2-Ho). A solution of the reducing agent sodium napthalenide was prepared by stirring 59.0 mg (0.460 mmol) of naphthalene in tetrahydrofuran over roughly 2-fold excess sodium for 3 h. The dark green sodium naphthalenide solution was then added to a stirring suspension of 181.6 mg (0.154 mmol) of **1-Ho** in 4 mL of THF. This suspension was stirred for 12 h, during which the suspended solids changed in color from pink-red to green. Solids of **2-Ho** were isolated by filtration, washed with 2 mL of THF, and dried for 15 m. The formula unit was determined by simultaneous fitting of C, H, N, and Na elemental analysis, in which Na content was obtained by inductively coupled plasma (ICP) analysis. Yield: 160.4 mg (92.7%). Anal. Calcd. for $C_{32.3}H_{37.5}N_{2.9}Na_3O_{16.3}Ho_2$ ($Na_3Ho_2(dbhq)_3(DMF)_{2.9}(THF)_{1.4}$): C, 34.45; H, 3.36; N, 3.61. Found: C, 34.49; H, 3.25; N, 3.57. ICP Calcd: Na, 6.13; Found: Na, 6.13.

Synthesis of $Na_{2.7}Er_2(dbhq)_3(DMF)_{2.7}(THF)_{1.8}$ (2-Er). A solution of the reducing agent sodium napthalenide was prepared by stirring 64.2 mg (0.501 mmol) of naphthalene in tetrahydrofuran over roughly 2-fold excess sodium for 3 h. The dark green sodium naphthalenide solution was then added to a stirring suspension of 198.1 mg (0.167 mmol) of **1-Er** in 4 mL of THF. This suspension was stirred for 12 h, during which the suspended solids changed in color from pink-red to green. Solids of **2-Er** were isolated by filtration, washed with 2 mL of THF, and dried for 15 m. The formula unit was determined by simultaneous fitting of C, H, N, and Na elemental analysis, in which Na content was obtained by inductively coupled plasma (ICP) analysis. Yield: 172.9 mg (91.1%). Anal. Calcd. for $C_{33.3}H_{39.3}N_{2.7}Na_{2.7}O_{16.5}Er_2$ ($Na_{2.7}Er_2(dbhq)_3(DMF)_{2.7}(THF)_{1.8}$): C, 35.15; H, 3.48; N, 3.32. Found: C, 35.17; H, 3.23; N, 3.42. ICP Calcd: Na, 5.45; Found: Na, 5.44.

Synthesis of $Na_3Tm_2(dbhq)_3(DMF)_{2.5}(THF)_{1.3}$ (2-Tm). A solution of the reducing agent sodium napthalenide was prepared by stirring 33.7 mg (0.263 mmol) of naphthalene in tetrahydrofuran over roughly 2-fold excess sodium for 3 h. The dark green sodium naphthalenide solution was then added to a stirring suspension of 104.5 mg (0.088 mmol) of **1-Tm** in 4 mL of THF. This suspension was stirred for 12 h, during which the suspended solids changed in color from pink-red to green. Solids of **2-Tm** were isolated by filtration, washed with 2 mL of THF, and dried for 15 m. The formula unit was determined by simultaneous fitting of C, H, N, and Na elemental analysis, in which Na content was obtained by inductively coupled plasma (ICP) analysis. Yield: 85.4 mg (88.7%). Anal. Calcd. for $C_{30.7}H_{33.9}N_{2.5}Na_3O_{15.8}Tm_2$ ($Na_3Tm_2(dbhq)_3(DMF)_{2.5}(THF)_{1.3}$): C, 33.6; H, 3.11; N, 3.19. Found: C, 33.52; H, 3.06; N, 3.19. ICP Calcd: Na, 6.28; Found: Na, 6.40.

Synthesis of $Na_{2.2}Yb_2(dbhq)_3(DMF)_{2.4}(THF)_{1.2}$ (2-Yb). A solution of the reducing agent sodium napthalenide was prepared by stirring 65.1 mg (0.508 mmol) of naphthalene in tetrahydrofuran over roughly 2-fold excess sodium for 3 h. The dark green sodium naphthalenide solution was then added to a stirring suspension of 203.0 mg (0.169 mmol) of **1-Yb** in 4 mL of THF. This suspension was stirred for 12 h, during which the suspended solids changed in color from pink-red to green. Solids of **2-Yb** were isolated by filtration, washed with 2 mL of THF, and dried for 15 m. The formula unit was determined by simultaneous fitting of C, H, N, and Na elemental analysis, in which Na content was obtained by inductively coupled plasma (ICP) analysis. Yield: 175.0 mg

(96.3%). Anal. Calcd. for $C_{30}H_{32.4}N_{2.4}Na_{2.2}O_{15.6}Yb_2$ ($Na_{2.2}Yb_2(dbhq)_3(DMF)_{2.4}(THF)_{1.2}$): C, 33.59; H, 3.04; N, 3.13. Found: C, 33.32; H, 3.33; N, 3.08. ICP Calcd: Na, 4.71; Found: Na, 4.69.

Synthesis of $Na_{2.2}Y_2(dbhq)_3(DMF)_{26}(THF)_{0.8}$ (2-Y). A solution of the reducing agent sodium napthalenide was prepared by stirring 75.9 mg (0.592 mmol) of naphthalene in tetrahydrofuran over roughly 2-fold excess sodium for 3 h. The dark green sodium naphthalenide solution was then added to a stirring suspension of 0.2034 mg (0.197 mmol) of **1-Y** in 4 mL of THF. This suspension was stirred for 12 h, during which the suspended solids changed in color from pink-red to green. Solids of **2-Y** were isolated by filtration, washed with 2 mL of THF, and dried for 15 m. The formula unit was determined by simultaneous fitting of C, H, N, and Na elemental analysis, in which Na content was obtained by inductively coupled plasma (ICP) analysis. Yield: 187.1 mg (%). Anal. Calcd. for $C_{29}H_{30.6}N_{2.6}Na_{2.2}O_{15.4}Y_2$ ($Na_{2.2}Y_2(dbhq)_3(DMF)_{2.6}(THF)_{0.8}$): C, 39.12; H, 3.46; N, 4.09. Found: C, 39.10; H, 3.80; N, 4.08. ICP Calcd: Na, 5.68; Found: Na, 5.55.

Procedure for Metal Content Analysis via ICP-OES. About 15 mg of **2-Ln** were placed in a 20 mL borosilicate glass vial and digested with 5 mL 5% HNO_3 in Millipore water. This solution was then diluted to a total volume of 100 mL with 5% HNO_3 in Millipore water. An aliquot of 10 mL of this solution was separated, to which 1 mL of a 2.5 ppm ytrrium standard solution was added to act as an internal standard. This solution was then further diluted to a total volume of 25 mL with 5% HNO_3 in Millipore water. Standard solutions ranging from 0.1 to 15 ppm of Na, and each containing 0.1 ppm Y as an internal standard, were prepared for the calibration curve. ICP analysis of **2-Y** was performed without an internal standard due to the presence of yttrium in the material.

Single-Crystal X-Ray Diffraction. X-ray diffraction analysis was performed on single crystals coated with Paratone-N oil and mounted on a MiTeGen loops. The crystals were frozen at 100 K by an Oxford Cryosystems Cryostream 700 Plus. Data were collected at Beamline 12.2.1 at the Advanced Light Source at Lawrence Berkeley National Laboratory using synchrotron radiation (λ = 0.7288 Å) on a Bruker D8 diffractometer equipped with a Bruker PHOTON II CPAD detector. Raw data were integrated and corrected for Lorentz and polarization effects using Bruker AXS SAINT software.[1] Absorption corrections were applied using SADABS.[2] The structures were solved using intrinsic phasing with SHELXT[3,4] and refined using SHELXL[5,6] operated in the OLEX2[7] interface. No significant crystal decay was observed during data collection. Thermal parameters were refined anisotropically for all non-hydrogen atoms. Hydrogen atoms were placed in ideal positions and refined using a riding model for all structures. Frameworks that crystallized in the $P2_1/c$ spacegroup exhibited stacking disorder that could not be satisfactorily modelled. Consequently, framework ligands required the use of strong geometric and displacement parameter restrains. Residual electron density near the framework ligands and lanthanide centers triggered several level A and B alerts in checkCIF. Responses to these alerts can be found in the CIFs and checkCIF reports. Unassigned electron density in the voids of some structures results from disordered solvent that could not be modeled. The unassigned electron density was accounted for using SQUEEZE[8] as implemented in the PLATON[9] interface.

Powder X-Ray Diffraction. Powder X-ray diffraction patterns were collected at Beamline 12.2.2 at the Advanced Light Source using a wavelength of 0.4973 Å (25 keV). The wavelength was determined using a CeO_2 standard. Two-dimensional Debye-Scherrer diffraction rings from

powder measurements were collected on a MAR345 image plate detector and integrated using *Dioptas* software.[10]

Infrared Spectroscopy. Infrared spectra were collected on a Perkin Elmer Avatar Spectrum 400 FTIR spectrometer. Spectra of **1-Ln** were collected under ambient conditions, and due to the hydroscopic nature of **1-Ln**, exhibits the presence of some absorbed water. A homebuilt glovebag attachment was used to perform air-free measurements of **2-Ln** under a dinitrogen atmosphere.

NIR-UV-Visible Spectroscopy. UV-visible-NIR diffuse reflectance spectra were collected using a CARY 5000 spectrophotometer interfaced with Varian Win UV software. The samples of **2-Ln** were held in a Praying Mantis air-free diffuse reflectance cell. Spectroscopy of **1-Ln** was performed in ambient conditions, but the Praying Mantis diffuse reflectance cell cover was still used in order to minimize differences in background spectra of **1-Ln** and **2-Ln**. Barium sulfate powder was used as a non-adsorbing matrix. The Kubelka-Munk conversion (F(R) vs. wavenumber) of the raw diffuse reflectance spectrum (R vs. wavenumber) was obtained by applying the formula $F(R) = (1 - R)^2/2R$.

Magnetic Measurements. Samples of **2-Ln** were prepared by adding crystalline powder of **2-Ln** to a 5 mm inner diameter quartz tube containing a raised quartz platform. Solid eicosane was added to cover the sample to prevent crystallite torqueing and provide good thermal contact between the sample and the cryostat. The tubes were fitted with Teflon sealable adapters, evacuated on a Schlenk line, and flame-sealed under static vacuum. Following flame sealing, the solid eicosane was melted in a water bath held at 40 °C. Magnetic susceptibility measurements were performed using a Quantum Design MPMS2 SQUID magnetometer. Dc magnetic susceptibility measurements were collected in the temperature range 2–300 K under applied magnetic fields of 0.1 T. Diamagnetic corrections were applied to the data using Pascal's constants.

Table S3.1. Crystallographic data for **1-Sm**, **1-Eu**, **1-Gd**, **1-Tb**, and **1-Dy**.

	$Sm_2(dhbq)_3(DMF)_6\cdot 2DMF$	$Eu_2(dhbq)_3(DMF)_6\cdot 1.5DMF$	$Gd_2(dhbq)_3(DMF)_6\cdot 1.5DMF$	$Tb_2(dhbq)_3(DMF)_4\cdot 2DMF$	$Dy_2(dhbq)_3(DMF)_4\cdot 2DMF$
Formula	$C_{42}H_{62}N_8O_{20}Sm_2$	$C_{40.5}H_{58.5}N_{7.5}O_{19.5}Eu_2$	$C_{40.5}H_{58.5}N_{7.5}O_{19.5}Gd_2$	$C_{36}H_{48}N_6O_{18}Tb_2$	$C_{36}H_{48}N_6O_{18}Dy_2$
Temperature (K)	100(2)	100(2)	100(2)	100(2)	100(2)
Crystal System	Monoclinic	Monoclinic	Monoclinic	Monoclinic	Monoclinic
Space Group	$C2/c$	$C2/c$	$C2/c$	$P2_1/c$	$P2_1/c$
a, b, c (Å)	23.0022(10), 13.2773(6), 18.2784(8)	22.9448(10), 13.2482(6), 18.2511(8)	22.9371(6), 13.2424(3), 18.1988(5)	15.8310(5), 21.6125(8), 12.97924(5)	15.6111(6), 21.9355(9), 12.9149(5)
α, β, γ (°)	90, 114.768(2), 90	90, 114.779(2), 90	90, 114.8350(14), 90	90, 91.248(2), 90	90, 91.475(2), 90
V (Å^3)	5068.8(4)	5037.1(4)	5016.5(2)	4436.4(3)	4421.1(3)
Z	4	4	4	4	4
Radiation, λ (Å)	Synchrotron, 0.7288	Synchrotron, 0.7288	Synchrotron, 0.7288	Synchrotron, 0.7288	Synchrotron, 0.7288
2Θ Range for Data Collection (°)	3.728 to 69.41	3.736 to 69.414	3.738 to 56.476	2.638 to 62.740	2.676 to 58.136
Completeness to 2Θ	100.0% (2Θ = 51.860°)	99.9% (2Θ = 51.860°)	100.0% (2Θ = 51.860°)	100.0% (2Θ = 51.860°)	100.0% (2Θ = 51.860°)
Data / Restraints / Parameters	10148 / 21 / 286	10072 / 42 / 286	5745 / 21 / 286	13546 / 246 / 571	10967 / 126 / 571
Goodness of Fit on F^2	1.403	1.382	1.359	1.175	1.175
$R_1{}^a$, $wR_2{}^b$ ($I>2\sigma(I)$)	0.1008, 0.1945	0.1012, 0.2004	0.0949, 0.1818	0.0942, 0.2476	0.0995, 0.2307
$R_1{}^a$, $wR2^b$ (all data)	0.1144, 0.1996	0.1128, 0.2049	0.1084, 0.1866	0.1056, 0.2526	0.1092, 0.2349
Largest Diff. Peak and Hole (e Å^{-3})	1.770 and −2.434	1.595 and –2.276	1.430 and –1.332	9.537 and –8.637	7.563 and –8.520

$^aR_1 = \sum||F_o| - |F_c||/\sum|F_o|$. $^bwR_2 = \{\sum[w(F_o^2 - F_c^2)^2]/\sum[w(F_o^2)^2]\}^{1/2}$

Table S3.2. Crystallographic data for **1-Ho**, **1-Er**, **1-Tm**, and **1-Yb**.

	$Ho_2(dhbq)_3(DMF)_4 \cdot 2DMF$	$Er_2(dhbq)_3(DMF)_4 \cdot 2DMF$	$Tm_2(dhbq)_3(DMF)_4 \cdot 2DMF$	$Yb_2(dhbq)_3(DMF)_4 \cdot 2DMF$
Formula	$C_{36}H_{48}N_6O_{18}Ho_2$	$C_{36}H_{48}N_6O_{18}Er_2$	$C_{36}H_{48}N_6O_{18}Tm_2$	$C_{36}H_{48}N_6O_{18}Yb_2$
Temperature (K)	100(2)	100(2)	100(2)	100(2)
Crystal System	Monoclinic	Monoclinic	Monoclinic	Monoclinic
Space Group	$P2_1/c$	$P2_1/c$	$P2_1/c$	$P2_1/c$
a, b, c (Å)	15.5431(7), 21.9774(11), 12.9073(6)	15.5200(5), 21.8478(7), 12.9213(4)	15.5434(6), 21.7317(10), 12.9262(5)	15.4935(7), 21.7088(11), 12.9479(6)
α, β, γ (°)	90, 91.714(2), 90	90, 91.6877(19), 90	90, 91.675(2), 90	90, 91.899(3), 90
V (Å^3)	4407.1(4)	4379.4(2)	4364.4(3)	4352.6(4)
Z	4	4	4	4
Radiation, λ (Å)	Synchrotron, 0.7288	Synchrotron, 0.7288	Synchrotron, 0.7288	Synchrotron, 0.7288
2Θ Range for Data Collection (°)	2.688 to 63.756	2.692 to 52.082	2.688 to 54.190	2.696 to 58.130
Completeness to 2Θ	100.0% (2Θ = 51.860°)	100.0% (2Θ = 51.860°)	100.0% (2Θ = 51.860°)	99.8% (2Θ = 51.860°)
Data / Restraints / Parameters	14051 / 0 / 571	8022 / 93 / 571	8935 / 141 / 571	10787 / 291 / 571
Goodness of Fit on F^2	1.098	1.092	1.125	1.089
R_1[a], wR_2[b] ($I>2\sigma(I)$)	0.0356, 0.0684	0.0531, 0.1233	0.1197, 0.2823	0.1373, 0.3523
R_1[a], $wR2$[b] (all data)	0.0513, 0.0729	0.0696, 0.1295	0.1347, 0.2890	0.1498, 0.3585
Largest Diff. Peak and Hole (e Å^{-3})	1.152 and –2.170	3.970 and –3.444	11.701 and –10.712	13.511 and –15.210

[a] $R_1 = \sum||F_o| - |F_c||/\sum|F_o|$. [b] $wR_2 = \{\sum[w(F_o^2 - F_c^2)^2]/\sum[w(F_o^2)^2]\}^{1/2}$.

Attempted Chemical Reduction of 1-Gd:

Synthesis of 1-Gd-reduction conditions. A solution of the reducing agent sodium napthalenide was prepared by stirring 44.9 mg (0.350 mmol) of naphthalene in tetrahydrofuran over roughly 2-fold excess sodium for 3 h. The dark green sodium naphthalenide solution was then added to a stirring suspension of 136.5 mg (0.117 mmol) of **1-Gd** in 4 mL of THF. This suspension was stirred for 12 h, during which the suspended solids changed in color from pink-red to green. Solids of **1-Gd-reduction conditions** were isolated by filtration, washed with 2 mL of THF, and dried for 15 m. The formula unit was determined by simultaneous fitting of C, H, N, and Na elemental analysis, in which Na content was obtained by inductively coupled plasma (ICP) analysis. Yield: 117.2 mg (94.5%). Anal. Calcd. for $C_{30.2}H_{33}N_{2.6}Na_{2.7}O_{15.7}Gd_2$ ($Na_{2.7}Gd_2(dbhq)_3(DMF)_{2.6}(THF)_{1.1}$): C, 34.21; H, 3.14; N, 3.44. Found: C, 34.27; H, 3.02; N, 3.43. ICP Calcd: Na, 5.85; Found: Na, 5.84. **1-Gd-reduction conditions** was amorphous and did not exhibit differences in magnetic behavior, compared to **1-Gd**, that were substantial enough to suggest bulk chemical reduction.

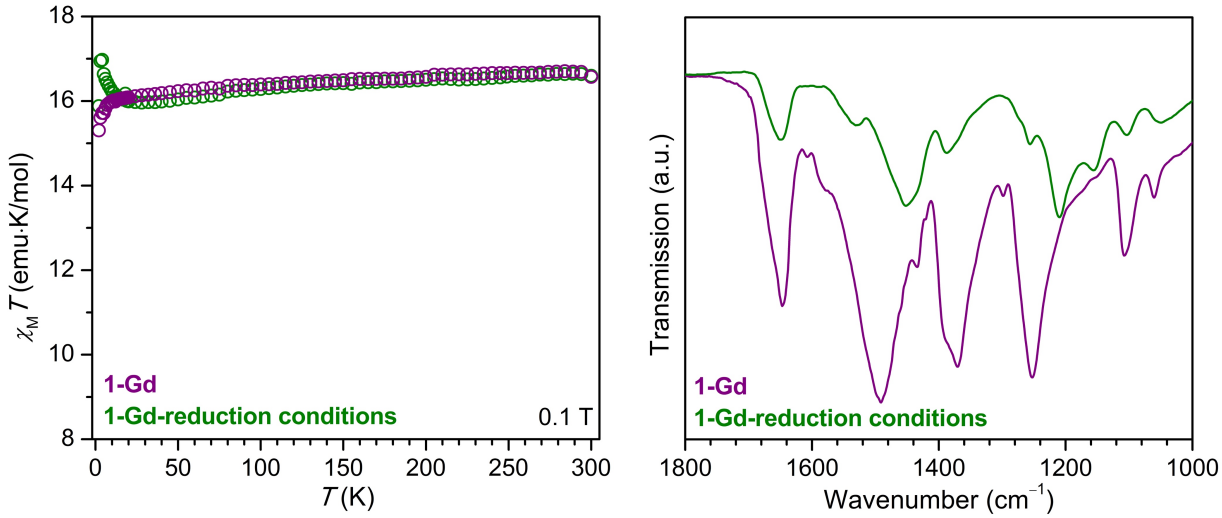

Figure S3.1. Left: Magnetic susceptibility times temperature product ($\chi_M T$) versus temperature for the materials **1-Gd** and **1-Gd-reduction conditions**, collected under an applied magnetic field of 0.1 T. Right: IR spectra zoomed in on the region of interest for **1-Gd** and **1-Gd-reduction conditions**, represented by purple and green lines, respectively.

Powder X-Ray Diffraction:

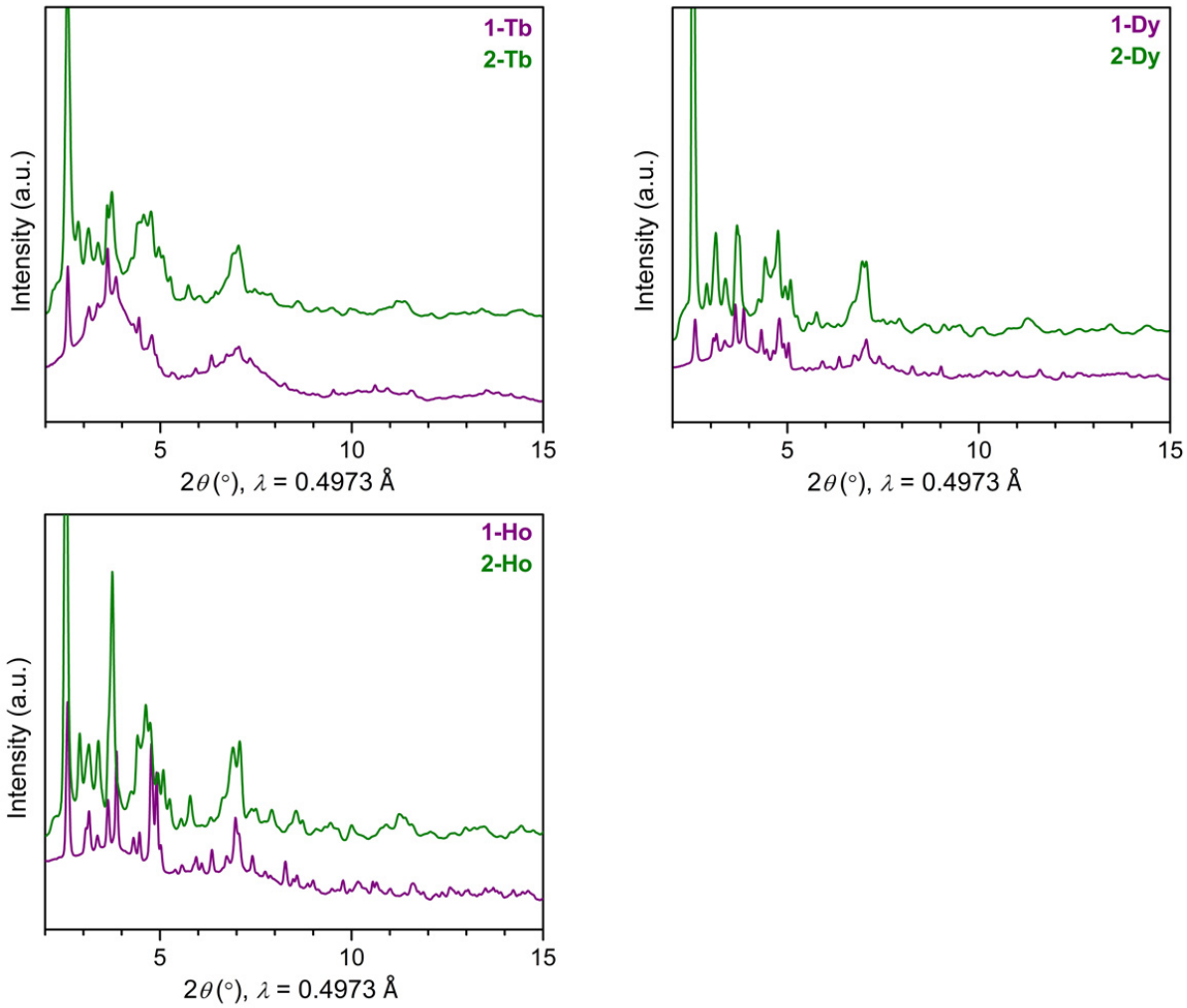

Figure S3.2. Powder X-ray diffraction patterns for **1-Tb** and **2-Tb**, **1-Dy** and **2-Dy**, and **1-Ho** and **2-Ho**, where **1-Ln** and **2-Ln** are represented by purple and green lines, respectively.

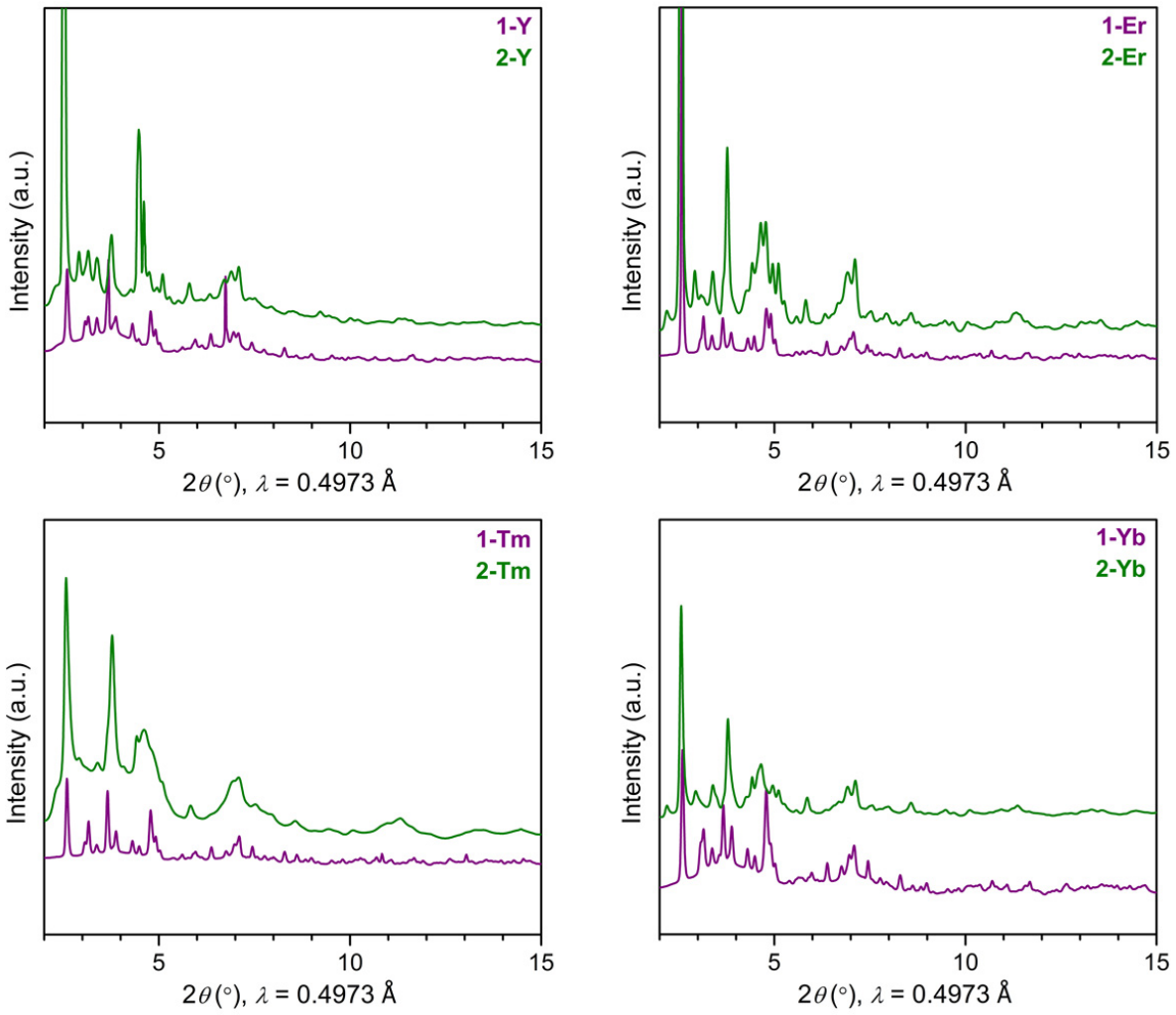

Figure S3.3 Powder X-ray diffraction patterns for **1-Y** and **2-Y**, **1-Er** and **2-Er**, **1-Tm** and **2-Tm**, and **1-Yb** and **2-Yb**, where **1-Ln** and **2-Ln** are represented by purple and green lines, respectively.

Infrared Spectroscopy:

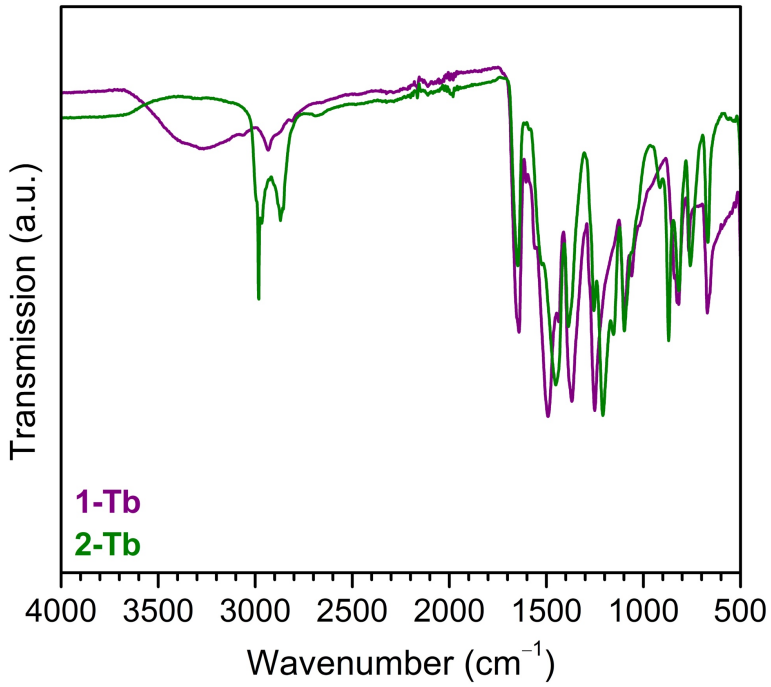

Figure S3.4. Full IR spectrum for **1-Tb** and **2-Tb**, shown by purple and green lines, respectively. Changes to the IR spectra between the **1-Ln** and **2-Ln** series are consistent across all lanthanides Ln = Y, Sm–Yb. The intense peaks between 3000 and 2850 cm^{-1} for **2-Tb** reflect C-H stretching modes of THF, which was used to clean the sample stage in between samples. Since the **2-Tb** spectra were collected in a home-built nitrogen glovebag setup, it was not possible to fully purge the atmosphere of THF solvent vapor.

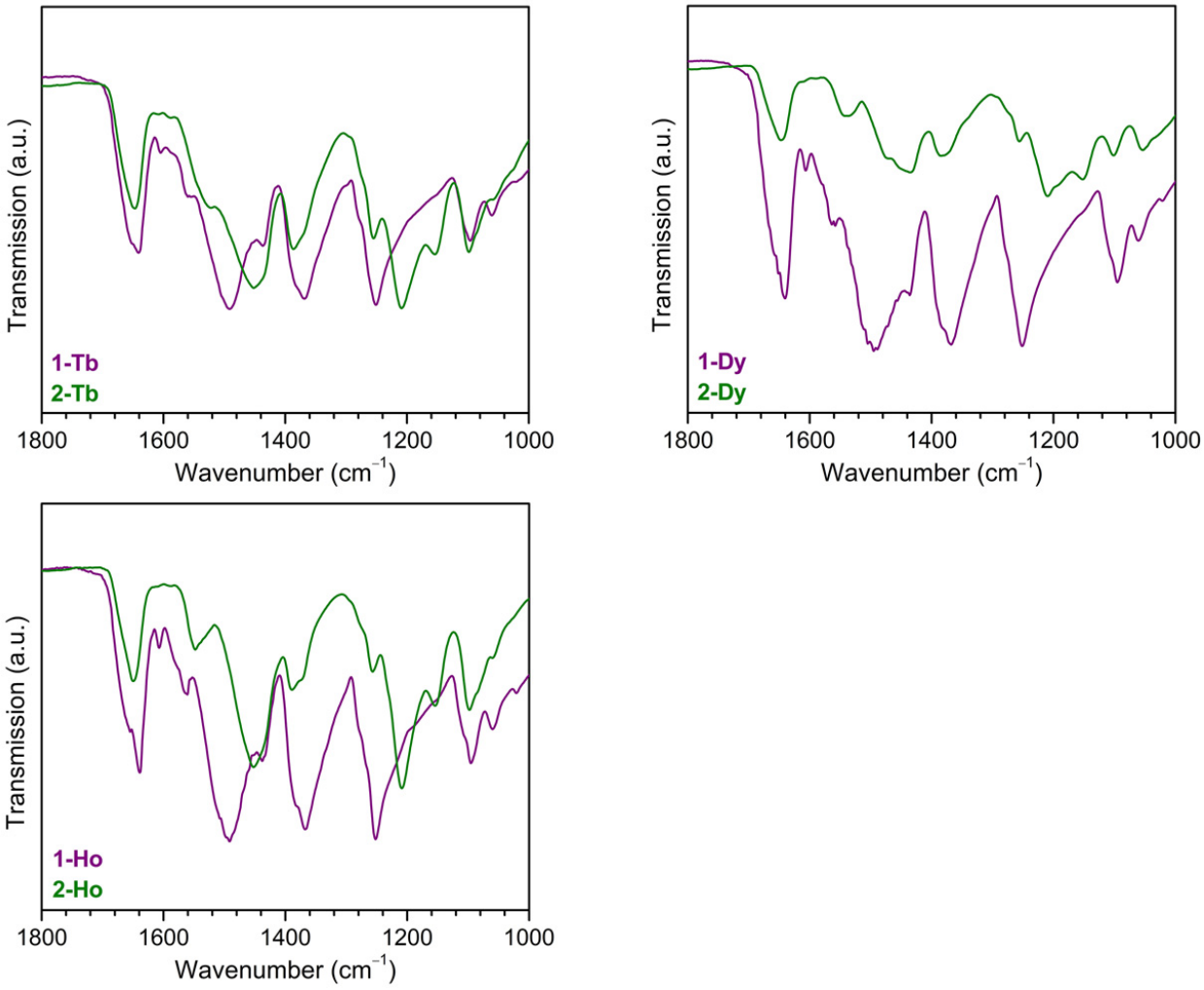

Figure S3.5. IR spectra zoomed in on the region of interest for **1-Tb** and **2-Tb**, **1-Dy** and **2-Dy**, and **1-Ho** and **2-Ho**, where **1-Ln** and **2-Ln** are represented by purple and green lines, respectively.

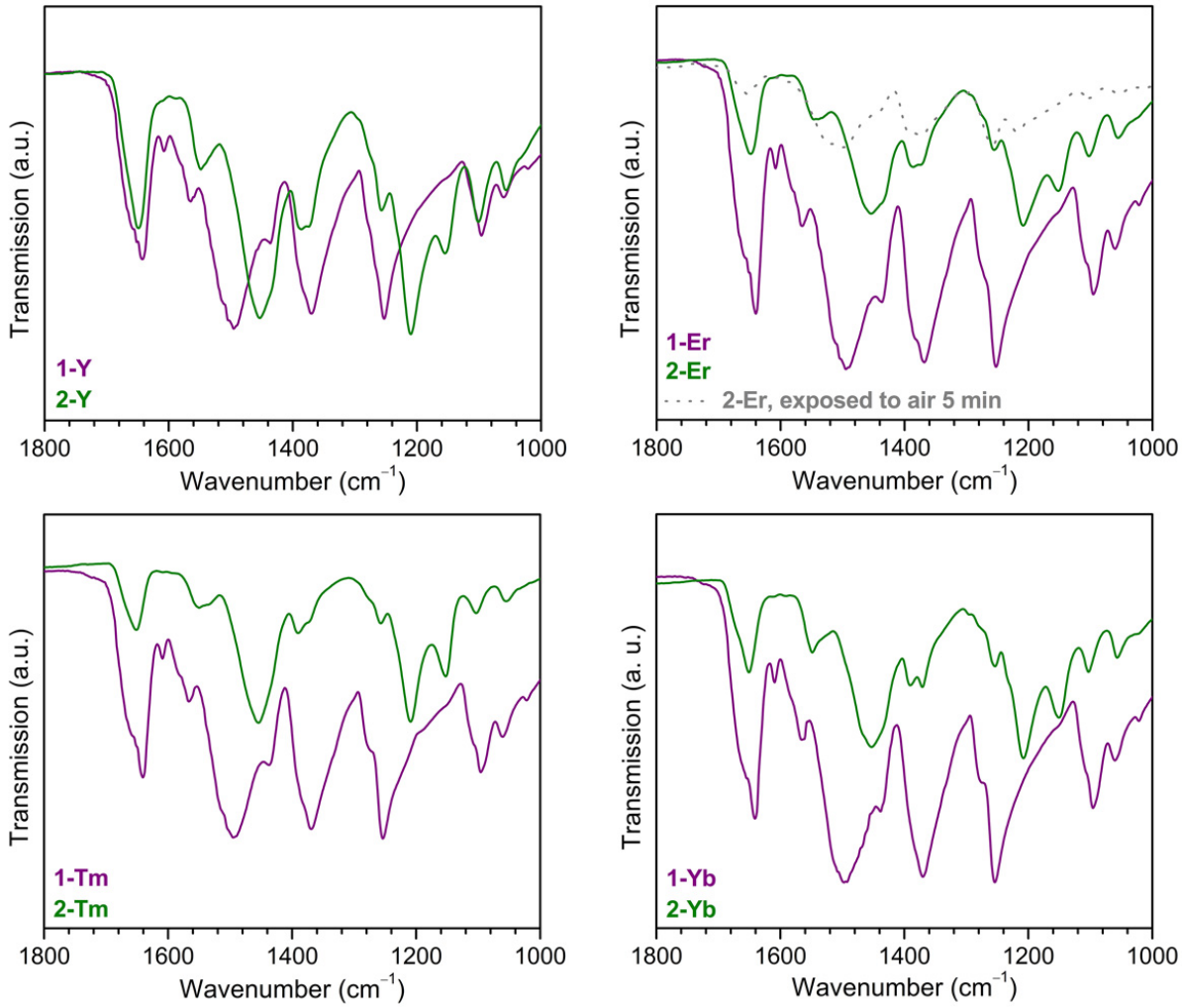

Figure S3.6. IR spectra zoomed in on the region of interest for **1-Y** and **2-Y**, **1-Er** and **2-Er**, **1-Tm** and **2-Tm**, and **1-Yb** and **2-Yb**, where **1-Ln** and **2-Ln** are represented by purple and green lines, respectively. The grey dotted line represents a sample of **2-Er** exposed to air for 5 minutes, and exhibits the return of the carbonyl stretch to its value in **1-Er**, as the ligand is oxidized back to dhbq^{2-}.

Magnetic Measurements:

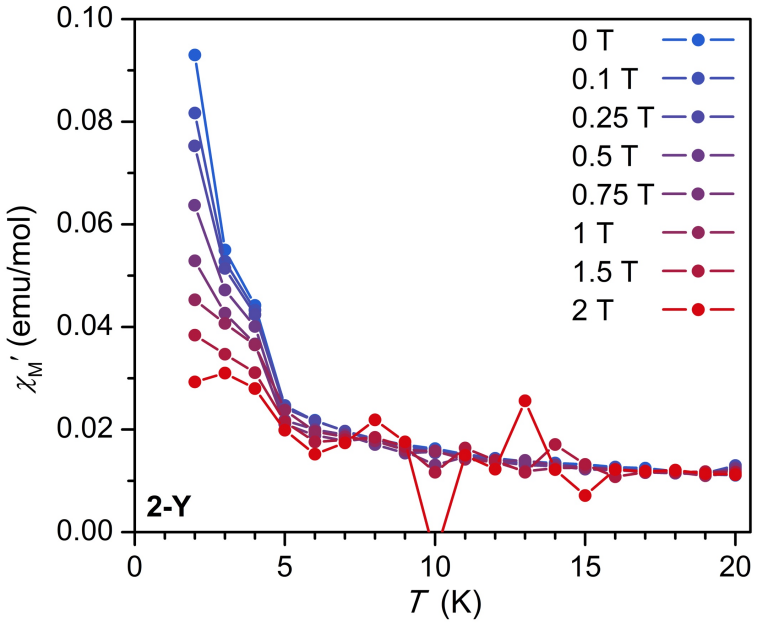

Figure S3.7. In-phase ac magnetic susceptibility measurements of **2-Y** collected under applied magnetic field strengths ranging from 0 to 2 T, with a frequency of 100 Hz and an oscillating ac field of 4 Oe. No out-of-phase ac signal was observed for **2-Y**.

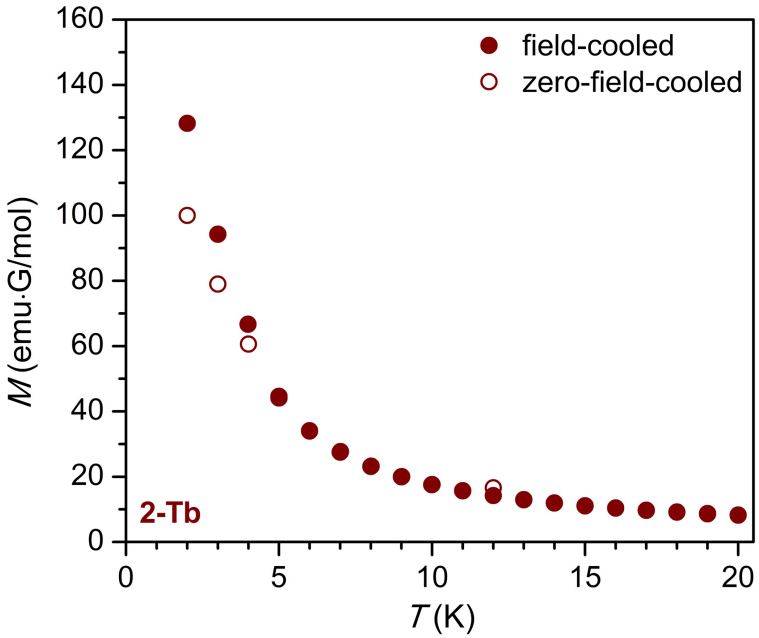

Figure S3.8. Zero-field-cooled and field-cooled magnetization measurements of **2-Tb**, showing a divergence at 4 K.

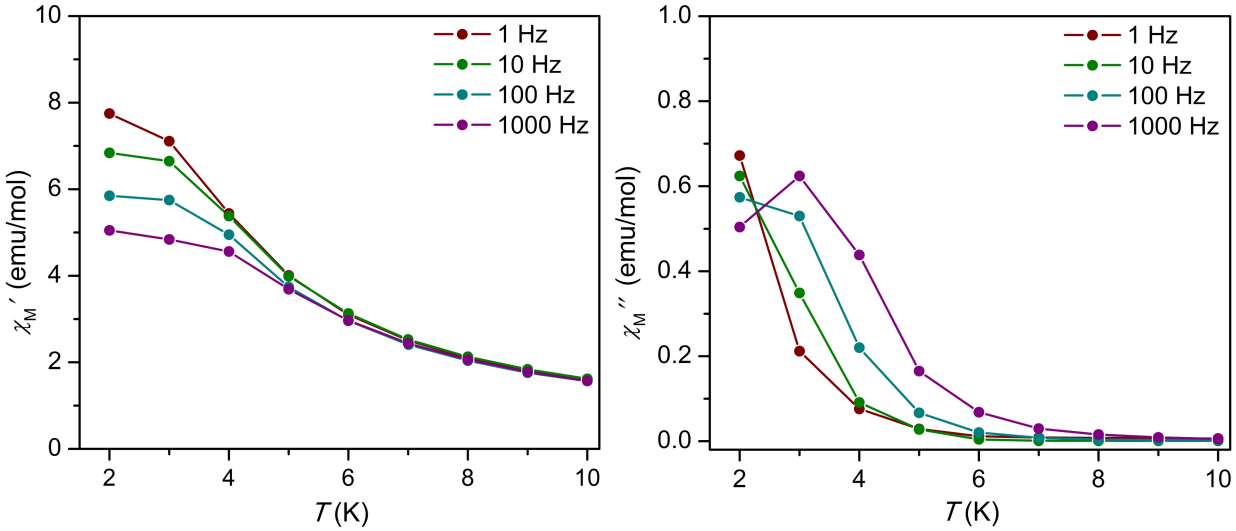

Figure S3.9. Ac magnetic susceptibility measurements of **2-Tb** collected under zero applied magnetic field using frequencies ranging from 1 – 1000 Hz, with an oscillating ac field of 4 Oe.

S3.2 References for Chapter 3 Supporting Information

1) Bruker Analytical X-ray Systems, Inc. *SAINT and APEX 2 Software for CCD Diffractometers*; Bruker Analytical X-ray Systems, Inc.: Madison, WI, 2000.
2) Sheldrick, G. M. SADABS; Bruker Analytical X-ray Systems, Inc.: Madison, WI, 2014.
3) G. M. Sheldrick, *SHELXS* (University of Göttingen, Germany, 2014).
4) G. M. Sheldrick, A short history of SHELX. *Acta Crystallogr., A, Found. Crystallogr.* **64**, 112–122 (2008).
5) Sheldrick, G. M. *Acta Crystallogr., Sect. A: Found. Crystallogr.* **2008**, *64*, 112−122.
6) Sheldrick, G. M. *SHELXL*; University of Göttingen: Germany, 2014.
7) Dolomanov, O. V.; Bourhis, L. J.; Gildea, R. J.; Howard, J. A. K.; Puschmann, H. *J. Appl. Crystallogr.* **2009**, *42*, 339−341.
8) A. L. Spek, PLATON SQUEEZE: a tool for the calculation of the disordered solvent contribution to the calculated structure factors. *Acta Crystallogr C Struct Chem*. **2015**, *71*, 9–18.
9) A. L. Spek, Single-crystal structure validation with the program PLATON. *Journal of Applied Crystallography*. **2003**, *36*, 7–13.
10) Prescher, C.; Prakapenka, V. B. DIOPTAS: a Program for Reduction of Two-Dimensional X-Ray Diffraction Data and Data Exploration. *High Press. Res.* **2015**, *35*, 223–230.

Chapter 4: Strong Ferromagnetic Exchange Coupling and Single-Molecule Magnetism in MoS_4^{3-}-Bridged Dilanthanide Complexes

4.1 Introduction

Single-molecule magnets, discrete molecules that exhibit a well-isolated bistable magnetic ground state with a thermal barrier to relaxation of the magnetization, *U,* are of potential utility in high-density information storage and quantum information processing.[1] However, to date even the most promising systems are limited by low operating temperatures, with upper limits defined by the blocking temperature, T_b, of a given molecule. Below this temperature the magnetization remains pinned along the molecular magnetic easy axis and is not susceptible to thermal fluctuations, akin to the magnetic polarization within bulk magnetic materials. One particularly successful strategy for generating single-molecule magnets with high blocking temperatures has been through the design of systems exhibiting strong magnetic exchange interactions between highly anisotropic lanthanide ions, perhaps best illustrated by the diterbium(III) complex $\{[((Me_3Si)_2N)_2Ln(THF)]_2(\mu\text{-}N_2^{\bullet})\}^{1-}$.[2] In this system, the diffuse spin orbital of the N_2^{3-} radical bridge is able to penetrate the core 4f magnetic orbitals to engender strong lanthanide-radical exchange coupling, resulting in a highly anisotropic molecular species with a 100-s magnetic blocking temperature of 14 K, one of the highest known values for an exchange-coupled system. A blocking temperature of 20 K was subsequently observed for the related N_2^{3-}-bridged complex, $\{[(C_5Me_4H)_2Tb]_2(\mu\text{-}N_2^{\bullet})\}^{1-}$,[3] and in this and other exchange-coupled complexes the barrier to magnetic relaxation, which tracks to some extent with T_b, has been shown to be a function of the magnitude of the magnetic exchange coupling.[3,4] While recent efforts to enhance crystal field splitting and axiality of magnetic excited states in single-ion lanthanide magnets has led to outstanding advances in 100-s magnetic blocking temperatures, up to 53 K,[5] the combination of large magnetic anisotropy and large total angular momentum achieved via strong exchange between lanthanides remains a promising route to still higher blocking temperatures.

Radical-bridged lanthanide complexes offer the advantage of ligands with spin-carrying atoms directly ligated to the lanthanide ion and thereby close enough to engage in direct exchange with the lanthanide spin density. In contrast, magnetic interactions of lanthanides with other metal ions have to date proceeded via superexchange pathways across ligand atoms. So, while lanthanide-transition metal pairings offer many additional synthetic handles with which to design exchange-coupled single-molecule magnets, *n*d-4f single-molecule magnets typically exhibit very weak magnetic coupling, in most cases less than 5 cm^{-1}.[6] This weak coupling in turn leads to slow magnetic relaxation that is single-ion in origin or prompts low-lying exchange-coupled excited states that preclude large relaxation barriers.[4,6,9b,9c]

The heavier 4d and 5d transition metals have the potential to facilitate strong superexchange with the lanthanides since their more diffuse d orbitals are more likely to have enhanced overlap with ligand orbitals.[7] Furthermore, there is better energy matching of 4d/5d spin-containing orbitals with the spin-carrying 4f and empty 5d lanthanide orbitals as compared to 3d transition metals. Nearly all lanthanide coordination compounds that incorporate 4d and 5d paramagnetic metal ions (M) utilize cyanide-ligated building units,[8] and all[8,9] of these compounds have yet to yield M–Gd coupling magnitudes of greater than 1.6 cm^{-1}.[8c,8i]

Considering candidate 4d bridging moieties with the potential for enhanced exchange strength, we turned to the MoS_4^{y-} ($y = 2, 3$) unit. The range of oxidation states available to molybdenum and the polarizability of the single-atom sulfide bridges render this moiety a promising ligand to facilitate magnetic communication. Herein, we report the synthesis and characterization of the MoS_4^{3-}-bridged complex salts $[Co(C_5Me_5)_2][(C_5Me_5)_2Ln(\mu\text{-}S)_2Mo(\mu\text{-}S)_2Ln(C_5Me_5)_2]$, **1-Ln**, accessed via one-electron reduction of the neutral Mo^{VI}-bridged complexes $(C_5Me_5)_2Ln(\mu$-

$S)_2Mo(\mu\text{-}S)_2Ln(C_5Me_5)_2$. Static magnetic susceptibility measurements reveal strong 4f/5d-4d ferromagnetic exchange coupling, which is proposed to occur via charge transfer from Mo^V to Ln^{III}, as supported by electron paramagnetic resonance and NIR-Uv-Vis spectroscopies. Moreover, slow magnetic relaxation behaviors are observed for **1-Tb** and **1-Dy**.

4.2 Experimental Information

General Information. All manipulations and syntheses described were conducted with rigorous exclusion of air and water using standard Schlenk line and glovebox techniques under an argon or nitrogen atmosphere. Solvents were sparged with UHP argon (Praxair) and dried by passage through columns containing Q-5 and molecular sieves prior to use. NMR solvents (Cambridge Isotope Laboratories) were dried over NaK alloy, degassed by three freeze-pump-thaw cycles, and vacuum transferred before use. Reagents $Co(C_5Me_5)_2$ (Aldrich) and $(NH_4)_2MS_4$ (M = Mo, W; Aldrich), were used as received. The lanthanide trichlorides $LnCl_3$ (Ln = Y, Gd, Tb, Dy) were dried according to literature procedures by heating a mixture of the hydrated trichloride with an excess of NH_4Cl.[10] Potassium bis(trimethylsilylamide) ($K[N(SiMe_3)_2]$, Aldrich, 95%) was purified via toluene extraction before use. Pentamethylcyclopentadiene, (C_5Me_5H, Aldrich, 95%) was dried over molecular sieves and degassed using three freeze-pump-thaw cycles before deprotonation with $K[N(SiMe_3)_2]$ to form the ligand KC_5Me_5.[11] The precursor compounds $(C_5Me_5)_2Y(C_3H_5)$,[12] $(C_5Me_5)_2Ln(\mu\text{-}Ph)_2BPh_2$[13] (Ln = Y, Gd, Tb, Dy), and $(PPh_4)_2MoS_4$[14] were prepared using literature procedures. Proton NMR spectra were recorded on Bruker GN500 or CRYO500 MHz spectrometers ($^{13}C\{^1H\}$ at 125 MHz) at 298 K, unless otherwise stated, and referenced internally to residual protio-solvent resonances. Samples for IR spectroscopic analysis were prepared as KBr pellets and spectra were obtained on a Jasco FT/IR-4700 or Varian 1000 spectrometer; EPR spectra were collected using X-band frequency (9.3–9.8 GHz) on a Bruker EMX Spectrometer equipped with an ER041XG microwave bridge, and the magnetic field was calibrated with DPPH (g = 2.0036). UV-visible-NIR diffuse reflectance spectra were collected using a CARY 5000 spectrophotometer interfaced with Varian Win UV software. The samples were held in a Praying Mantis air-free diffuse reflectance cell. Barium sulfate powder was used as a non-adsorbing matrix. The Kubelka-Munk conversion (F(R) vs. wavenumber) of the raw diffuse reflectance spectrum (R vs. wavenumber) was obtained by applying the formula $F(R) = (1 - R)2/2R$. Elemental analyses were conducted on a Perkin-Elmer 2400 Series II CHNS elemental analyzer.

$(C_5Me_5)_2Y(\mu\text{-}S)_2Mo(\mu\text{-}S)_2Y(C_5Me_5)_2$. A slurry of $(PPh_4)_2MoS_4$ (0.043 g, 0.048 mmol) in 3 mL of THF was added to a solution of $(C_5Me_5)_2Y(\mu\text{-}Ph)_2BPh_2$ (0.066 g, 0.097 mmol) in 2 mL of THF. The solution immediately became dark brown/purple and cloudy. After stirring for 1 h, the mixture was centrifuged to produce a purple supernatant and dark grey insoluble material. The supernatant was collected by filtration and the THF solvent was removed under reduced pressure to yield a dark brown/purple solid. The brown/purple solid was dissolved in toluene (5 mL) and cooled overnight at −35 °C to yield dark purple crystals (0.018 g, 43%) suitable for X-ray diffraction, which enabled identification of the compound as Mo^{VI}-bridged $(C_5Me_5)_2Y(\mu\text{-}S)_2Mo(\mu\text{-}S)_2Y(C_5Me_5)_2$. ^1H NMR (C_6D_6): δ 2.09 (s, $C_5\mathit{Me}_5$, 60H). $^{13}C\{^1H\}$ NMR 128.4 (C_5Me_5), 12.2 ($C_5\mathit{Me}_5$). IR (cm^{-1}): 2960m, 2900s, 2850s, 2720w, 1960w, 1440m, 1380m, 1020m, 800w, 730m, 700w, 490s. Anal Calcd for $C_{40}H_{60}S_4Y_2Mo$: C, 50.97; H, 6.42. Found: C, 50.69; H, 6.52.

$(C_5Me_5)_2Gd(\mu\text{-}S)_2Mo(\mu\text{-}S)_2Gd(C_5Me_5)_2\cdot C_4H_8O$. This compound was prepared as described: $(PPh_4)_2MoS_4$ (0.120 g, 0.133 mmol) and $(C_5Me_5)_2Gd(\mu\text{-}Ph)_2BPh_2$ (0.203 g, 0.272 mmol) were combined to yield dark purple solids of $(C_5Me_5)_2Gd(\mu\text{-}S)_2Mo(\mu\text{-}S)_2Gd(C_5Me_5)_2$ (0.120 g, 83%).

Crystals suitable for X-ray diffraction were grown from a concentrated toluene solution stored at −35 °C overnight. IR (cm^{-1}): 2901s, 2855s, 1591w, 1494m, 1433m, 1378m, 1189s, 1022w, 732m, 698m, 493s, 469m. Multiple elemental analyses are consistent with the inclusion of a THF molecule. Anal Calcd for $C_{40}H_{60}S_4Gd_2Mo \cdot C_4H_8O$: C, 45.89; H, 5.95. Found: C, 45.96; H, 5.96.

$(C_5Me_5)_2Tb(\mu\text{-}S)_2Mo(\mu\text{-}S)_2Tb(C_5Me_5)_2$. This compound was prepared as described above for $(C_5Me_5)_2Y(\mu\text{-}S)_2Mo(\mu\text{-}S)_2Y(C_5Me_5)_2$: $(PPh_4)_2MoS_4$ (0.135 g, 0.150 mmol) and $(C_5Me_5)_2Tb(\mu\text{-}Ph)_2BPh_2$ (0.230 g, 0.307 mmol) were combined to yield the product as a purple powder (0.089 g, 55%). Crystals suitable for X-ray diffraction were grown from a concentrated toluene solution stored at −35 °C overnight. IR (cm^{-1}): 2963s, 2900s, 2855s, 2725w, 2360m, 2341m, 2244m 2056w, 1435m, 1378m, 1022m, 732m, 489s, 478s, 434m. Anal Calcd for $C_{40}H_{60}S_4Tb_2Mo$: C, 44.36; H, 5.58. Found: C, 44.51; H, 5.58.

$(C_5Me_5)_2Dy(\mu\text{-}S)_2Mo(\mu\text{-}S)_2Dy(C_5Me_5)_2$. This compound was prepared as described above for $(C_5Me_5)_2Y(\mu\text{-}S)_2Mo(\mu\text{-}S)_2Y(C_5Me_5)_2$: $(PPh_4)_2MoS_4$ (0.142 g, 0.157 mmol) and $(C_5Me_5)_2Dy(\mu\text{-}Ph)_2BPh_2$ (0.243 g, 0.323 mmol) were combined to yield the product as a purple/brown powder (0.115 g, 67%). Crystals suitable for X-ray diffraction were grown from a concentrated toluene solution stored at −35 °C overnight. IR (cm^{-1}): 2963s, 2901s, 2854s, 2724w, 1434m, 1431m, 1378m, 1022m, 733m. Anal Calcd for $C_{40}H_{60}S_4Dy_2Mo$: C, 44.07; H, 5.55. Found: C, 44.36; H, 5.41.

$[Co(C_5Me_5)_2][(C_5Me_5)_2Y(\mu\text{-}S)_2Mo(\mu\text{-}S)_2Y(C_5Me_5)_2]$, 1-Y. To a stirred solution of $(C_5Me_5)_2Y(\mu\text{-}S)_2Mo(\mu\text{-}S)_2Y(C_5Me_5)_2$ (0.082 g, 0.087 mmol) in 6 mL of THF was added $Co(C_5Me_5)_2$ (0.027 g, 0.082 mmol) in 4 mL of THF. The solution changed from purple to red immediately. After 1 h, the solvent was removed under reduced pressure to produce a red solid. The solid was washed with toluene (3 × 2 mL) and dried under reduced pressure to yield the product as a red solid (0.077 g, 74%). Recrystallization of this solid from concentrated THF solutions at −35 °C overnight afforded red block-shaped crystals suitable for X-ray diffraction. ^1H NMR (THF-d_8): δ 2.38 (s, br, 60H, C_5Me_5), 2.26 (s, br, 30H, $Co(C_5Me_5)_2$). IR (cm^{-1}): 2957s, 2892s, 2851s, 2719w, 1475m, 1446m, 1427m, 1376m, 1259w, 1065m, 1022m. Anal Calcd for $C_{60}H_{90}S_4Y_2CoMo$: C, 56.64; H, 7.13. Found: C, 56.42; H, 7.19.

$[Co(C_5Me_5)_2][(C_5Me_5)_2Gd(\mu\text{-}S)_2Mo(\mu\text{-}S)_2Gd(C_5Me_5)_2]$, 1-Gd. This compound was prepared as described above for **1-Y**. $(C_5Me_5)_2Gd(\mu\text{-}S)_2Mo(\mu\text{-}S)_2Gd(C_5Me_5)_2$ (0.120 g, 0.111 mmol) and $Co(C_5Me_5)_2$ (0.0350 g, 0.106 mmol) were combined in THF to yield a red solution. The THF was removed from this solution under reduced pressure to yield a red powder. Recrystallization from concentrated THF solutions at −35 °C overnight gave the product as red block-shaped crystals (0.087 g, 58%) suitable for X-ray diffraction. IR (cm^{-1}): 2962m, 2888s, 2851s, 2721w, 1476m, 1450m, 1432m, 1388m, 1377m, 1066w, 1023m. Anal Calcd for $C_{60}H_{90}S_4Gd_2CoMo$: C, 51.15; H, 6.44. Found: C, 49.86; H, 6.32. Low carbon and hydrogen values were obtained even after multiple analysis attempts using different batches of samples. Found H/C ratios support an empirical formula having $C_{60}H_{90}$, so incomplete combustion of the EA sample likely occurred.

$[Co(C_5Me_5)_2][(C_5Me_5)_2Tb(\mu\text{-}S)_2Mo(\mu\text{-}S)_2Tb(C_5Me_5)_2]$, 1-Tb. This compound was prepared as described above for **1-Y**. $(C_5Me_5)_2Tb(\mu\text{-}S)_2Mo(\mu\text{-}S)_2Tb(C_5Me_5)_2$ (0.089 g, 0.084 mmol) and $Co(C_5Me_5)_2$ (0.026 g, 0.079 mmol) were combined in THF to yield a red solution. The THF was removed from this solution under reduced pressure to yield a red powder. Recrystallization from concentrated THF solutions at −35 °C overnight afforded the product as red block-shaped crystals (0.041 g, 37%) suitable for X-ray diffraction. IR (cm^{-1}): 2961m, 2889s, 2851s, 2718w, 1476m, 1449m, 1428m, 1385s, 1377s, 1066m, 1024m. Anal Calcd for $C_{64}H_{98}S_4OTb_2CoMo$: C, 51.78; H, 6.65. Found: C, 52.05; H, 6.42.

[Co(C_5Me_5)$_2$][(C_5Me_5)$_2$Dy(μ-S)$_2$Mo(μ-S)$_2$Dy(C_5Me_5)$_2$], 1-Dy. This compound was prepared as described above for **1-Y**. (C_5Me_5)$_2$Dy(μ-S)$_2$Mo(μ-S)$_2$Dy(C_5Me_5)$_2$ (0.119 g, 0.109 mmol) and Co(C_5Me_5)$_2$ (0.037 g, 0.112 mmol) were combined in THF to yield a red solution. The THF was removed from this solution under reduced pressure to yield a red powder. Recrystallization from concentrated THF solutions at −35 °C overnight afforded the product as red block-shaped crystals (0.055 g, 35%) suitable for X-ray diffraction. IR (cm^{-1}): 3372w, 2960s, 2889s, 2852s, 2722m, 2361m, 2344m, 1475m, 1447m, 1428m, 1377m, 1024m, 732m, 434s. Anal Calcd for $C_{64}H_{98}S_4ODy_2CoMo$: C, 51.53; H, 6.62. Found: C, 51.49; H, 6.79.

Scheme 4.1. Synthetic scheme for (C_5Me_5)$_2$Ln(μ-S)$_2$Mo(μ-S)$_2$Ln(C_5Me_5)$_2$and **1**-Ln (Ln = Y, Gd, Tb, Dy).

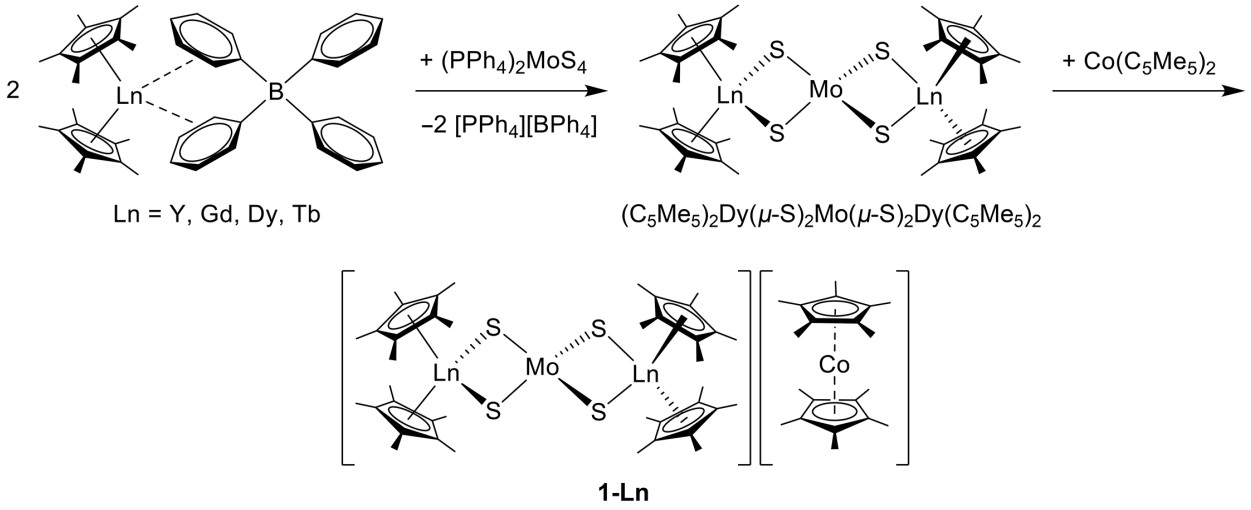

4.3 Results and Discussion

The tetrathiomolybdate unit, MoS_4^{n-}, has previously been shown to bridge multiple metal centers in transition metal complexes containing Cu,[15] Fe,[16] and Nb,[17] which have primarily found interest in nonlinear optics and as models for the Fe-Mo cofactor in nitrogenase. The compound (PPh$_4$)[(C_5Me_5)$_2$Sm(μ-S)$_2$Mo(μ-S)$_2$Sm(C_5Me_5)$_2$], containing an S = ½ MoS_4^{3-} unit bridging two Sm^{III} centers, has also been previously synthesized, demonstrating the ability of a MoS_4^{n-} unit to bridge two lanthanide(III) centers.[18] Since the later lanthanides are known to facilitate magnetic exchange and slow magnetic relaxation via their large magnetic moments and magnetic anisotropies, analogues with Gd, Tb, and Dy were pursued.

Toward this goal, the purple trimetallic MoS_4^{2-}-bridged complexes (C_5Me_5)$_2$Ln(μ-S)$_2$Mo(μ-S)$_2$Ln(C_5Me_5)$_2$ (Ln = Y, Gd, Tb, Dy) were synthesized according to the first step of Scheme 4.1. Crystallographic characterization (Table S4.1) revealed two Ln^{III} centers capped by two pentamethylcyclopentadienyl ligands each and bridged by a MoS_4^{2-} ion with a pseudo-tetrahedral, diamagnetic Mo^{VI} center. One-electron reduction of these compounds using decamethylcobaltocene (Co(C_5Me_5)$_2$, −1.94 V vs. Fc$^{0/1+}$)[19] resulted in a red powder that could be isolated directly from the THF reaction mixture after removing the solvent under reduced pressure. Cooling a concentrated THF solution of this solid to −35 °C overnight afforded X-ray quality crystals and enabled structural characterization of **1-Ln**.

In the structure of the gadolinium congener (Figure 4.1, right), the two Gd^{III} centers are not equivalent by symmetry, and two different Gd···Mo distances of 3.4378(3) and 3.4419(3) Å are observed (Table 4.1). The Mo–S bond lengths support the occurrence of a Mo-centered reduction, with the average Gd–S bond lengthening from 2.1906(12) Å in $(C_5Me_5)_2Gd(\mu\text{-}S)_2Mo(\mu\text{-}S)_2Gd(C_5Me_5)_2$ to 2.2278(10) Å in **1-Gd**. The tetrahedral MoS_4 unit is compressed along the Gd···Gd axis, resulting in S–Mo–S angles of 110.96(4)°, 110.72(4)°, 106.49(4)°, and 106.65(4)°.The axis and degree of distortion of the MoS_4 tetrahedron is consistent across the **1-Ln** series.

Comparing the structure of **1-Gd** with that of **1-Y** (Figure 4.1), some intriguing differences arise. While the Mo–S bond lengths in **1-Gd** are all relatively similar, those of **1-Y** exhibit a distinct asymmetry. On one side of the molecule, long Mo–S bonds are observed, with an average bond length of 2.2391(13) Å, in addition to short Ln–S bond lengths, averaged to 2.7408(12) Å. On the opposite side, short Mo–S bonds, averaging to 2.2325(13) Å, and long Ln–S bonds, averaging to 2.7557(13) Å, are observed. This asymmetry suggests a localization of the unpaired Mo^V electron on one side of the molecule. Since the Mo^V unpaired electron populates a Mo–S antibonding orbital, Mo–S bond lengths should increase on the side of the charge localization, while Ln–S bonds on the same side may be expected to decrease due to an Ln–MoS_4 bonding-type interaction. The structures of **1-Tb** and **1-Dy** are isostructural with that of **1-Y** and show a similar asymmetry of the Mo–S and Ln–S bond lengths, again suggesting some degree of charge localization.

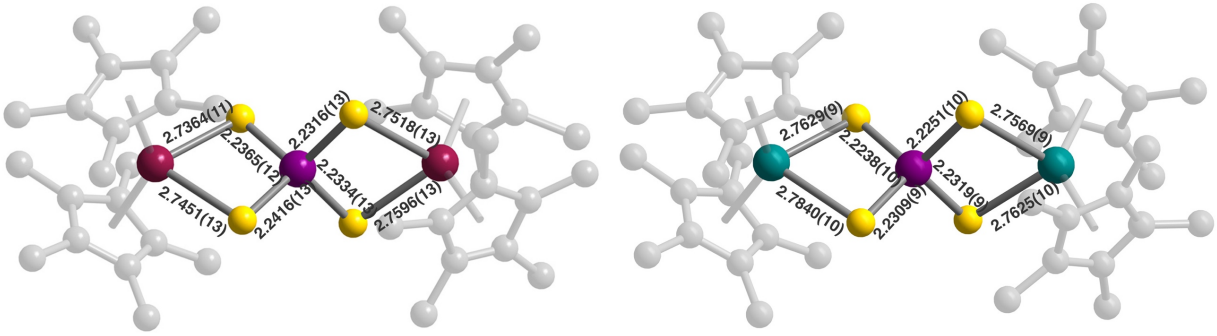

Figure 4.1. Left: Structure of the MoS_4^{3-}-bridged diyttrium complex anion in **1-Y**. Right: Structure of the MoS_4^{3-}-bridged digadolinium complex anion in **1-Gd**. Relevant bond lengths in units of Å are overlaid. Maroon, cyan, purple, yellow, and grey ellipsoids represent Y, Gd, Mo, S, and C atoms, respectively. Hydrogen atoms, a $[Co(C_5Me_5)_2]^+$ countercation, and cocrystallized solvent molecules are omitted for clarity.

The EPR spectrum of **1-Y** collected at 77 K in frozen THF (Figure 4.2) shows a primary signal consistent with an $S = {}^1/_2$ molybdenum center (^{95}Mo, $I = 0$, 75% abundance; ^{97}Mo, $I = {}^5/_2$, 25% abundance). Interestingly, the spectrum can only be reasonably fit[20] when including hyperfine coupling to a single ^{89}Y center ($I = {}^1/_2$, 100% abundance), rather than coupling to both ^{89}Y centers. Three g values of $g_x = 1.972$, $g_y = 1.980$, and $g_z = 1.988$ were included in the fit, along with three ^{95}Mo coupling constants, both sets of which are consistent with reported Mo^V EPR spectra.[19,20] In contrast, the ^{89}Y hyperfine coupling constants of $A_\perp = 23$ MHz, and $A_\parallel = 26$ MHz are substantially larger than previously observed yttrium-transition metal hyperfine couplings,[21,22] suggesting a non-negligible electron delocalization from the MoS_4^{3-} unit onto one of the Y centers. Indeed, the

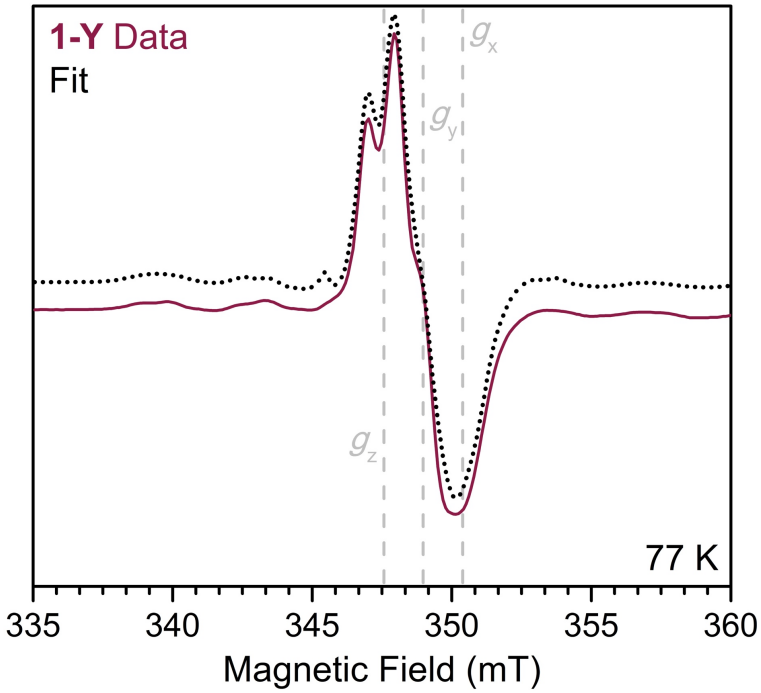

Figure 4.2. X-band EPR spectrum of **1-Y** collected at 77 K. The dotted black line represents a fit to the data, shown by a maroon line, as described in the text and Supporting Information. Fitting parameters are shown in Table S4.3. The fitting parameters g_x, g_y, and g_z, obtained as described in the Supporting Information, are shown as dashed grey lines.

divalent yttrium complex [K(2.2.2-cryptand)][$(C_5H_4SiMe_3)_3Y$], with a single electron localized in a $5d_z^2$ orbital, exhibits an only four-fold higher hyperfine coupling of A_{iso} = 102.6 MHz.[23] Charge transfer involving only a single yttrium center is further supported by the single-crystal X-ray diffraction structure of **1-Y**, which exhibits asymmetry of Mo–S and Y–S bond distances as described above, leading to two distinct Mo···Y separations of 3.4320(5) Å and 3.4263(6) Å. The shorter Mo···Y distance corresponds to longer Mo–S and shorter Y–S average distances, potentially demarcating this side of the molecule as the charge transfer pathway (Table 4.1).

Considering the character of the filled Mo^V orbital, and thereby the mechanism of Mo–Ln charge transfer, the observation from the EPR spectrum that $g_z > g_x, g_y$ suggests that the d_z^2 orbital is populated.[24] The crystallographic parameters of the MoS_4^{3-} unit may in theory be assessed to determine the nature and orientation of the d orbital; if the d_z^2 orbital is populated, the MoS_4^{3-} unit should be elongated along the z axis due to a Jahn-Teller distortion away from T_d symmetry.[25] Across the **1-Ln** series, the MoS_4^{3-} tetrahedron is elongated perpendicular to the Ln···Ln axis. However, the MoS_4^{2-} tetrahedra in $(C_5Me_5)_2Ln(\mu\text{-}S)_2Mo(\mu\text{-}S)_2Ln(C_5Me_5)_2$ are distorted to a similar degree along the same axis, suggesting that any MoS_4^{3-} distortion away from tetrahedral symmetry is a consequence of the coordination of two $LnCp^*_2$ units, rather than a Jahn-Teller perturbation. The Mo^V unpaired electron is then assigned to a d_z^2 orbital with the z axis lying parallel to the Ln···Mo···Ln axis, in agreement with preliminary DFT calculations and molecular orbital analysis of a known trinuclear MoS_4^{n-}-bridged complex.[16b] Given the large ^{89}Y hyperfine coupling, which suggests substantial Mo–Y charge transfer, one can envision a coupling mechanism that engages an empty yttrium 4d orbital. In a bent metallocene, the d_z^2 orbital is lowest in energy, and the z axis is perpendicular to the plane defined by the C_5Me_5 ring centroids and the molecular C_2-axis.[26] The

proposed orbital picture (Figure 4.3) allows for charge transfer to both lanthanide centers. Thus, the origin of the asymmetric crystal structures of **1-Y**, **1-Tb**, and **1-Dy**, as well as the unidirectional charge transfer implied by Y–Mo hyperfine coupling incorporating only a single Y^{III} center, is still under investigation. Notably, the countercation $[CoCp^*_2]^+$ is located on the same side as that of the proposed charge localization in the crystal structures of **1-Y**, **1-Tb**, and **1-Dy**, and as such may play a role in enforcing asymmetric charge transfer. However, such an argument would not explain the solution EPR spectrum of **1-Y**, in which crystal packing effects should not be possible.

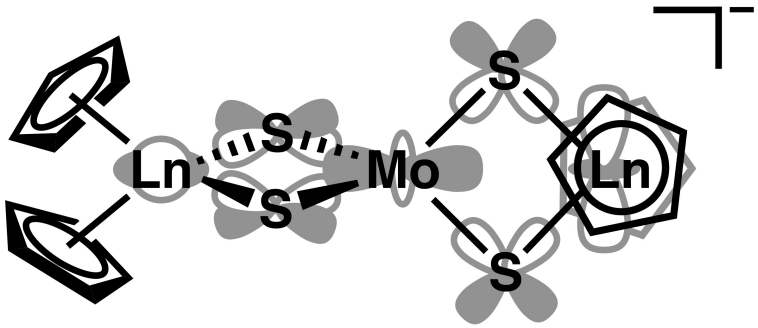

Figure 4.3. Proposed participant orbitals and magnetic coupling pathway in **1-Ln.**

Table 4.1. Comparison of Ln···Mo distances for 1-Ln.

Parameter Complex	Ln1-Mo (Å)	Ln2-Mo (Å)	Δ (Å)
1-Y	3.4263(6)	3.4320(5)	0.0057(6)
1-Gd	3.4378(3)	3.4419(3)	0.0041(3)
1-Tb	3.4389(6)	3.4454(5)	0.0065(6)
1-Dy	3.4285(4)	3.4328(4)	0.0043(4)

UV-Vis-NIR diffuse reflectance measurements of **1-Ln** (Figure 4.4) exhibit a number of features consistent with a $(MoS_4)^{3-}$ unit.[21c] As an example, **1-Gd** exhibits transitions at 33675 cm^{-1} and 21789 cm^{-1}, assigned to LMCT (S→Mo) t2→e and t1→e transitions, respectively, 18486 cm^{-1}, tentatively assigned to a triplet charge transfer transition,[27] and 11977 cm^{-1} and 10895 cm^{-1}, assigned to (Mo) ligand field e→t2 transitions, approximating the symmetry of the MoS_4^{3-} tetrahedron as T_d. In addition, an intense near-IR feature is observed at 5397 cm^{-1}, which is assigned to a metal-to-metal charge transfer transition (MMCT; Mo→Ln). The MMCT transition increases slightly in energy to 5444 cm^{-1} and 5559 cm^{-1} for **1-Tb** and **1-Dy**, respectively, and diminishes substantially in intensity from **1-Gd** to **1-Tb** to **1-Dy**, trending with the decreasing size of the 4f and 5d orbitals. Metal-to-metal charge transfer involving a lanthanide ion is exceedingly rare, with other reported examples occurring at much higher energies with much lower intensity.[28] The low energy of the MMCT transition can be ascribed to the highly reducing nature of the Mo^V ion, which should have a decent energy match with the Ln^{III}/Ln^{II} reduction potential. Further, strong-field cyclopentadienyl ligands have been shown to preferentially stabilize the lanthanide $5d_{z^2}$ orbital,[23] and as such the $5d_{z^2}$ orbital in these organometallic complexes should be more accessible compared to complexes with Ln^{III} ions in weaker ligand fields. The low-energy MMCT

indicates that **1-Ln** may have accessible Ln^{III}/Ln^{II} reduction potentials that permit isolation of derivatives with Ln^{II} centers; this avenue will be explored in future work.

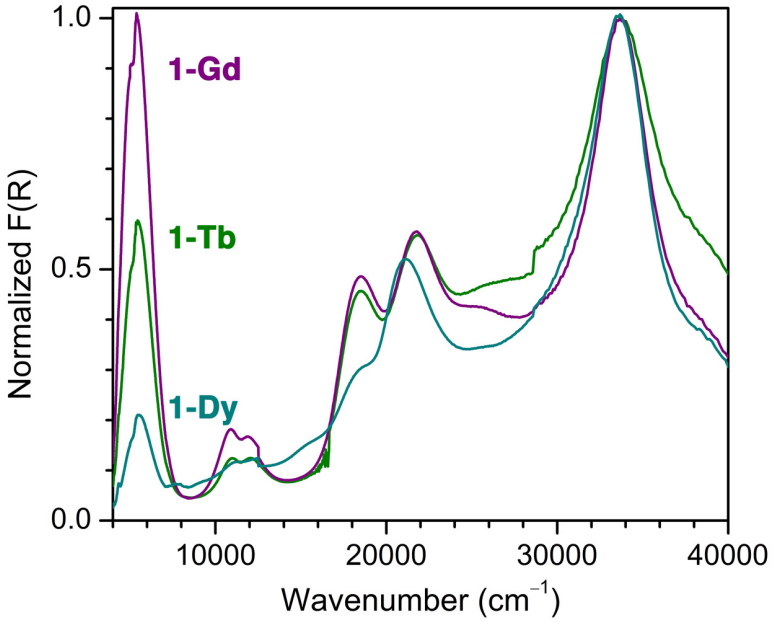

Figure 4.4. Normalized diffuse reflectance UV-vis-NIR spectra of **1-Gd**, **1-Tb**, and **1-Dy** shown in purple, green, and blue, respectively. F(R) is a Kubelka-Munk conversion of the raw diffuse reflectance spectrum. Spectra are normalized with the strongest absorbance set to F(R) = 1.

Variable-temperature dc magnetic susceptibility measurements were performed from 2–300 K in order to investigate the nature of any magnetic communication between the lanthanide centers and Mo^{V} in **1-Gd**, **1-Tb**, and **1-Dy**. For **1-Gd**, the product of magnetic susceptibility times temperature, $\chi_M T$, at room temperature was found to be 19.1 emu K/mol under an applied field of 0.1 T. This is higher than the expected magnitude of 16.135 emu K/mol for two magnetically isolated $S = {}^{7}/_{2}$ Gd^{III} centers and an $S = {}^{1}/_{2}$ Mo^{V} center (Figure 4.5), suggesting the presence of significant ferromagnetic Gd–Mo exchange. Indeed, the $\chi_M T$ product for **1-Gd** rises steadily with decreasing temperature until reaching a maximum value of 31.6 emu K/mol at 6 K, in good agreement with the expected value of 31.875 emu K/mol for an $S = {}^{15}/_{2}$ ground state. The small downturn in the $\chi_M T$ product below 6 K can be ascribed to Zeeman splitting of this large spin ground state. The nature and strength of the Gd–Mo magnetic coupling were evaluated by fitting the $\chi_M T$ data[29] using the following Hamiltonian:

$$\hat{H} = -2(J_{\mathrm{Gd-Mo}})(\hat{S}_{\mathrm{Mo}} \cdot (\hat{S}_{\mathrm{Gd(1)}} + \hat{S}_{\mathrm{Gd(2)}})) + \sum_{i=\mathrm{Gd,Mo}} \mu_B \hat{S}_i g_i H \qquad (4.1)$$

where $J_{\mathrm{Gd-Mo}}$ is the Gd–Mo magnetic coupling constant. Good agreement between data and fit was obtained using a $J_{\mathrm{Gd-Mo}}$ value of +16.1(2) cm^{-1}, along with a χ_{TIP} contribution of 0.0053(2) emu/mol. The $J_{\mathrm{Gd-Mo}}$ value represents one of the largest magnetic coupling constants observed to date between Gd^{III} and another spin center. The record value of $J_{\mathrm{Gd-e^-}} = +175$ cm^{-1} was recently determined for coupling between Gd^{III} and a radical "trapped" in a metal-metal bonding-type orbital in $Gd_2@C_{79}N$,[30] and is followed in magnitude by coupling constants of $J = -27$ cm^{-1} [2a,31] and -20 cm^{-1} [3] determined for the interaction between Gd^{III} and an N_2^{3-} radical bridge. Notably,

the extracted Gd–Mo coupling is the strongest yet observed between gadolinium and a transition metal center, superseding the previous record of +10.1 cm^{-1} for a Gd–Cu complex.[32] As expected for a strongly exchange-coupled complex, low-temperature magnetization versus applied magnetic field curves collected from 2–10 K agree well with simulated Brillouin curves for a $S = {}^{15}/_{2}$ ground state with $g = 2.05$ (Figure S4.2).

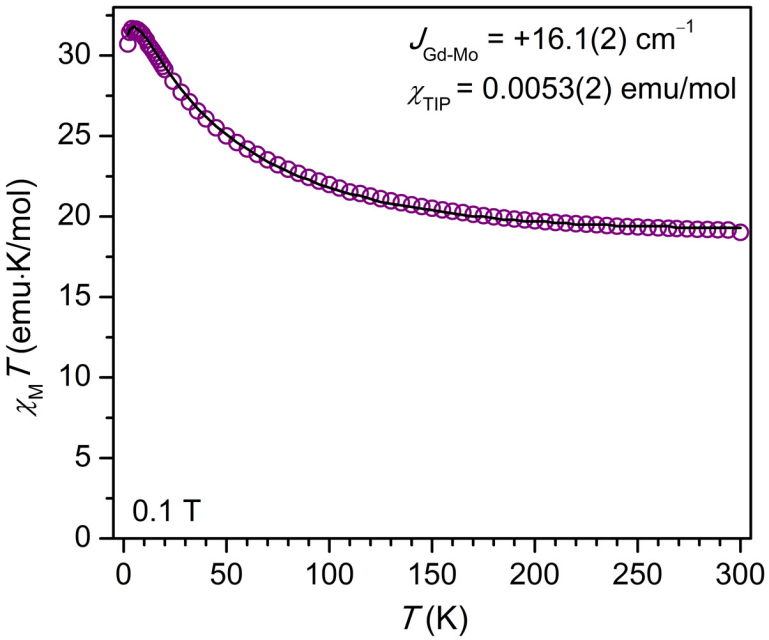

Figure 4.5. Plot of the magnetic susceptibility times temperature product ($\chi_M T$) versus temperature for **1-Gd**. Purple circles represent data collected under an applied magnetic field of 0.1 T. The black line represents a fit to the data using the Hamiltonian in Equation 4.1.

The strong Gd–Mo charge-transfer exchange interaction can be attributed to a number of factors. First and most simply, the more diffuse character of the 4d orbitals relative to those of the 3d transition metal series should promote enhanced orbital interactions with the empty 5d orbitals of the lanthanides, while the higher energy of the 4d orbitals should enable better energy matching with the lanthanide 4f orbitals. However, given the small Ln–Mo couplings observed for cyanide-bridged complexes, the nature of the bridging thiometallate in **1-Gd** must also be considered essential to achieving strong coupling. The close Gd···Mo distance of ~3.44 Å facilitated by the single-atom sulfide bridges is likely the primary aid in enhancing magnetic interactions. Indeed, Gd^{III}–Mo^{V} interactions across larger distances have been shown to be quite weak, for instance $J_{Gd-Mo} = -0.68$ cm^{-1} for an $[Mo^{V}(CN)_8]^{3-}$-Gd^{III} chain compound with a Gd···Mo separation of 5.7 Å.[8d] The diffuse and polarizable nature of the S^{2-} bridges should additionally enable enhanced spin polarization compared to cyanide ligands; the sulfide ligands of thiometallate units have been previously shown to support substantial charge and spin delocalization.[33] Finally, despite the relatively short Gd···Mo distance in **1-Gd**, the overlap integral between the Mo^{V} 4d and Ln^{III} 5d orbitals is still likely to be quite small, leading to an ideal scenario for charge-transfer-driven ferromagnetic coupling—i.e., charge transfer from a SOMO of MoS_4^{3-} to an empty Gd^{III} 5d orbital, with minimal to no SOMO/SOMO overlap.[34]

Interestingly, the dc magnetic susceptibility data for **1-Tb** and **1-Dy** do not show the same signatures of strong ferromagnetic coupling incorporating both lanthanide centers; instead, $\chi_M T$

versus T data for each compound exhibit much weaker temperature dependences (Figure 4.6). At room temperature and under an applied field of 0.1 T, the $\chi_M T$ product for **1-Tb** is 25.35 emu K/mol, slightly higher than the expected value of 24.015 emu K/mol for two magnetically isolated Tb^{III} centers and an $S = {}^1/_2$ Mo^V center. This $\chi_M T$ value, in conjunction with the steady rise in $\chi_M T$ with decreasing temperature and corresponding absence of a local minimum, supports the presence of ferromagnetic interactions between spins, analogous to **1-Gd**. However, $\chi_M T$ increases only slightly to a maximum of 26.59 emu K/mol at 85 K, indicating that either the Ln–Mo coupling is weak relative to that present in **1-Gd**, or possibly that the Mo^V center couples to only a single Tb^{III} center. The latter explanation is better supported by the EPR observation of Y–Mo hyperfine coupling with only a single yttrium center in **1-Y**, as well as a disparity in Tb···Mo distances, as was observed in **1-Y** (see Table 4.1). In this scenario, the $\chi_M T$ data should simply reflect the sum of $\chi_M T$ for a coupled Tb^{III}–Mo^V pair with that of a magnetically-isolated Tb^{III} center, and as such will show reduced temperature dependence because of the absence of a fully coupled ground state involving both Tb^{III} ions.

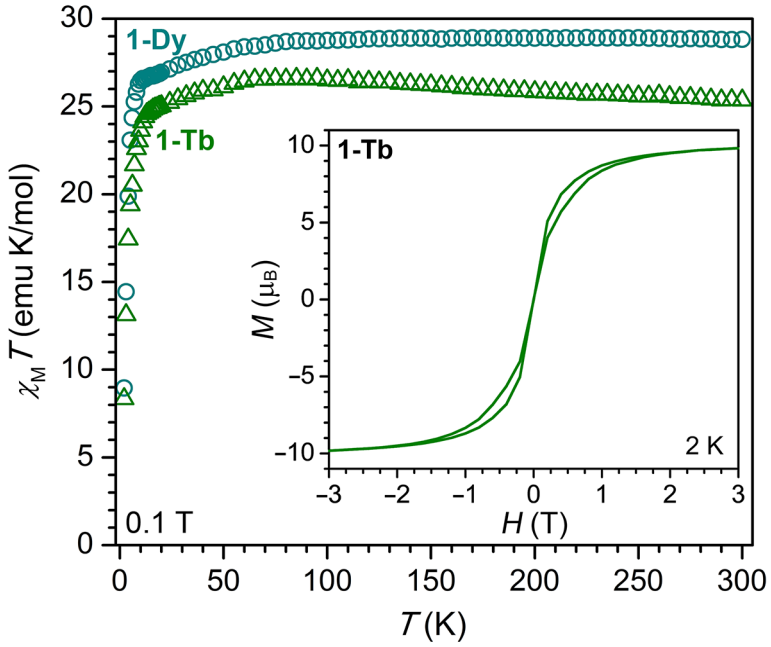

Figure 4.6. Magnetic susceptibility times temperature products ($\chi_M T$) versus temperature of **1-Tb** and **1-Dy**, represented by green triangles and cyan circles, respectively, collected under an applied magnetic field of 0.1 T. Inset: Magnetization versus applied magnetic field curve for **2-Tb** collected at 2 K with a field sweep rate of 0.4 mT s^{-1}.

The room temperature $\chi_M T$ product for **1-Dy** is 28.82 emu K/mol under an applied field of 0.1 T, also close to the expected value of 28.615 emu K/mol for two magnetically isolated Dy^{III} centers and an $S = {}^1/_2$ Mo^V center. The slightly higher than expected $\chi_M T$ value again supports the presence of ferromagnetic interactions, while two distinct Dy···Mo separations (Table 4.1) and a weak increase in $\chi_M T$ with decreasing temperature support magnetic coupling of the Mo^V to only a single Dy^{III} center. The decrease in $\chi_M T$ observed for both **1-Tb** and **1-Dy** at low temperatures is attributed to thermal depopulation of exchange-coupled and crystal-field-split states. The nature of the seemingly unilateral Ln–Mo magnetic exchange in **1-Tb** and **1-Dy** remains under investigation,

while the participation of both Gd^{III} centers in coupling to the Mo^{V} spin in **1-Gd**—in contrast to the Y^{III}, Tb^{III}, and Dy^{III} congeners— is consistent with the proposed orbital picture (Figure 4.3).

Finally, **1-Tb** and **1-Dy** were investigated using ac magnetic susceptibility measurements to elucidate any features of slow magnetic relaxation. We note that while magnetic coupling of metal centers can in principle generate a well-isolated, large-spin ground state conducive to slow magnetic relaxation under zero applied magnetic field, only a few 4f-*n*d (n = 4, 5) molecular complexes have actually been found to exhibit slow magnetic relaxation.[9a,9c,9d] Variable-temperature ac magnetic susceptibility data were collected for **1-Tb** and **1-Dy** under zero dc field using a 4-Oe field oscillating at frequencies ranging from 1 to 1500 Hz. Between 2 and 13 K, both **1-Tb** (Figure S4.3) and **1-Dy** (Figure 4.7, top) exhibit asymmetric peaks in the out-of-phase susceptibility, χ'', indicative of slow magnetic relaxation. Plots of the in-phase susceptibility, χ', versus the out-of-phase susceptibility, χ'', (Cole-Cole plots) appear as broad and asymmetric semicircles, suggesting the overlap of more than one time regime for the magnetization relaxation and hence more than one relaxation process. The severity of this overlap precluded extraction of precise relaxation time data for distinct processes (Figure S4.4), and instead the Cole-Cole plot data for both compounds were approximately fit using a single modified Debye model,[1a] yielding values for the relaxation time, τ, at each temperature. Among the resulting fitted parameters is the α value, which provides a measure of the uniformity of relaxation and ranges from 0 to 1, with smaller values corresponding to relaxation dominated by a single process. Values of α as high as 0.4-0.5 at the lowest temperatures for both **1-Tb** and **1-Dy** confirm the presence of multiple processes.

To gain some insight into the nature of the slow magnetic relaxation exhibited by **1-Tb**, we examined the temperature dependence of the natural log of the relaxation times (Figure S4.5) and found pronounced curvature instead of the Arrhenius behavior of a thermally-activated over-barrier relaxation process. The temperature dependence of τ was best fit using the expression $\tau^{-1} = CT^n$, with $C = 12.3\ s^{-1}\ K^{-n}$ and $n = 2.5$ (Figure S4.5), indicating that at least one Raman relaxation mechanism, a spin–lattice relaxation process that occurs through virtual magnetic excited states, likely dominates in the examined temperature and frequency range. Under an applied field between 2 and 5 K, the relaxation time of **1-Tb** is also sufficiently long to observe waist-restricted magnetic hysteresis (Figure 4.6, inset, and Figure S4.6).

In contrast, no magnetic hysteresis was observed for **1-Dy** using the same field sweep rate and for temperatures as low as 2 K (Figure S4.9), although this compound exhibits ac peaks over a similar temperature and frequency range as **1-Tb** (Figures 4.7, S4.7, and S4.8). Relaxation times extracted from ac magnetic susceptibility data suggest that slow magnetic relaxation for **1-Dy** arises due to both Raman relaxation and thermally-activated Orbach relaxation. Accordingly, an Arrhenius plot of the relaxation times could be fit to the equation:

$$\tau^{-1} = CT^n + \tau_0^{-1} \exp\left(-\frac{U_{\text{eff}}}{k_B T}\right) \qquad (4.2)$$

with $C = 10.2\ s^{-1}\ K^{-n}$, $n = 2.2$, $\tau_0 = 5.7 \times 10^{-9}$ s, and $U_{\text{eff}} = 68\ cm^{-1}$ (Figure 4.6, bottom). It is possible that the barrier to magnetization reversal exhibited by **1-Dy** derives from Dy^{III} single-ion anisotropy, as opposed to the energy landscape of the total coupled system, although with the present data it is not possible to make a definitive determination. Nevertheless, the 68 cm^{-1} barrier is the highest yet observed for any complex containing a lanthanide ion and a 4d metal center, nearly double the prior record of 30 cm^{-1} for a Dy^{III} ion coordinated to a ruthenium acetylide

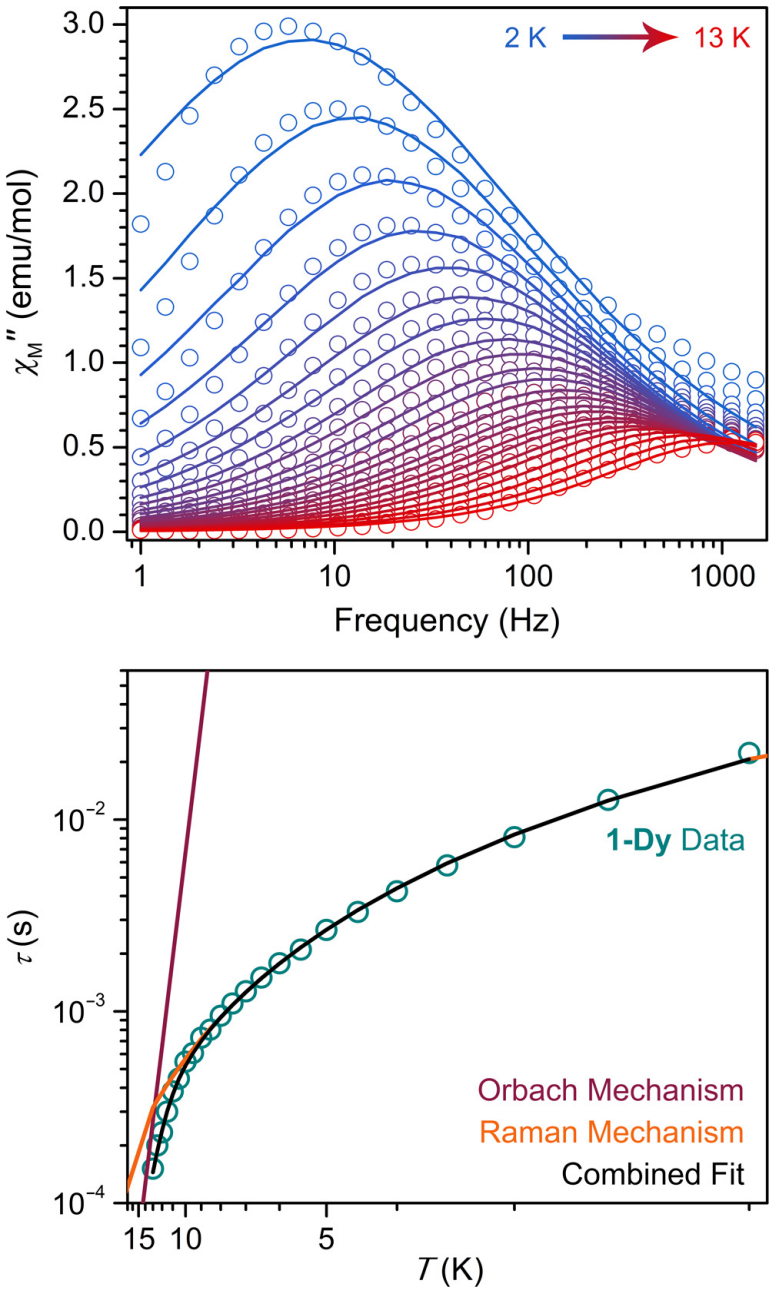

Figure 4.7. Top: Variable-temperature out-of-phase magnetic susceptibility versus frequency data for **1-Dy**, collected at temperatures ranging from 2 to 13 K under zero applied magnetic field. Colored symbols represent data points and lines represent fits of the data to a generalized Debye model. Bottom: Arrhenius plot of magnetic relaxation times, τ (log scale) versus temperature (inverse scale) for **1-Dy**. Data are represented by cyan circles. Orange and maroon lines represent the Raman and Orbach components, respectively, of the fit to the data, while the black line represents the total fit to Equation 4.2, as described in the text, with values of $C = 10.2\ s^{-1}\ K^{-n}$, $n = 2.2$, $\tau_0 = 5.7 \times 10^{-9}$ s, and $U_{eff} = 68\ cm^{-1}$.

moiety.[9b] Moreover, the barrier for **1-Dy** is the highest for any complex simply containing a 4d metal center.[7b] Although it is not possible to distinguish whether one or both Ln^{III} centers (one of

which is coupled to the Mo^{V} spin) contribute to slow magnetic relaxation, we note that a temperature-independent regime is not observed in the Arrhenius plot for either **1-Tb** or **1-Dy**, indicating the absence of zero-field tunneling behavior, possibly inhibited by Ln^{III}–Mo^{V} exchange.[4a,35]

The absence of large barriers to magnetic relaxation in both **1-Tb** and **1-Dy** likely arises due to two main factors. First, in both complexes the Mo^{V} spin is proposed to be coupled only to a single lanthanide center, preventing formation of a fully-coupled, large-spin ground state. Second, since the strongly donating $(C_5Me_5)^{1-}$ ligands should define the magnetic axis of each lanthanide (assuming an oblate electronic state)[36,37] and the $(C_5Me_5)^{1-}$ ligands on each lanthanide in **1-Tb** and **1-Dy** are in planes roughly perpendicular to one another, the anisotropy axes of the lanthanide centers are likely close to perpendicular. Systems containing magnetic ions with non-collinear magnetic axes typically exhibit mixed axiality ground states, which enable quantum tunneling of magnetization as well as low-lying excited states.[38] Improved single-molecule magnet behavior could be achieved via rational synthesis of a molecule with collinear lanthanide anisotropy axes, in which both lanthanides can strongly engage in 4f/5d-*n*d interactions. With this in mind, we are now pursuing dilanthanide molecules incorporating octahedral or square planar 4d or 5d complexes with the single-atom bridging ligands that should enable strong magnetic exchange.

4.4 Conclusions and Outlook

Mechanisms of *n*d-4f magnetic exchange have long captivated the molecular magnetism community.[39] The foregoing results demonstrate for the first time that 4d, and likely 5d, metal centers can achieve strong magnetic interactions with lanthanide ions in molecular complexes. Polarizable bridging ligands that facilitate charge and spin transfer and sufficiently short lanthanide-transition metal distances likely play crucial roles in the strength of magnetic exchange. While strong ferromagnetic coupling is observed between both Gd^{III} centers and Mo^{V} in **1-Gd**, unilateral coupling seems to occur in **1-Tb** and **1-Dy**, and the origins of this distinct behavior remain under investigation. Compounds **1-Tb** and **1-Dy** also exhibit slow magnetic relaxation, with the latter compound displaying the largest value of U_{eff} yet observed for both a 4f-4d complex and any 4d-metal-containing complex. Altogether, these results highlight new strategies with which to achieve strong magnetic exchange with the trivalent lanthanide ions and suggest the possibility of accessing larger barrier *n*d-4f single-molecule magnets via enhanced *n*d-4f magnetic exchange.

4.5 Acknowledgements

This work was performed in collaboration with Monica D. Boshart. We thank the U. S. National Science Foundation for support of this research through grants CHE-1565776 (William J. Evans) and CHE-1800252 (Jeffrey R. Long). Analysis of the EPR spectrum (Wayne Lukens) was supported by the U.S. Department of Energy, Office of Science, Basic Energy Sciences, Chemical Sciences, Biosciences, and Geosciences Division, Heavy Element Chemistry Program and was performed at Lawrence Berkeley National Laboratory under contract No. DE-AC02-05CH11231. Single-crystal X-ray diffraction data for **1-Gd** were collected on Beamline 12.2.1 at the Advanced Light Source, which is supported by the Director, Office of Science, Office of Basic Energy Sciences, of the U.S. Department of Energy under Contract no. DE-AC-02-05CH11231. The NSF Graduate Research Fellowship Program is thanked for support of L.E.D. Dr. Joseph Ziller, Dr. Jason R. Jones, Michael K. Wojnar, and Ari Turkiewicz are thanked for assistance with X-ray

crystallography. Professor Alan F. Heyduk is thanked for helpful discussions, and Dr. Katie Meihaus is thanked for editorial assistance.

4.6 References

(1) (a) Gatteschi, D., Sessoli, R., Villain, J. *Molecular Nanomagnets*, Oxford University Press, Oxford, 2006. (b) Woodruff, D. N.; Winpenny, R. E. P.; Layfield, R. A. *Chem. Rev.* **2013**, *113*, 5110–5148.
(2) (a) Rinehart, J. D.; Fang, M.; Evans, W. J.; Long, J. R. *Nat. Chem.* **2011**, *3*, 538–542. (b) Rinehart, J. D.; Fang, M.; Evans, W. J.; Long, J. R. *J. Am. Chem. Soc.* **2011**, *133*, 14236–14239.
(3) Demir, S.; Gonzalez, M. I.; Darago, L. E.; Evans, W. J.; Long, J. R. *Nat. Commun.* **2017**, *8*, 2144.
(4) (a) Langley, S. K.; Wielechowski, D. P.; Vieru, V.; Chilton, N. F.; Moubaraki, B.; Abrahams, B. F.; Chibotaru, L. F.; Murray, K. S. *Angew. Chem. Int. Ed.* **2013**, *52*, 12014–12019. (b) Ungur, L.; Thewissen, M.; Costes, J.-P.; Wernsdorfer, W.; Chibotaru, L. F. *Inorg. Chem.* **2013**, *52*, 6328–6337.
(5) (a) Guo, F.-S.; Day, B. M.; Chen, Y.-C.; Tong, M.-L.; Mansikkamäki, A.; Layfield, R. A. *Angew. Chem. Int. Ed.* **2017**, *56*, 11445–11449. (b) Goodwin, C. A. P.; Ortu, F.; Reta, D.; Chilton, N. F.; Mills, D. P. *Nature* **2017**, *548*, 439–442.
(6) Rosado Piquer, L.; Sañudo, E. C. *Dalton Trans.* **2015**, *44*, 8771–8780.
(7) (a) Visinescu, D.; Desplanches, C. D.; Imaz, I.; Bahers, V.; Pradhan, R.; Villamena, F. A.; Guionneau, P.; Sutter, J.-P. *J. Am. Chem. Soc.* **2006**, *128*, 10202–10212. (b) Wang, X.-Y.; Avendano, C.; Dunbar, K. R. *Chem. Soc. Rev.* **2011**, *40*, 3213–3238 and references therein.
(8) Cyanide Ln-TM bridges: (a) Hozumi, T.; Ohkoshi, S.-I.; Arimoto, Y.; Seino, H.; Mizobe, Y.; Hashimoto, K. *J. Phys. Chem. B* **2003**, *107*, 11571–11574. (b) Ikeda, S.; Hozumi, T.; Hashimoto, K.; Ohkoshi, S.-I. *Dalton Trans.* **2005**, *378*, 2120–2123. (c) Przychodzeń, P.; Lewiński, K.; Pełka, R.; Bałanda, M.; Tomala, K.; Sieklucka, B. *Dalton Trans.* **2006**, 625–628. (d) Tanase, S.; de Jongh, L. J.; Prins, F.; Evangelisti, M. *ChemPhysChem* **2008**, *9*, 1975–1978. (e) Prins, F.; Pasca, E.; de Jongh, L. J.; Kooijman, H.; Spek, A. L.; Tanase, S. *Angew. Chem. Int. Ed.* **2007**, *46*, 6081–6084. (f) Przychodzeń, P.; Pełka, R.; Lewiński, K.; Supel, J.; Rams, M.; Tomala, K.; Sieklucka, B. *Inorg. Chem.* **2007**, *46*, 8924–8938. (g) Chelebaeva, E.; Larionova, J.; Guari, Y.; Sá Ferreira, R. A.; Carlos, L. D.; Almeida Paz, F. A.; Trifonov, A.; Guérin, C. A. *Inorg. Chem.* **2008**, *47*, 775–777. (h) Chelebaeva, E.; Larionova, J.; Guari, Y.; Ferreira, R. A. S.; Carlos, L. D.; Paz, F. A. A.; Trifonov, A.; Guérin, C. *Inorg. Chem.* **2009**, *48*, 5983–5995. (i) Dhers, S.; Sahoo, S.; Costes, J.-P.; Duhayon, C.; Ramasesha, S.; Sutter, J.-P. *CrystEngComm* **2009**, *11*, 2078–2083. (j) Visinescu, D.; Madalan, A. M.; Andruh, M.; Duhayon, C.; Sutter, J.-P.; Ungur, L.; Van den Heuvel, W.; Chibotaru, L. F. *Chem. Eur. J.* **2009**, *15*, 11808–11814. (k) Zhou, H.; Chen, Q.; Zhou, H.-B.; Yang, X.-Z.; Song, Y.; Yuan, A.-H. (l) Alexandru, M.-G.; Visinescu, D.; Shova, S.; Lloret, F.; Julve, M. *Inorg. Chem.* **2017**, *56*, 12594–12605. (m) Note: Trimetallic complexes in which a 3d transition metal ion is between the 4d/5d and 4f centers are not included here, since in these complexes there is typically no reasonable 4d/5d-4f magnetic coupling pathway.
(9) Non-cyanide Ln-TM bridges: (a) Pointillart, F.; Bernot, K.; Sessoli, R.; Gatteschi, D. *Inorg. Chem.* **2010**, *49*, 4355–4361. (b) Martínez-Lillo, J.; Cañadillas-Delgado, L.; Cano, J.; Lloret, F.; Julve, M.; Faus, J. A. *Chem. Commun.* **2012**, *48*, 9242–9244. (c) Norel, L.; Feng, M.; Bernot, K.; Roisnel, T.; Guizouarn, T.; Costuas, K.; Rigaut, S. *Inorg. Chem.* **2014**, *53*, 2361–2363. (d) Langley, S. K.; Wielechowski, D. P.; Vieru, V.; Chilton, N. F.; Moubaraki, B.; Chibotaru, L. F.; Murray, K.

S. *Chem. Commun.* **2015**, *51*, 2044–2047. (e) Marinescu, G.; Maxim, C.; Clérac, R.; Andruh, M. *Inorg. Chem.* **2015**, *54*, 5621–5623. (f) Pejo, C.; Guedes, G. P.; Novak, M. A.; Speziali, N. L.; Chiozzone, R.; Julve, M.; Lloret, F.; Vaz, M. G. F.; González, R. *Chem. Eur. J.* **2015**, *21*, 8696–8700.
(10)(a) Herrmann, W. A. *Synthetic Methods of Organometallic and Inorganic Chemistry*, Thieme: Stuttgart, 1997, Vol. 8. (b) Meyer, G.; Ax, P. *Mat. Res. Bull.* **1982**, 17, 1447–1455.
(11) Evans, W. J.; Kozimor, S. A.; Ziller, J. W.; Kaltsoyannis, N. *J. Am. Chem. Soc.* **2004**, *126*, 14533–14547.
(12) Evans, W. J.; Kozimor, S. A.; Brady, J. C.; Davis, B. L.; Nyce, G. W.; Seibel, C. A.; Ziller, J. W.; Doedens, R. J. *Organometallics* **2005**, *24*, 2269–2278.
(13) (a) Izod, K.; Liddle, S. T.; Clegg, W. *Inorg. Chem.* **2004**, *43*, 214–218. (b) Evans, W. J.; Davis, B. L.; Champagne, T. M.; Ziller, J. W. *Proc. Natl. Acad. Sci. U. S. A.* **2006**, *103*, 12678–12683.
(14) Lang, J.-P.; Kawaguchi, H.; Tatsumi, K. *J. Chem. Soc. Dalt. Trans.* **2002**, 2573–2580.
(15) (a) Müller, A.; Dartmaan, M.; Römer, C.; Clegg, W.; Sheldrick, G. M. *Angew. Chem. Int. Ed.* **1981**, *20*, 1060–1061. (b) Gheller, S. F.; Hambley, T. W.; Rodgers, J. R.; Brownlee, R. T. C.; O'Connor, M. J.; Snow, M. R.; Wedd, A. G. *Inorg. Chem.* **1984**, *23*, 2519–2528. (c) Beheshti, A.; Clegg, W.; Sadr, M. H. *Inor. Chim. Acta* **2002**, *335*, 21–26. (d) Niu, Y.-Y.; Chen, T.-N.; Liu, S.-X.; Song, Y.-L.; Wang, Y.-X.; Xue, Z.-L.; Xin, X.-Q. *J. Chem. Soc. Dalt. Trans.* **2002**, 1980–1984. (e) Zheng, H.-G.; Zhou, H.-L.; Tan, W.-L.; Niu, Y.-Y.; Ji, W.; Xin, X.-Q. *Inorg. Chim. Acta* **2002**, *340*, 29–34.
(16) (a) Coucouvanis, D.; Baenziger, N. C.; Simhon, E. D.; Stremple, P.; Swensen, D.; Simopoulos, A.; Kostikas, A.; Petrouleas, V.; Papaefthymiou, V. *J. Am. Chem. Soc.* **1980**, *102*, 1732–1734.
(b) Müller, A.; Jostes, R.; Schmitz, K.; Krickemeyer, E.; Bögge, H.; Bill, E.; Trautwein, A. *Inorg. Chim. Acta* **1988**, *149*, 9–12. (c) Müller, A.; Krickemeyer, E.; Bögge, H. *Z. Anorg. Allg. Chem.* **1987**, *554*, 61.
(17) Blacque, O.; Brunner, H.; Kubicki, M. M.; Lucas, D.; Meier, W.; Mugnier, Y.; Nuber, B.; Stubenhofer, B.; Wachter, J. *J. Organomet. Chem.* **1998**, *564*, 71–79.
(18) Evans, W. J.; Ansari, M. A.; Ziller, J. W.; Khan, S. I. *Organometallics* **1995**, *14*, 3–4.
(19) Connelly, N. G.; Geiger, W. E. *Chem. Rev.* **1996**, *96*, 877–910.
(20) Stoll, S.; Schweiger, A. *J. Magn. Reson.* **2006**, *178*, 42–55.
(21) (a) Greenblatt, M.; Strobel, P.; Pifer, J. H. *J. Chem. Phys.* **1981**, *74*, 6580–6583. (b) Pifer, J. H.; Ziemski, S.; Greenblatt, M.; Wanklyn, B. M. *J. Solid State Chem.* **1982**, *45*, 93–98. (c) Schäfer, R.; Fiedler, J.; Moscherosch, M.; Kaim, W. *J. Chem. Soc. Chem. Commun.* **1993**, *114*, 896–897. (d) Ecclestone, T.; Laurie, S. H.; Symons, M. C. R.; Taiwo, F. A. *Polyhedron* **1998**, *17*, 1435–1438.
(22) Greenblatt, M.; Pifer, J. H.; McGarvey, B. R.; Wanklyn, B. M. *Chem. Phys.* **1981**, *74*, 6014–6017.
(23) MacDonald, M. R.; Bates, J. E.; Ziller, J. W.; Furche, F.; Evans, W. J. *J. Am. Chem. Soc.* **2013**, *135*, 9857–9868.
(24) (a) Abragam, A.; Bleaney, B. *Electron Paramagnetic Resonace of Transtion Ions*, Clarendon Press: Oxford, 1970. (b) McGarvey, B. R. In *Transition Metal Chemistry, a Series of Advances*; Carlin, R. L., Ed.; Marcel Dekker: New York, 1966.
(25) Záliš, S.; Stoll, H.; Baerends, E. J.; Kaim, W. *Inorg. Chem.* **1999**, *38*, 6101–6105.
(26) (a) Petersen, J. L.; Lichtenberger, D. L., Fenske, R .F.; Dahl, L. F. *J. Am. Chem. Soc.* **1975**, *97*, 6433-6441. (b) Albright, T. A.; Burdett, J. K.; Whangbo, M.–H. *Orbital Interactions in Chemistry*, Wiley-Interscience: New York, 1985.

(27) (a) Kober, E. M.; Meyer, T. J. *Inorg. Chem.* **1982**, *21*, 3967–3977. (b) Schäfer, R.; Kaim, W.; Moscherosch, M.; Krejčik, M. *J. Chem. Soc., Chem. Commun.* **1992**, *93*, 834–835.
(28) (a) Sabbatini, N.; Bonazzi, A.; Ciano, M.; Balzani, V. *J. Am. Chem. Soc.* **1984**, *106*, 4055–4056. (b) Chorazy, S.; Arczynski, M.; Nakabayashi, K.; Sieklucka, B.; Ohkoshi, S.-I. *Inorg. Chem.* **2015**, *54*, 4724–4736. (c) Yoshida, T.; Cosquer, G.; Izuogu, D. C.; Ohtsu, H.; Kawano, M.; Lan, Y.; Wernsdorfer, W.; Nojiri, H.; Breedlove, B. K.; Yamashita, M. *Chem. Eur. J.* **2017**, *125*, 3576–3577. (d) Yoshida, T.; Izougu, D. C.; Iwasawa, D.; Ogata, S.; Hasegawa, M.; Breedlove, B. K.; Cosquer, G.; Wernsdorfer, W.; Yamashita, M. *Chem. Eur. J.* **2017**, *23*, 10527–10531.
(29) Chilton, N. F.; Anderson, R. P.; Turner, L. D.; Soncini, A.; Murray, K. S. *J. Comput. Chem.* **2013**, *34*, 1164–1175.
(30) (a) Liu, F.; Krylov, D. S.; Spree, L.; Avdoshenko, S. M.; Samoylova, N. A.; Rosenkranz, M.; Kostanyan, A.; Greber, T.; Wolter, A. U. B.; Büchner, B.; Popv, A. A. *Nat. Commun.* **2017**, *8*, 16098. (b) Hu, Z.; Dong, B.-W.; Liu, Z.; Liu, J.-J.; Su, J.; Yu, C.; Xiong, J.; Shi, D.-E.; Wang, Y.; Wang, B.-W.; Ardavan, A.; Shi, Z.; Jiang, S.–D.; Gao, S. *J. Am. Chem. Soc.* **2018**, *140*, 1123–1130.
(31) Meihaus, K. R.; Corbey, J. F.; Fang, M.; Ziller, J. W.; Long, J. R.; Evans, W. J. *Inorg. Chem.* **2014**, *53*, 3099−3107.
(32) Costes, J.-P.; Dahan, F. O.; Dupuis, A. *Inorg. Chem.* **2000**, *39*, 165−168.
(33) Müller, A.; Diemann, E.; Jostes, R.; Bögge, H. *Angew. Chem. Int. Ed.* **1981**, *20*, 934–955.
(34) Kollmar, C.; Kahn, O. *Acc. Chem. Res.* **1993**, *26*, 259–265.
(35) Guo, Y.-N.; Xu, G.-F.; Wernsdorfer, W.; Ungur, L.; Guo, Y.; Tang, J.; Zhang, H.-J.; Chibotaru, L. F.; Powell, A. K. *J. Am. Chem. Soc.* **2011**, *133*, 11948–11951.
(36) Tuna, F.; Smith, C. A.; Bodensteiner, M.; Ungur, L.; Chibotaru, L. F.; McInnes, E. J. L.; Winpenny, R. E. P.; Collison, D.; Layfield, R. A. *Angew. Chem. Int. Ed.* **2012**, *51*, 6976–6980.
(37) Demir, S.; Zadrozny, J. M.; Long, J. R. *Chem. Eur. J.* **2014**, *20*, 9524–9529.
(38) Barra, A. L.; Caneschi, A.; Cornia, A.; Gatteschi, D.; Gorini, L.; Heiniger, L.-P.; Sessoli, R.; Sorace, L. *J. Am. Chem. Soc.* **2007**, *129*, 10754–10762.
(39) Benelli, C.; Gatteschi, D. *Chem. Rev.* **2002**, *102*, 2369–2388.

Chapter 4 Supporting Information

S4.1 Experimental Details

X-ray Data Collection, Structure Solution and Refinement

For $(C_5Me_5)_2Y(\mu\text{-}S)_2Mo(\mu\text{-}S)_2Y(C_5Me_5)_2$, 1-Y: A purple crystal of approximate dimensions 0.088 × 0.163 × 0.264 mm was mounted on a glass fiber and transferred to a Bruker SMART APEX II diffractometer. The APEX2[1] program package was used to determine the unit-cell parameters and for data collection (35 sec/frame scan time for a sphere of diffraction data). The raw frame data was processed using SAINT[2] and SADABS[3] to yield the reflection data file. Subsequent calculations were carried out using the SHELXTL[4] program. There were no systematic absences nor any diffraction symmetry other than the Friedel condition. The centrosymmetric triclinic space group $P\bar{1}$ was assigned and later determined to be correct. The structure was solved by direct methods and refined on F^2 by full-matrix least-squares techniques. The analytical scattering factors[5] for neutral atoms were used throughout the analysis. Hydrogen atoms were included using a riding model. Carbon atoms C(31)-C(40) were disordered and included using multiple components with partial site-occupancy-factors. There was one-half molecule of toluene solvent present. The solvent was located about an inversion center and was disordered. Hydrogen atoms associated with the solvent were not included in the refinement. At convergence, wR2 = 0.0929 and Goof = 1.023 for 584 variables refined against 9829 data (0.78 Å), R1 = 0.0373 for those 8373 data with $I > 2.0\sigma(I)$.

For $(C_5Me_5)_2Gd(\mu\text{-}S)_2Mo(\mu\text{-}S)_2Gd(C_5Me_5)_2$, Gd: A purple crystal of approximate dimensions 0.095 × 0.144 × 0.200 mm was mounted on a glass fiber and transferred to a Bruker SMART APEX II diffractometer. The APEX2[1] program package was used to determine the unit-cell parameters and for data collection (10 sec/frame scan time for a sphere of diffraction data). The raw frame data was processed using SAINT[2] and SADABS[3] to yield the reflection data file. Subsequent calculations were carried out using the SHELXTL[4] program. There were no systematic absences nor any diffraction symmetry other than the Friedel condition. The centrosymmetric triclinic space group $P\bar{1}$ was assigned and later determined to be correct.

The structure was solved by dual space methods and refined on F^2 by full-matrix least-squares techniques. The analytical scattering factors[5] for neutral atoms were used throughout the analysis. There were two molecules of the formula-unit present (Z = 4). Hydrogen atoms were included using a riding model. There was one-half molecule of toluene solvent present per formula-unit. The solvents were located about inversion centers and were disordered. Hydrogen atoms associated with the solvents were not included in the refinement. Least-squares analysis yielded wR2 = 0.0791 and Goof = 1.045 for 929 variables refined against 21640 data (0.75Å), R1 = 0.0314 for those 17706 data with $I > 2.0\sigma(I)$.

For $(C_5Me_5)_2Tb(\mu\text{-}S)_2Mo(\mu\text{-}S)_2Tb(C_5Me_5)_2$, Tb: A purple crystal of approximate dimensions 0.095 × 0.144 × 0.200 mm was mounted in a cryoloop and transferred to a Bruker SMART APEX II diffractometer. The APEX2[1] program package was used to determine the unit-cell parameters and for data collection (60 sec/frame scan time for a sphere of diffraction data). The raw frame data was processed using SAINT[2] and SADABS[3] to yield the reflection data file. Subsequent calculations were carried out using the SHELXTL[4] program. There were no systematic absences nor any diffraction symmetry other than the Friedel condition. The centrosymmetric triclinic space group $P\bar{1}$ was assigned and later determined to be correct.

The structure was solved by dual space methods and refined on F^2 by full-matrix least-squares techniques. The analytical scattering factors[5] for neutral atoms were used throughout the analysis. There were two molecules of the formula-unit present (Z = 4). Hydrogen atoms were included using a riding model. There was one-half molecule of toluene solvent present per formula-unit. The solvents were located about inversion centers and were disordered. Hydrogen atoms associated with the solvents were not included in the refinement. Least-squares analysis yielded wR2 = 0.0812 and Goof = 1.010 for 929 variables refined against 19675 data (0.78Å), R1 = 0.0329 for those 15075 data with I > 2.0σ(I).

$(C_5Me_5)_2Dy(\mu\text{-}S)_2Mo(\mu\text{-}S)_2Dy(C_5Me_5)_2$, Dy: A brown crystal of approximate dimensions 0.063 × 0.083 × 0.316 mm was mounted in a cryoloop and transferred to a Bruker SMART APEX II diffractometer. The APEX2[1] program package was used to determine the unit-cell parameters and for data collection (60 sec/frame scan time for a sphere of diffraction data). The raw frame data was processed using SAINT[2] and SADABS[3] to yield the reflection data file. Subsequent calculations were carried out using the SHELXTL[4] program. There were no systematic absences nor any diffraction symmetry other than the Friedel condition. The centrosymmetric triclinic space group $P\bar{1}$ was assigned and later determined to be correct. The structure was solved by direct methods and refined on F^2 by full-matrix least-squares techniques. The analytical scattering factors[5] for neutral atoms were used throughout the analysis. Hydrogen atoms were included using a riding model. Carbon atoms C(31)-C(40) were disordered and included using multiple components with partial site-occupancy-factors. There was one-half molecule of toluene solvent present. The solvent was located about an inversion center and was disordered. Hydrogen atoms associated with the solvent were not included in the refinement. At convergence, wR2 = 0.0625 and Goof = 1.021 for 534 variables refined against 9845 data (0.78 Å), R1 = 0.0274 for those 8254 data with I > 2.0σ(I).

$[(C_5Me_5)_2Y(\mu\text{-}S)_2Mo(\mu\text{-}S)_2Y(C_5Me_5)_2][Co(C_5Me_5)_2]$, Y: A red crystal of approximate dimensions 0.203 × 0.235 × 0.491 mm was mounted on a glass fiber and transferred to a Bruker SMART APEX II diffractometer. The APEX2[1] program package was used to determine the unit-cell parameters. Data was collected using a 25 sec/frame scan time for a sphere of diffraction data. The raw frame data was processed using SAINT[2] and SADABS[3] to yield the reflection data file. Subsequent calculations were carried out using the SHELXTL[4] program. There were no systematic absences nor any diffraction symmetry other than the Friedel condition. The centrosymmetric triclinic space group $P\bar{1}$ was assigned and later determined to be correct. The structure was solved by direct methods and refined on F^2 by full-matrix least-squares techniques. The analytical scattering factors[5] for neutral atoms were used throughout the analysis. Hydrogen atoms were included using a riding model. There were three molecules of tetrahydrofuran solvent present. Several atoms were disordered and included using multiple components with partial site-occupancy-factors. Least-squares analysis yielded wR2 = 0.1975 and Goof = 1.035for 658 variables refined against 18095 data (0.73 Å), R1 = 0.0623 for those 14603 with I > 2.0σ(I).

$[(C_5Me_5)_2Gd(\mu\text{-}S)_2Mo(\mu\text{-}S)_2Gd(C_5Me_5)_2][Co(C_5Me_5)_2]$, 1-Gd: A red crystal of approximate dimensions 0.028 × 0.021 × 0.014 mm was coated in Paratone-N oil and mounted on a MiTeGen loop. The crystal was frozen at 100 K by an Oxford Cryosystems Cryostream 700 Plus. Data were collected at Beamline 12.2.1 at the Advanced Light Source at Lawrence Berkeley National Laboratory using synchrotron radiation (λ = 0.7288 Å) on a Bruker D8 diffractometer equipped with a Bruker PHOTON II CPAD detector. Raw data were integrated and corrected for Lorentz and polarization effects using Bruker AXS SAINT software.[2] Absorption corrections were applied using SADABS.[3] Subsequent calculations were carried out using the SHELXTL[4] program

operated in the OLEX2[6] interface. No significant crystal decay was observed during data collection. Thermal parameters were refined anisotropically for all non-hydrogen atoms. Hydrogen atoms were placed in ideal positions and refined using a riding model for all structures. Least-squares analysis yielded wR2 = 0.0648, R1 = 0.0294, and Goof = 1.042.

[$(C_5Me_5)_2Tb(\mu\text{-}S)_2Mo(\mu\text{-}S)_2Tb(C_5Me_5)_2$][$Co(C_5Me_5)_2$], 1-Tb: A red crystal of approximate dimensions 0.160 × 0.294 × 0.392 mm was mounted on a glass fiber and transferred to a Bruker SMART APEX II diffractometer. The APEX2[1] program package was used to determine the unit-cell parameters. Data was collected using a 20 sec/frame scan time for a sphere of diffraction data. The raw frame data was processed using SAINT[2] and SADABS[3] to yield the reflection data file. Subsequent calculations were carried out using the SHELXTL[4] program. There were no systematic absences nor any diffraction symmetry other than the Friedel condition. The centrosymmetric triclinic space group $P\bar{1}$ was assigned and later determined to be correct. The structure was solved by dual space methods and refined on F^2 by full-matrix least-squares techniques. The analytical scattering factors[5] for neutral atoms were used throughout the analysis. Hydrogen atoms were included using a riding model. There were three molecules of tetrahydrofuran solvent present. Several atoms were disordered and included using multiple components with partial site-occupancy-factors. Least-squares analysis yielded wR2 = 0.1233 and Goof = 1.029 for 690 variables refined against 17277 data (0.76 Å), R1 = 0.0442 for those 14006 with I > 2.0σ(I).

[$(C_5Me_5)_2Dy(\mu\text{-}S)_2Mo(\mu\text{-}S)_2Dy(C_5Me_5)_2$][$Co(C_5Me_5)_2$], **1-Dy**: A red crystal of approximate dimensions 0.309 × 0.316 × 0.392 mm was mounted on a glass fiber and transferred to a Bruker SMART APEX II diffractometer. The APEX2[1] program package was used to determine the unit-cell parameters. Data was collected using a 15 sec/frame scan time for a sphere of diffraction data. The raw frame data was processed using SAINT[2] and SADABS[3] to yield the reflection data file. Subsequent calculations were carried out using the SHELXTL[4] program. There were no systematic absences nor any diffraction symmetry other than the Friedel condition The centrosymmetric triclinic space group $P\bar{1}$ was assigned and later determined to be correct. The structure was solved by dual space methods and refined on F^2 by full-matrix least-squares techniques. The analytical scattering factors[5] for neutral atoms were used throughout the analysis. Hydrogen atoms were included using a riding model. There were three molecules of tetrahydrofuran solvent present. Several atoms were disordered and included using multiple components with partial site-occupancy-factors. Least-squares analysis yielded wR2 = 0.0884 and Goof = 1.064 for 690 variables refined against 17208 data (0.76 Å), R1 = 0.0336 for those 15764 with I > 2.0σ(I).

Definitions:

$wR2 = [\Sigma[w(F_o^2-F_c^2)^2] / \Sigma[w(F_o^2)^2]\ ]^{1/2}$

$R1 = \Sigma||F_o|-|F_c|| / \Sigma|F_o|$

$Goof = S = [\Sigma[w(F_o^2-F_c^2)^2] / (n-p)]^{1/2}$ where n is the number of reflections and p is the total number of parameters refined.

Fitting Details for EPR Spectrum of 1-Y

The spectrum was clipped to remove data above and below the actual signal; the final spectral range as 335 mT to 363 mT. In addition, every other point was removed to reduce the number of data points and hasten fitting the spectrum.

The spectrum was fit using EasySpin[7] using second-order perturbation theory. Three g values and three ^{95}Mo hyperfine coupling constants, A(^{95}Mo), were used in the fit, but the other parameters were fit as though the spectrum were axial (two principal components for A(^{89}Y) and g-strain). The spectrum was fit using two sets of hyperfine coupling constants. The strong central signal is due to Mo isotopes with even atomic mass numbers; it displays coupling to a single atom with I = 1/2, presumably ^{89}Y. The spectrum cannot be fit as well if two I = 1/2 isotopes are included. The spectrum was fit allowing either the g-strain or hyperfine coupling constants of the central peak to vary but not both at the same time. Since the hyperfine coupling is not resolved for the high field peaks, g-strain has a similar effect on the simulated spectrum as does $A_{\perp}$(^{89}Y) resulting in strong correlation between these parameters. The smaller features in the spectrum are due to hyperfine coupling to the ^{95}Mo (16% abundance) and ^{97}Mo (9.6% abundance). Since their nuclear moments are similar, they were fit using a single species with I = 5/2.

Fitting was performed iteratively. The central feature (even mass number Mo isotopes) was fit to determine the values of g and A(^{89}Y). These values were used (and not allowed to vary) for a second species along with another A matrix for ^{95}Mo. In the second step, ^{95}Mo hyperfine coupling and g-strain of the ^{95}Mo species were fit. After the fit had converged, the central feature was fit again, and the values obtained for g and A(^{89}Y) were transferred to the ^{95}Mo species, and A(^{95}Mo), the line width and g-strain of the ^{95}Mo species were fit again. This process continued until an acceptable fit was obtained.

The agreement between the simulated and experimental spectra is good apart from the region around 346 mT where the ^{95}Mo hyperfine features parallel to the z-axis are too narrow in the simulation relative to the spectrum. Increasing the g-strain in this direction did not improve the fit. The hyperfine coupling to the I = 1/2 nucleus is only resolved along one axis (assigned to the z-axis or parallel axis). Consequently, the hyperfine coupling constant in the perpendicular direction has a large uncertainty due to strong correlation with the g-strain in this direction. The ^{95}Mo hyperfine coupling constants also have a large uncertainty due to the limited amplitude of the features and because the central portion of the spectrum is obscured by the strong signal due to the Mo isotopes with even mass numbers.

Magnetic Measurements

Samples were prepared by adding crystalline powder of **1-Gd** (13.9 mg), **1-Tb** (18.7 mg), or **1-Dy** (16.9 mg) to a 5 mm inner diameter quartz tube containing a raised quartz platform. Solid eicosane was added to cover the sample to prevent crystallite torqueing and provide good thermal contact between the sample and the cryostat. The tubes were fitted with Teflon sealable adapters, evacuated on a Schlenk line, and flame-sealed under static vacuum. Following flame sealing, the solid eicosane was melted in a water bath held at 40 °C. Magnetic susceptibility measurements were performed using a Quantum Design MPMS2 SQUID magnetometer. Dc magnetic susceptibility measurements were collected in the temperature range 2–300 K under applied magnetic fields of 0.1 T, 0.5, and 1 T. Diamagnetic corrections were applied to the data using Pascal's constants to give χ_D = –0.0008057 emu/mol (**1-Gd**) χ_D = –0.0008037 emu/mol (**1-Tb**), χ_D = –0.00104808

emu/mol (**1-Dy**), and χ_D = –0.00024306 emu/mol (eicosane).

Fitting of AC Susceptibility Data

AC susceptibility data for **1-Tb** and **1-Dy** were fit using a generalized Debye function. While data for both complexes clearly reflects more than one relaxation process, shown by additional components not accounted for by the fit on both high and low frequency ends of the data collected, the close overlap of the timescales of these relaxation processes did not allow for accurate extraction of multiple relaxation times per temperature. As such, the standard single-process Debye function was used to fit both data sets. Applied magnetic fields did decreased the magnitude of peaks in χ'' and shifted them to lower frequency, without significantly altering the peak breadth. Solvent-diluted magnetic samples were not possible due to the limited solubility of **1-Tb** and **1-Dy**.

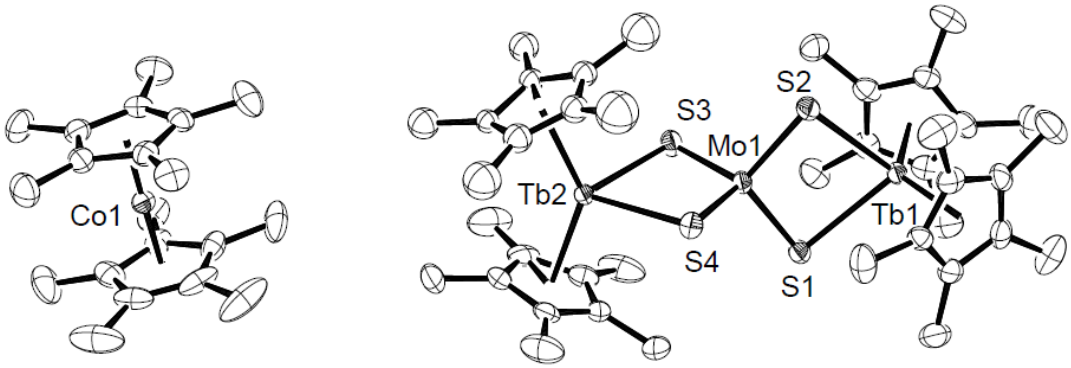

Figure S4.1. ORTEP diagram of **1-Tb** with ellipsoids shown at 50% probability. Hydrogen atoms and co-crystallized solvent molecules have been removed for clarity.

Table S4.1. Crystallographic details for $(C_5Me_5)_2Ln(\mu\text{-}S)_2Mo(\mu\text{-}S)_2Ln(C_5Me_5)_2$.

Ln	**Y**	**Gd**	**Tb**	**Dy**
Empirical formula	$C_{40}H_{60}MoS_4Y_2 \cdot ½(C_7H_8)$	$C_{40}H_{60}MoS_4Gd_2 \cdot ½(C_7H_8)$	$C_{40}H_{60}MoS_4Tb_2 \cdot ½(C_7H_8)$	$C_{40}H_{60}MoS_4Dy_2 \cdot ½(C_7H_8)$
Formula weight	988.94	1125.62	1128.96	1136.12
Temperature (K)	88(2)	88(2)	133(2)	88(2)
Space group	$P\bar{1}$	$P\bar{1}$	$P\bar{1}$	$P\bar{1}$
a (Å)	10.6530(5)	10.6470(7)	10.6478(14)	10.653(7)
b (Å)	13.7219(6)	17.2551(11)	13.7560(18)	13.779(9)
c (Å)	17.1935(8)	26.5973(16)	17.199(2)	17.175(11)
α (°)	109.1095(5)	100.9140(7)	109.0658(16)	109.161(7)
β (°)	106.3207(6)	97.6421(7)	106.5415(16)	106.358(7)
γ (°)	94.7936(6)	106.6827(7)	94.5822(16)	94.614(7)
Volume (Å^3)	2236.02(18)	4503.9(5)	2240.5(5)	2243(2)
Z	2	4	2	2
ρ_{calcd} (Mg/m^3)	1.469	1.660	1.673	1.682
μ (mm^{-1})	3.065	3.339	3.612	3.787
$R1^a$	0.0373	0.0314	0.0279	0.0274
$wR2^b$	0.0475	0.0736	0.0639	0.0583

Table S4.2. Crystallographic details for $[(C_5Me_5)_2Ln(\mu\text{-}S)_2Mo(\mu\text{-}S)_2Ln(C_5Me_5)_2][Co(C_5Me_5)_2]$, **1-Ln**.

	1-Y	**1-Gd**	**1-Tb**	**1-Dy**
Empirical formula	$C_{60}H_{90}MoS_4Y_2 \cdot 3(C_4H_8O)$	$C_{60}H_{90}MoS_4Gd_2 \cdot 2.5(C_4H_8O)$	$C_{60}H_{90}MoS_4Tb_2 \cdot 3(C_4H_8O)$	$C_{60}H_{90}MoS_4Dy_2 \cdot 3(C_4H_8O)$
Formula weight	1488.56	1589.18	1628.58	1635.74
Temperature (K)	163(2)	100(2)	173(2)	163(2)
Space group	$P\bar{1}$	$P\bar{1}$	$P\bar{1}$	$P\bar{1}$
a (Å)	13.4367(7)	13.6260(4)	13.4660(14)	13.4326(6)
b (Å)	15.5484(8)	14.9561(5)	15.5735(17)	15.5499(7)
c (Å)	17.8903(9)	17.5531(5)	17.9456(19)	17.8967(8)
α (°)	96.6278(7)	84.647(2)	96.5915(13)	96.6247(5)
β (°)	97.2769(7)	80.781(2)	97.3365(13)	97.2624(5)
γ (°)	93.2738(7)	80.980(2)	93.1581(14)	93.2596(5)
Volume (Å^3)	3673.0(3)	3478.77(19)	3698.6(7)	3673.7(3)
Z	2	2	2	2
ρ_{calcd} (Mg/m^3)	1.346	1.517	1.462	1.479
μ (mm^{-1})	2.109	6.750	2.430	2.555
$R1^a$	0.0623	0.0294	0.0442	0.0336
$wR2^b$	0.1855	0.0648	0.1134	0.0864

Table S4.3. EPR Parameters of complex **1-Y**.

g_x	1.972
g_y	1.980
g_z	1.988
$A_x(^{95}Mo)$	107.2 MHz
$A_y(^{95}Mo)$	89.3 MHz
$A_z(^{95}Mo)$	59.6 MHz
A.Rotation.z	19°
A.Rotation.y	29°
A.Rotation.z	18°
$A_\perp(^{89}Y)$	23.4
$A_\parallel(^{89}Y)$	26.2
Linewidth	0.168 mT
Perpendicular g-strain (even number Mo)	0.0081
Parallel g-strain (even number Mo)	0.0038
Perpendicular g-strain (^{95}Mo)	0.0117
Parallel g-strain (^{95}Mo)	0.0003

Table S4.4. Comparison of **1-Y** EPR parameters with relevant M^V-containing compounds. All hyperfine coupling constants *A* are reported in MHz.

Parameter	Y_2Mo	MoS_4^{3-} [8]	Mo^V in $[(NC)(OC)_3Re(MoS_4)Re(CO)_3(CN)]^{3-}$ [9]	Cr^V in YPO_4 [10]	$Ca_{1-x}Y_xMoO_4$ [11]
g_x	1.972	1.973	1.965	1.9511	1.8925
g_y	1.980	1.973	1.965	1.9511	1.8753
g_z	1.988	1.953	2.019	1.9773	1.9780
$A_x(^{95}Mo)$	107.2	140	—	—	116
$A_y(^{95}Mo)$	89.3	140	—	—	128
$A_z(^{95}Mo)$	59.6	83	—	—	67
$A_\perp(^{89}Y)$	23.4	—	—	4.2	—
$A_\parallel(^{89}Y)$	26.2	—	—	4.8	—

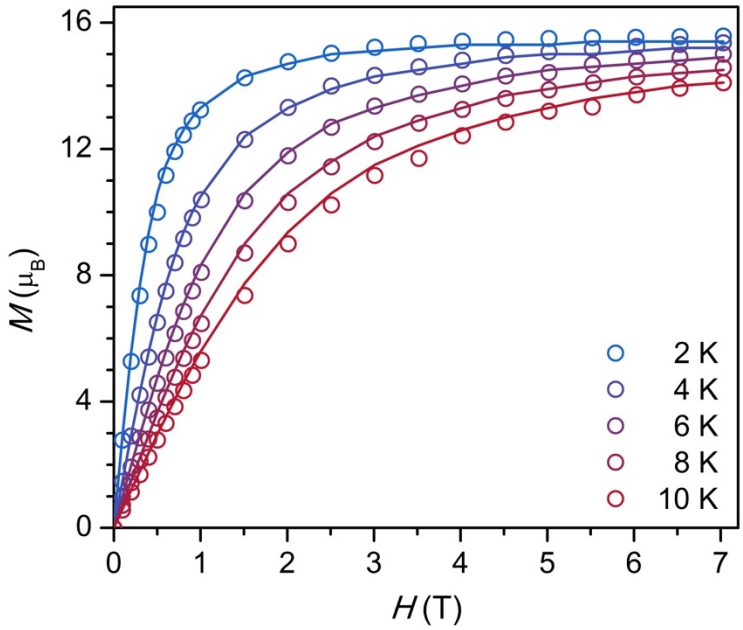

Figure S4.2. Variable-temperature *M* versus *H* curves for **1-Gd** collected from 0 to 7 T. Data points are represented by colored circles and solid lines reflect the Brillouin function for an $S = {}^{15}/_{2}$ system with $g = 2.05$. The Brillouin function was modeled using *PHI*.[12]

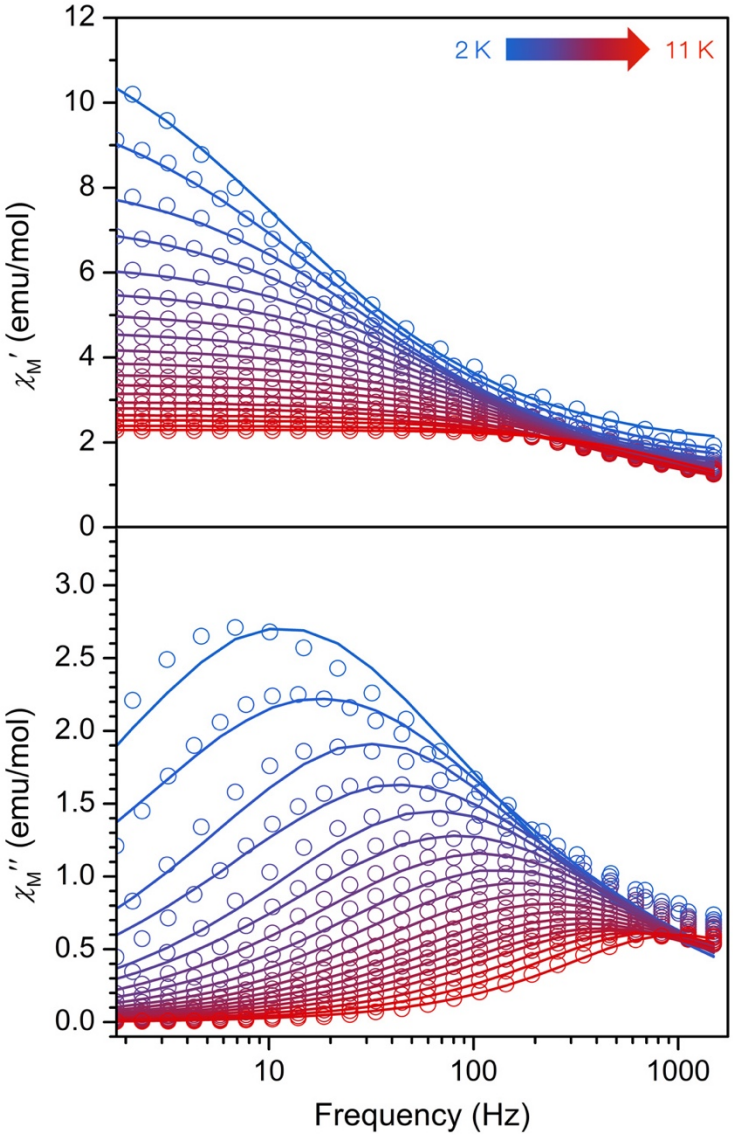

Figure S4.3. Molar in-phase (χ_M') and out-of-phase (χ_M'') magnetic susceptibility versus frequency for **1-Tb**. Colored circles represent data points and while colored lines represent fits to a generalized Debye model as referenced in the main text.

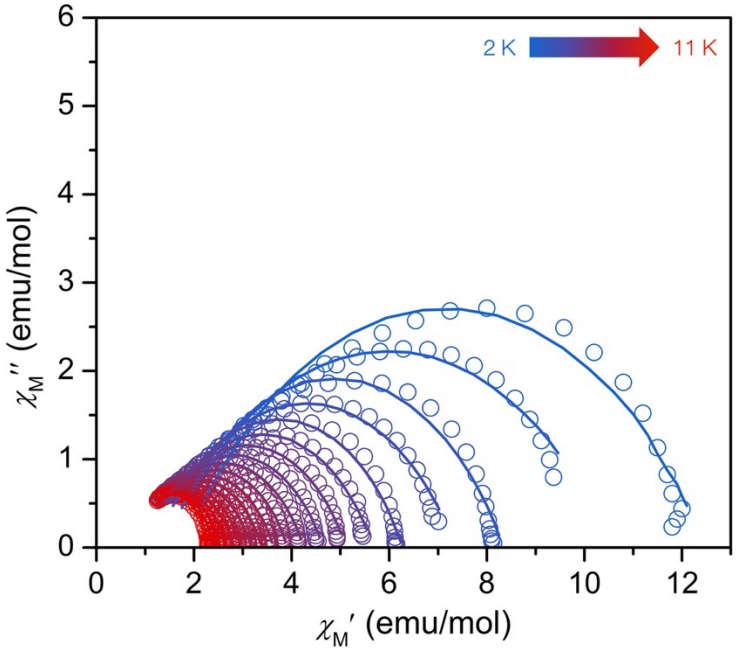

Figure S4.4. Cole-Cole plots for **1-Tb**. Colored circles represent data points and colored lines represent fits to a generalized Debye model. Data were fit with $0.14 \leq \alpha \leq 0.42$.

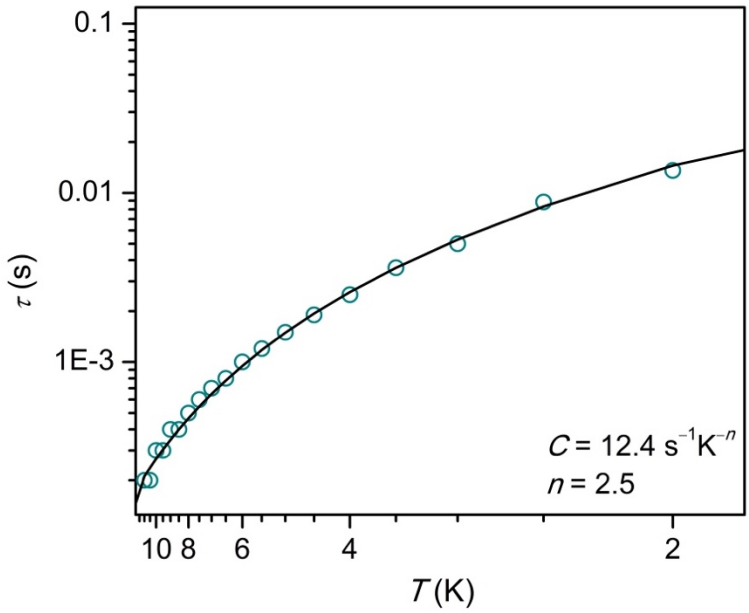

Figure S4.5. Plot of the relaxation time (log scale) versus temperature (inverse scale) for **1-Tb**. Data points are represented by cyan circles and the solid black line represents a fit of the data to the equation for a single Raman relaxation process, $\tau^{-1} = CT^n$.

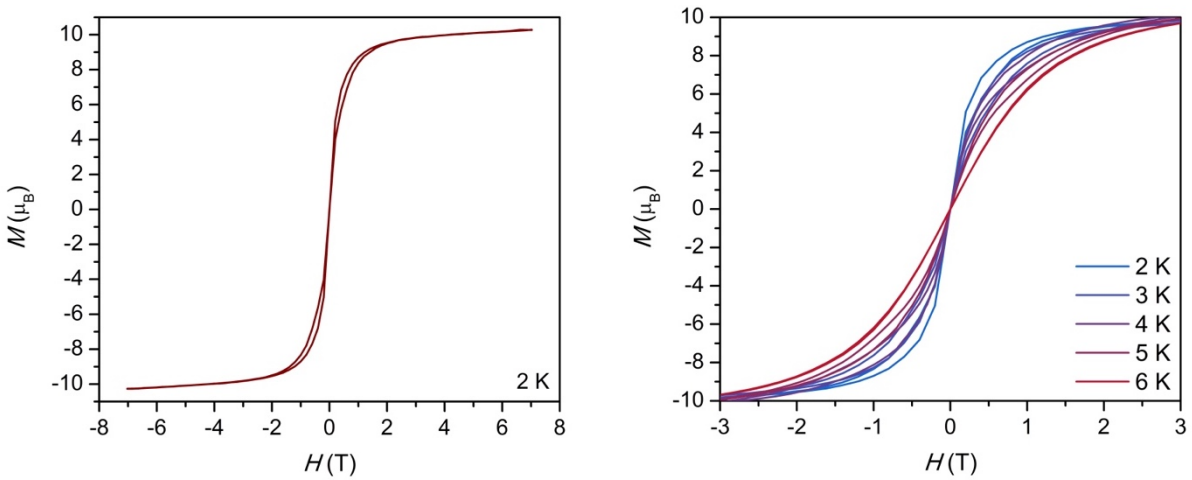

Figure S4.6. Left: Magnetization versus field data for **1-Tb** collected at 2 K using a field sweep rate of 0.4 mT s^{-1}, revealing magnetic hysteresis. Right: Magnetization versus field curves for **1-Tb** from 2 to 6 K.

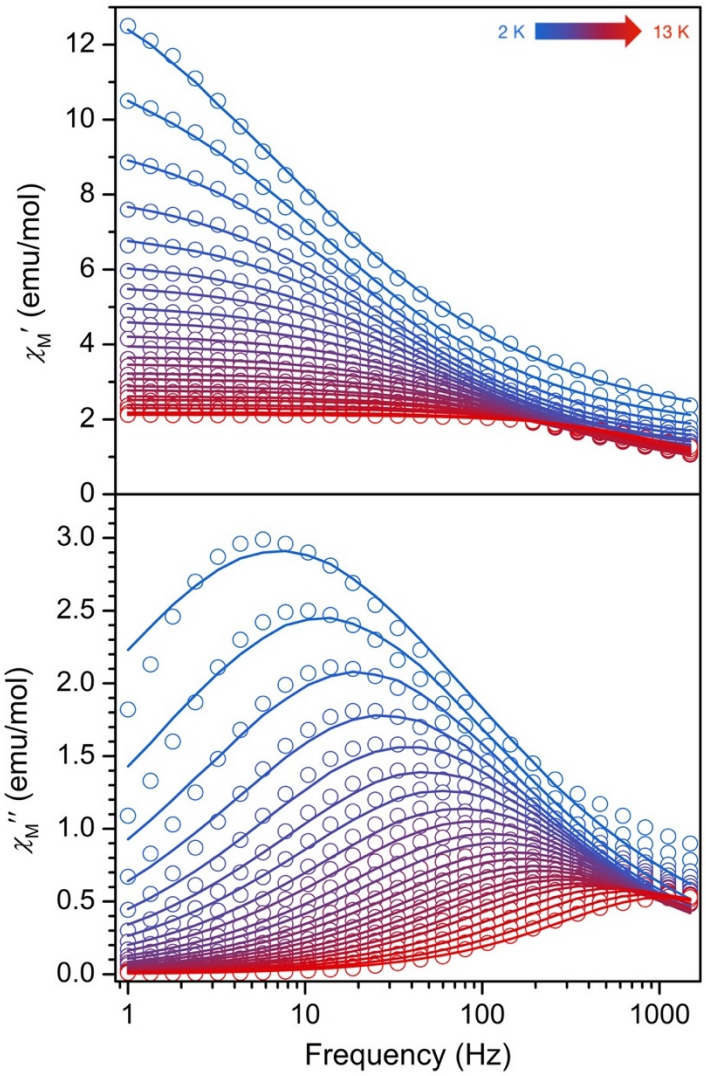

Figure S4.7. Variable-temperature in-phase (χ_M') and out-of-phase (χ_M'') magnetic susceptibility versus frequency data for **1-Dy**, collected at temperatures ranging from 2 to 13 K under zero applied magnetic field. Colored circles represent data points and colored solid lines represent fits to a generalized Debye function as referenced in the main text. All data were fit with $0.19 \leq \alpha \leq 0.50$.

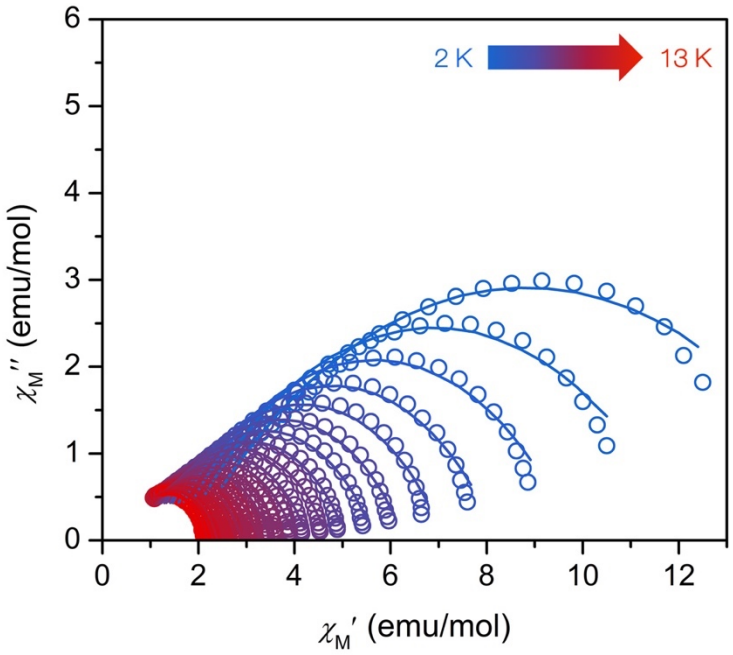

Figure S4.8. Cole-Cole plots for **1-Dy**. Colored circles represent data and colored lines represent fits to a generalized Debye model.

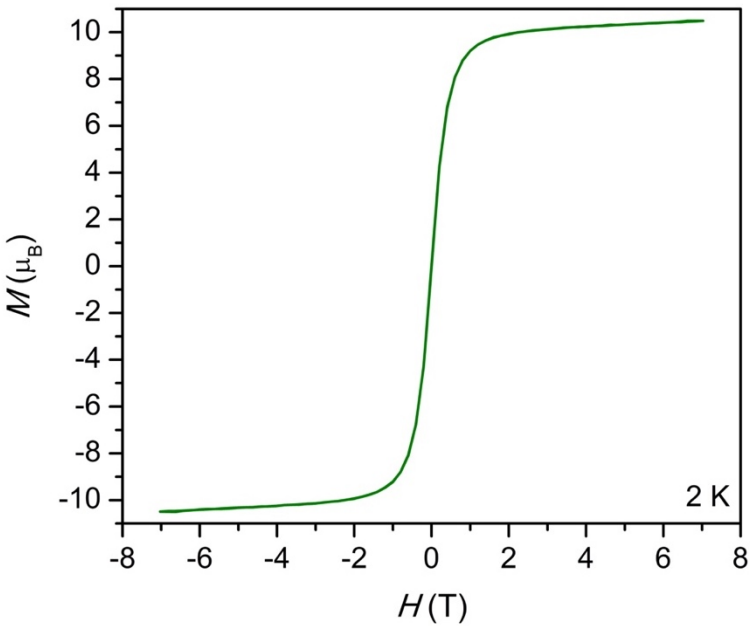

Figure S4.9. Magnetization versus field plot for **1-Dy** collected at 2 K, collected using a field sweep rate of 0.5 mT s^{-1}.

S4.2 References for Chapter 4 Supporting Information

(1) APEX2 Version 2014.11-0, Bruker AXS, Inc.; Madison, WI 2014.
(2) SAINT Version 8.34a, Bruker AXS, Inc.; Madison, WI 2013.
(3) Sheldrick, G. M. SADABS, Version 2014/5, Bruker AXS, Inc.; Madison, WI 2014.
(4) Sheldrick, G. M. SHELXTL, Version 2014/7, Bruker AXS, Inc.; Madison, WI 2014.
(5) *International Tables for Crystallography*, Vol. C.; Kluwer Academic Publishers: Dordrecht, 1992.
(6) G. Dolomanov, O. V.; Bourhis, L. J.; Gildea, R. J.; Howard, J. A. K.; Puschmann, H. *J. Appl. Crystallogr.* **2009**, *42*, 339−341.
(7) Stoll, S.; Schweiger, A. EasySpin, a comprehensive software package for spectral simulation and analysis in EPR. *J. Magn. Reson.* **2006**, *178*, 42–55.
(8) Ecclestone, T.; Laurie, S. H.; Symons, M. C. R.; Taiwo, F. A. E. EPR studies on irradiated group VI tetrachalconide ions. *Polyhedron* **1998**, *17*, 1435–1438.
(9) Schäfer, R.; Fiedler, J.; Moscherosch, M.; Kaim, W. First characterization of a tetrathiomolybdate(V) derivative by EPR, UV–VIS and IR spectroelectrochemistry. *J. Chem. Soc., Chem. Commun.* **1993**, *114*, 896–897.
(10) Greenblatt, M.; Pifer, J. H.; McGarvey, B. R.; Wanklyn, B. M. Electron spin resonance of Cr^{5+} in YPO_4 and YVO_4. *J. Chem. Phys.* **1981**, *74*, 6014–6017.
(11) Greenblatt, M.; Strobel, P.; Pifer, J. H. Magnetic resonance study of Mo^{5+} in $Ca_{1-x}Y_xMoO_4$. *J. Chem. Phys.* **1981**, *74*, 6580–6583.
12) Chilton, N. F.; Anderson, R. P.; Turner, L. D.; Soncini, A.; Murray, K. S. PHI: A powerful new program for the analysis of anisotropic monomeric and exchange-coupled polynuclear d- and f-block complexes. *J. Comput. Chem.* **2013**, *34*, 1164–1175.